Project 412

RELIABILITY ANALYSIS OF A TOP-TENSIONED TLP RISER JOINT INDUSTRY PROJECT

Final Report

Prepared for

ARCO Exploration and Production Technology
Amoco Production Company
Chevron Petroleum Technology Company
Conoco, Inc.
U.S. Minerals Management Service
Mobil Technology Company
Shell E&P Technology Company
Texaco, Inc.

by

Risk Engineering, Inc
4155 Darley Avenue, Suite A
Boulder, CO 80303 USA

July 20, 2001

PROPRIETARY

ACKNOWLEDGMENTS

This study was funded by Arco, BP-Amoco, Chevron, Conoco, MMS, Mobil, Shell, and Texaco. We wish to thank the technical representatives of these sponsors (Roy Shilling, Bernie Stahl and Hugh Banon, Chuck Petrauskas, Fikry Botros, Charles Smith and Larry Ake, Gene Berek, G.T. Ju and Denby Morrison, and Dave Wisch, respectively) for their support of this study, for their technical guidance, and for data they agreed to share with the study. In particular, we thank Bernie Stahl for his boundless support and enthusiasm.

The subcontractors and consultants for this study were Chuck Miller of Stress Engineering, C. Allin Cornell and Steve Winterstein of Stanford University, Paul Wirsching of the University of Arizona, and Kim Vandiver of MIT. We wish to thank them for their valuable contributions.

We also received inputs and comments from many other individuals, particularly Dan Beal (Arco), Mike Spillane (Atlantia), Pierre Beynet, Hin Chiu, Jeff Geyer, and Dave Driver (BP-Amoco), Don Allen (Shell), Kim Mork (DNV), Hugh Thompson, T.M. Hsu, Tim Finnigan, Irv Brooks, and Kenn Loch (Chevron), and Chang Wang (Texaco).

CONTENTS

1. Introduction

1.1 BACKGROUND

There is no well-established design practice for the extreme-load and fatigue design of risers in the U.S. A common approach consists of designing for the 100-year motion of the vessel. The forces and stresses associated with the 100-year surge are calculated using time-domain simulations, equivalent-linear models in the frequency domain, or combined approaches. The peak stresses obtained from the time-domain analyses are then multiplied by a single safety factor. The controlling ultimate limit states are tension (at the top) and bending (at the top and bottom). Other limit states of interest are fatigue and wear due to riser interference or other causes. These limit-states become more complicated, and have higher uncertainties, if less conventional riser materials are used. Fatigue life calculations are affected by vortex-induced vibration during times of high current and by wave-zone effects. The operating conditions (e.g., internal pressure, density of fluids in riser) associated with the various limit states are chosen using engineering judgment.

This approach has a number of limitations. For instance, waves may have a more important role in riser loads than in vessel motions. Also, a single safety factor is applied to the combined load effect, regardless of the uncertainties associated with the various loads. For instance, the same factor is applied to operational loads (which have low uncertainties) and to environmental loads (which have much higher uncertainties). These limitations will become more important as production moves into deeper waters and new riser materials are introduced.

The first step towards a more rational response-based design of risers is to develop response-based load- and resistance-factor design (LRFD) design criteria similar to those developed for TLPs (Banon et al., 1994). The resulting multiple load and resistance factors will provide more consistent designs for a wide range of environmental conditions, types of risers, water depths, etc. Alternatively, one may go all the way to a reliability-based design of the risers. Both of these approaches require a probabilistic model of riser failure that includes long-term environmental variations, short-term response of the riser, and a characterization of ultimate limit states.

This study demonstrates a practical approach for the reliability analysis of risers under Gulf of Mexico severe-storm and long-term environments. This study considers failure under extreme loads, wave-cycle fatigue, and fatigue associated with vortex-induced vibrations (VIV). Although the original plan was to consider a top-tensioned riser and a steel-catenary riser (SCR), this study focused on the analysis of a 1000 meter long top-tensioned riser from the Marlin Tension Leg Platform. Consideration of SCRs is limited to a brief discussion in Section 5.

Results for each type of loading include failure probabilities at various locations in the riser, the relative importance of the various Type-I and Type-II uncertainties, and additional sensitivity results. The failure probabilities provide information on the implied reliability of current designs, which is useful for future calibration efforts. The importance factors and other sensitivity results provide guidance for the development of future, more refined, reliability models and for the development of reliability-based LRFD procedures for risers.

1.2 ROADMAP

Section 2 of this report considers extreme loads, Section 3 considers wave-cycle fatigue, and Section 4 considers VIV fatigue. The organization of each of these section follows the same general outline, as follows: (a) metocean model, (b) model for global response (not present in Section 4), (c) model for stresses in riser, (d) reliability calculations, and (e) results. Finally, Section 5 contains a summary of results and discusses the issues that may arise in performing similar analyses for SCRs.

2. Analysis of Extreme Loads from Hurricanes

2.1 INTRODUCTION

The inputs to a reliability analysis for extreme loads on risers consist of a joint-probability model for the waves, wind, and current during severe hurricanes, models for the calculation of vessel motions given the metocean conditions, models for the calculation of stresses in the riser given the metocean conditions and global response, and limit-state models that define the occurrence of failure or other undesirable outcomes. All these inputs are then used to construct a reliability model, which is used to calculate the annual probability of failure and to investigate other combinations of parameters of interest for design.

Throughout this analysis, we distinguish between aleatory (or Type-I) and epistemic (or Type-II) uncertainties.

2.2 HURRICANE METOCEAN MODEL

Past studies of TLP global response (e.g., Banon et al,. 1994; Winterstein and Kumar, 1994) have used joint-probability models where the significant wave height Hs is the primary quantity. Wind speed, current, and other quantities are specified by means of conditional distributions given Hs.

This study will utilize wind speed Vw as the primary variable. This choice is motivated by both meteorological and engineering reasons. Wind is the driving mechanism that generates waves and currents, so it is natural to model wind as the primary quantity. In addition, the wind-driven mean offset and slow drift are the major causes for extreme stresses on the risers, as will be seen in Section 2.7. We will also use a model in which Hs is the primary quantity, for the sake of comparison.

The wind, waves, and current will be assumed to act in the same direction, and this direction will be taken in Section 2.3 as the direction in which the vessel response is higher. This conservative assumption is frequently made in the analysis of extreme riser response. Explicit consideration of directionality is necessary in the analysis of steel catenary of lazy-wave risers for FPSOs.

The distributions described below for wind, wave, and current apply to the 90-minute portion of the storms with the highest wind speed Hs.

2.2.1 Base Model: Use Wind Speed as Primary Quantity

The distribution for the annual maximum wind speed (1-hour mean at 10 m elevation) was provided by G. Berek and is based on the consensus estimates developed by the API Wave Force Task Group in 1993. After algebraic manipulation and unit conversions, this distribution may be written in Gumbel form as:

$$F_{V_{W,\text{annual max}}}(v_w)=\exp\left\{-5.04\exp\left(-\frac{v_w(\text{m/s})}{6.66}\right)\right\} \tag{2-1}$$

where v_w is the wind speed in m/s.

This distribution of annual maximum wind speed can be transformed into an event-based model, where are interested only in rare storms. Considering only those storms with wind speeds greater than 26.1 m/s (which have a recurrence rate $\nu=0.1$ events/yr, according to Eq. 2-1), we obtain that the distribution of wind speed during each events is given by

$$F_{V_w}(v_w)=1-\exp\left(\frac{v_w(\text{m/s})-26.1}{6.66}\right); \qquad v_w\geq 26.1\text{ m/s} \tag{2-2}$$

Together with the assumption that the storms of interest constitute a Poisson process with a rate $\nu=0.1$events/yr, the above equation predicts a distribution of annual maxima that is identical (in the upper tail) to the distribution in Equation 2-1. Epistemic uncertainty in the wind speed distribution is characterized by means of a 10% uncertainty in the scale parameters of 6.66.

For the distribution of Hs given Vw, we use the 25% rule (Cooper, 1988), which predicts a mean Hs equal to 0.25 times the wind speed at an elevation of 20 meters. Assuming a ratio of 0.92 between the wind speeds at 10 and 20 meters elevation (obtained using the wind profile in the 1993 API-RP2A), and using the standard deviation based on Cooper's rms errors, we obtain

$$H_S(m)|V_w:\begin{cases}\text{mean}=0.27V_w\,(\text{m/s})\\ \sigma=0.75\text{ m}\end{cases} \tag{2-3}$$

The associated conditional distribution of Hs|Vw is assumed to be lognormal.

The conditional distribution for the wave peak-period Tp is obtained from values developed by the API Wave Force Task Group in 1993 (provided by G. Berek), which may be represented by a linear equation. The associated coefficient of variation was taken from Winterstein and Kumar (1994). The resulting model is of the form:

$$T_P\,(\text{sec})|Hs:\begin{cases}\text{mean}=8.18+0.54H_S\,(\text{m})\\ COV=6\%\end{cases} \tag{2-4}$$

The associated conditional distribution of Tp|Hs is assumed to be lognormal.

The conditional distribution of mixed-layer current speed is obtained from values developed by the API Wave Force Task Group in 1993 (provided by G. Berek), which may be represented by a linear equation. The associated coefficient of variation was selected by consensus of the participants. The resulting model is of the form:

$$V_C\,(m/s)|Hs:\begin{cases}\text{mean}=-0.32+0.12H_S\,(\text{m})\\ COV=10\%\end{cases} \tag{2-5}$$

The associated conditional distribution of Vc|Hs is assumed to be lognormal. In addition to the aleatory uncertainty indicated by the COV above, we consider a 10% epistemic uncertainty in the current velocity for a given Hs. For the sake of consistency in our approach to using Vw as the primary quantity, a model of the form Vc|Vw would have been preferred.

2.2.2 Alternative Model: Use Hs as Primary Quantity

The distribution for the annual maximum Hs was provided by G. Berek and is based on the consensus estimates developed by the API Wave Force Task Group. This distribution may be written in Gumbel form as:

$$F_{H_{S,\text{annual max.}}}(h_s)=\exp\left\{-44.09\exp\left(-\frac{h_s(\text{m})}{1.40}\right)\right\} \tag{2-6}$$

This distribution can be transformed into an event-based model. Considering only those storms with a Hs>8.52 m (which have a recurrence rate $\nu=0.1$ events/yr, according to Eq. 2-6), we obtain that the distribution of Hs during each events is given by

$$F_{H_S}(h_s)=1-\exp\left(\frac{h_s(\text{m})-8.52}{1.40}\right); \qquad h_s\geq 8.52\text{ m} \tag{2-7}$$

Together with the assumption that the storms of interest constitute a Poisson process with a rate $\nu=0.1$events/yr, the above equation predicts a distribution of annual maxima that is identical (in the upper tail) to the distribution in Equation 2-6.

The conditional distribution of Vw|Hs is obtained from values developed by the API Wave Force Task Group, which may be represented by a linear equation. The associated coefficient of variation was taken from Winterstein and Kumar (1994). The resulting model is of the form:

$$V_w\,(m/s)|Hs\colon \begin{cases}\text{mean}=0.5+3.44\,H_S\,(\text{m})\\ COV=12\%\end{cases} \tag{2-8}$$

2.2.3 Comparison of Marginal Models for Vw and Hs

It is useful to compare the marginal distributions of wind speed and Hs that result from these two models. Figure 2-1 shows the distributions of wind speed, as well as the wind speed associated with the 100-year Hs in API-RP2A (1993) for locations in the western Gulf of Mexico. Although the two distributions predict similar values at annual exceedence probabilities of 0.01 (or 100 years), they differ substantially at lower probabilities, with the model derived from the Hs distribution predicting lower wind speeds.

Similarly, Figure 2-2 shows the distributions for Hs, as well as the 100-year Hs in API-RP2A (1993) for locations in the western Gulf of Mexico and the distribution of Winterstein and Kumar (1994, which is inferred from Banon et al., 1994). Again, all distributions predict similar values at annual exceedence probabilities of 0.01 (or 100 years) but they differ substantially at lower probabilities. The distribution obtained with Vw as primary (our base-case model) predicts the highest values of Hs in the upper tail.

One obtains different results by using Hs or Vw as primary variables because the conditional distributions of Hs|Vw and Vw|Hs are not entirely consistent with the associated marginal distributions, as a result of using different data sets (or subsets of the original data set) or as a result of the functional forms selected for the conditional distributions. These effects are particularly important in the tails. Thus, if wind dominates the response of a structure (as is the case here), it is preferable to select Vw as the primary variable in order to have a more faithful representation of its distribution.

It is also worth noting that the Hs-based and the Winterstein-Kumar distributions in Figure 2-2 differ substantially in the upper tail, even though they are derived from the same GUMSHOE hindcasts. This is believed to be the result of fitting different models to the same data, when those data span a limited number of years.

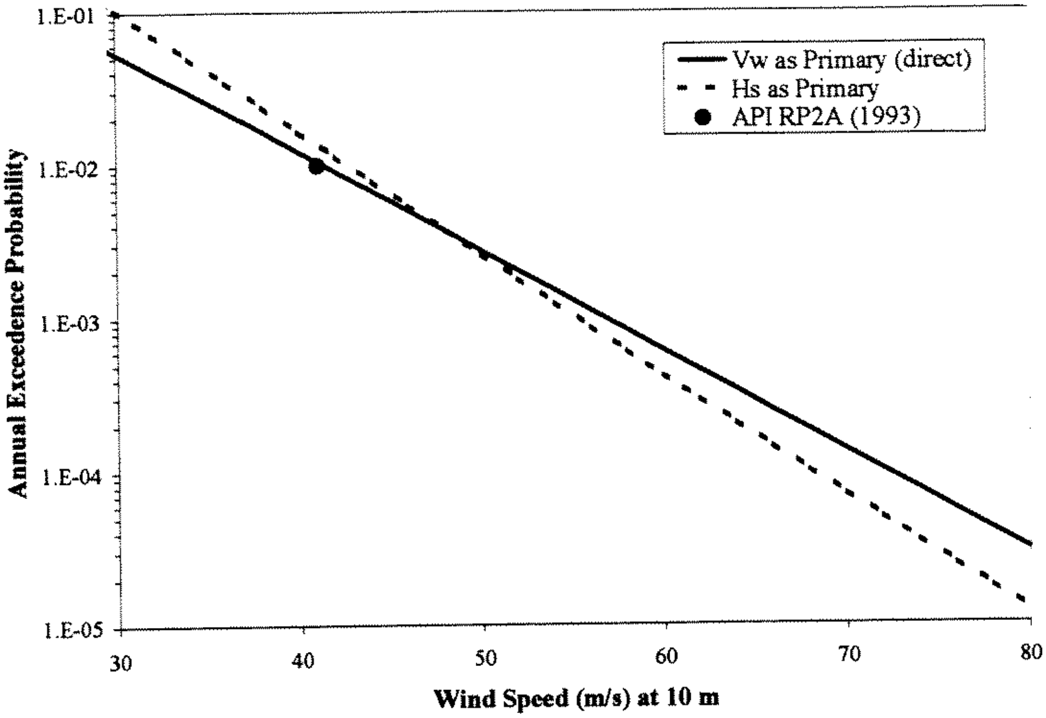

Figure 2-1. Comparison of distributions of wind speed Vw, as obtained with different choices for the primary meteorological quantity in the probabilistic model.

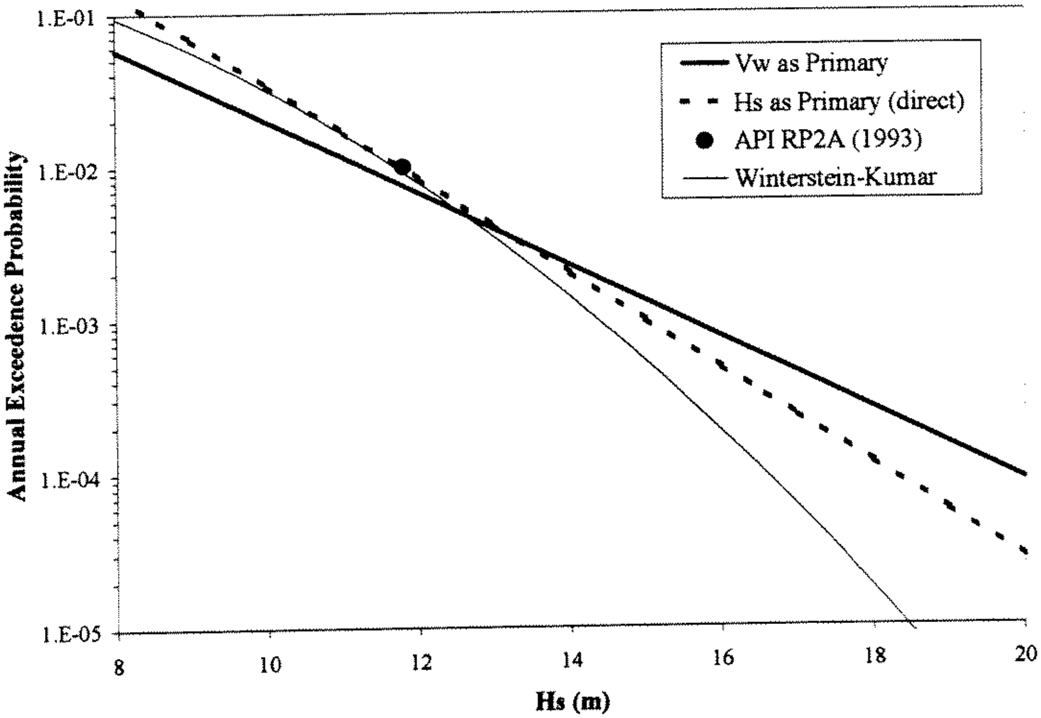

Figure 2-2. Comparison of distributions of significant wave height Hs, as obtained with different choices for the primary meteorological quantity in the probabilistic model.

2.3 GLOBAL RESPONSE MODEL

Although this study is not directly interested in the motion of the vessel or the forces acting on the tendons, it is necessary to calculate the mean offset and the low-frequency and wave-frequency motions of the vessel during a given sea state, because these quantities have a significant effect on the stresses that the riser will experience.

For the purposes of this study, it is most convenient to express the global-response model as a set of parametric expressions and/or small tables. Because no such models had been developed for the Marlin platform, we had to derive these models on the basis of configuration and response data that for Marlin that were provided by Mike Spillane of Atlantia/OSAC and Jeff Geyer of Amoco. In addition, we checked the predictions from the resulting models against Marlin results obtained by Amoco to verify their accuracy.

Conceivably, one could have incorporated Amoco or other consultant's software for global-response calculations within the reliability software, instead of relying on parametric expressions. This would have been complicated by the proprietary nature of the software for global-response calculations.

2.3.1 Relation Between Mean Offset, Mean Horizontal Force, and Horizontal Stiffness

We can establish the relationship between the mean offset and the horizontal force by considering the horizontal and vertical forces acting on the platform, under the assumption of no tendon elongation. The horizontal forces acting on the vessel are the mean force F_m (from wind, currents, and waves) and the horizontal component of tendon force. The vertical forces acting on the vessel are the vessel weight, the buoyancy force under no offset, the additional buoyancy arising from set-down, and the vertical component of the tendon force. By imposing equilibrium and considering the geometric relationship of tendon length, mean offset, set-down, and the angle between the tendons and the vertical direction, one obtains the following relationship between mean offset X_m and mean force F_m:

$$F_m = \frac{T_0 X_m}{L} + K_{wp} X_m \left(\frac{1}{\sqrt{L^2 - X_m^2}} - 1 \right) \tag{2-9}$$

The other quantities appearing in this equations, and their values for Marlin, are given in Table 2-1. This table also contains other platform parameters, which will be introduced later in this Section.

Table 2-1 Marlin Configuration and Response Parameters used in the Calculation of Global Responses

Symbol	Description	Value
L	Tendon length	3158 feet [1]
T_0	Tendon Pre-tension (all tendons)	1.293E4 kips [1]
K_{wp}	Water-plane stiffness (total cross-sectional area of TLP columns times weight density of water)	490.9 kips/ft [1]
M	Vessel Mass (including added mass)	3.31E6 slugs [2]
ζ	Damping Ratio	0.18 [1]
C_{fw}	Wind force coefficient	0.0393 kip/fps^2 [1]

[1] Values provided by, or derived from values provided by, Jeff Geyer

[2] Value provided by Mike Spillane

For computational simplicity, one can approximate the above equation by the linear and cubic terms of the Taylor expansion about $X_m=0$ and then solve the cubic equation for F_m. The resulting expression for the horizontal offset associated with a given horizontal force is:

$$X_m(F_m)=a(F_m)^{1/3}-\frac{2}{3}\frac{T_0 L}{K_{wp}a(F_m)^{1/3}} \tag{2-10}$$

where

$$a(F_m)=F_m\frac{L^2}{K_{wp}}+\left(\frac{L}{3K_{wp}}\right)^{3/2}\sqrt{8T_0^3+27F_m^2 L K_{wp}} \tag{2-11}$$

and $F_m=F_W+F_V+F_C$ is the mean or static force (i.e., the sum of the static forces due to wind, waves, and current, which are assumed to act in the same direction and will be calculated below).

We can also obtain the horizontal stiffness by differentiating the cubic equation, obtaining

$$K_h(X_m)=\frac{T_0}{L}+\frac{3}{2}\frac{K_{wp}}{L^2}X_m^2 \tag{2-12}$$

This stiffness may be used to calculate the slow-drift period T_Z as

$$T_Z=2\pi\sqrt{\frac{M}{K_h(X_m)}} \tag{2-13}$$

Periods will decrease slightly for the more severe environmental conditions, as a result of increased stiffness. For instance, the slow-drift periods associated with the 50- and 1000-year hurricane environmental criteria are 130 and 116 seconds.

2.3.2 Wind Forces and Offsets

The static wind force is calculated using the expression

$$F_w = \frac{1}{2}\rho_a C_S A V_Z^2 = C_{fw} V_W^2 \tag{2-14}$$

where ρ_a is the density of air, C_S is a shape coefficient, A is the projected area, V_Z is the 1-hour average velocity at the elevation of the center of effort (180 feet), C_{fw} is the wind-force coefficient (given in Table 2-1) and V_w is the wind speed (m/s) at 10 m elevation.

Calculation of the low-frequency offset from fluctuating wind requires consideration of the wind spectrum and of the dynamic characteristics of the vessel. The spectrum of wind-velocity fluctuations (about V_Z) is characterized by means of the Froya spectrum. This spectrum has been adopted by the Norwegian Petroleum Directorate (NPD) for inclusion in its offshore guidance notes and is being recommended for inclusion in the proposed ISO offshore standard. The spectral density function of wind velocity takes the form:

$$S_{uu}(f) = \frac{320\left(\frac{V_W}{10}\right)^2 \left(\frac{z}{10}\right)^{0.45}}{\left(1+\tilde{f}^{\,n}\right)^{5/(3n)}} \tag{2-15}$$

where $S_{uu}(f)$ has units of $m^2 s^{-2}/Hz$, z is height above sea level (m), n=0.468, and

$$\tilde{f} = 172 f \left(\frac{z}{10}\right)^{2/3} \left(\frac{V_W}{10}\right)^{-0.75} \tag{2-16}$$

Following the linearization approach in Section 6.2.3 of API-RP2A, and assuming that the aerodynamic admittance is unity (as recommended by the above reference for low frequencies), the spectral density function of the fluctuating wind force is then

$$S_{ff}(f) = S_{uu}(f)\,\frac{4F_W^2}{V_Z^2} \tag{2-17}$$

where F_W is the static wind force defined earlier.

Calculation of the rms offset due to fluctuating wind uses the force spectrum defined above and the transfer function of the vessel (which depends on the vessel slow-drift period and damping ratio defined earlier), resulting in the expression

$$X^2_{rmsLFW} = \int_0^\infty \frac{1}{2\pi} S_{ff}\left(\frac{\omega}{2\pi}\right) \frac{1}{\left(\omega^2-\omega_0^2\right)^2 + 4\zeta^2\omega_0^2\omega^2}\, d\omega \tag{2-18}$$

where $\omega_0 = 2\pi/T_Z$ is the slow-drift frequency in rad/sec. By applying the narrow-band approximation (i.e., assuming that most of the contribution to the integral above comes from frequencies near ω_0), one obtains the expression

$$X_{rmsLFW}=\frac{1}{K_h}\sqrt{\frac{\pi}{4\zeta}S_{ff}\left(\frac{1}{T_Z}\right)\left(\frac{1}{T_Z}\right)} \qquad (2\text{-}19)$$

For the sake of simplicity in the implementation, we fit the following functional form to the rms values obtained by numerical integration of equation 2-18 over a range of wind speeds associated with return periods from 10 to 1000 years:

$$X_{rmsLFW}=c_1\frac{V_W^{3/2}}{\zeta^{1/2}K_h^{3/4}}\left[1+\left(c_2\frac{K_h^{1/2}}{V_w^{3/4}}\right)^{0.468}\right]^{-\frac{5}{6\times 0.468}} \qquad (2\text{-}20)$$

where V_W is given in feet/sec, K_h is given in kips/foot, $c_1=97.7$, and $c_2=2.7\times10^5$. The values of c_1 and c_2 are specific to Marlin; the functional form is based on the equations above and is applicable to other platforms.

The static wind force and rms offset calculated here (using the API wind spectrum instead of the Froya spectrum) were checked against values calculated by Amoco for the 50, 100, and 1000-year conditions, and found to be in agreement.

2.3.3 Wave Forces

The (velocity)^2 terms in the calculation of wave forces acting on the TLP vessel give rise to a static force and a low-frequency force. The static force (or wave-drift force) is given by the equation:

$$F_v=2\int_0^{\infty}S_{\eta\eta}(\omega)\,C_{wd}(\omega)d\omega \qquad (2\text{-}21)$$

where $S_{\eta\eta}(\omega)$ is the power spectral density function of wave elevation (units of ft^2/(rad/sec); we use a Jonswap shape with $\gamma=2.4$) and $C_{wd}(\omega)$ is the wave-drift coefficient (a property of the vessel). Figure 2-3 shows the wave-drift coefficient for Marlin as a function of Tz.

Because the waves of interest in these calculations have peak periods greater than 10 seconds, most of the contribution to the integral above comes from the peak near 7 sec. Figure 2-4 shows the calculated wave drift force (normalized by Hs^2) for a range of wave peak periods Tp. The figure also shows the values calculated by Amoco for the 10, 50, 100, and 1000-year sea states (provided by J. Geyer). In view of the discrepancy, which is believed to be the result of not

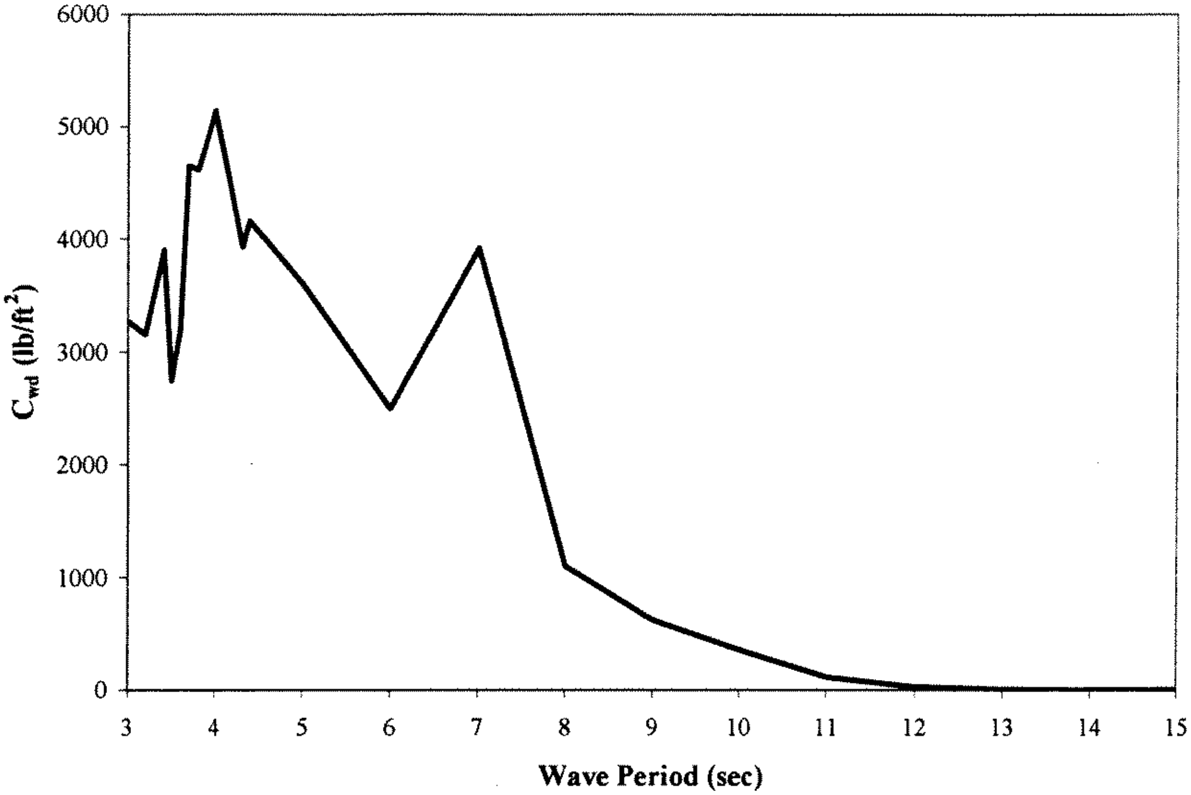

Figure 2-3. Wave-drift coefficient for Marlin (45-degree direction). Computed from values provided by J. Geyer.

including viscous drag forces, this study will use the Amoco values. The Amoco values will be approximated by the relation

$$F_{wd}=12.49T_p^{-1.636}H_S^2$$

where F_{wd} has units of kips, Tp has units of seconds, and Hs has units of feet.

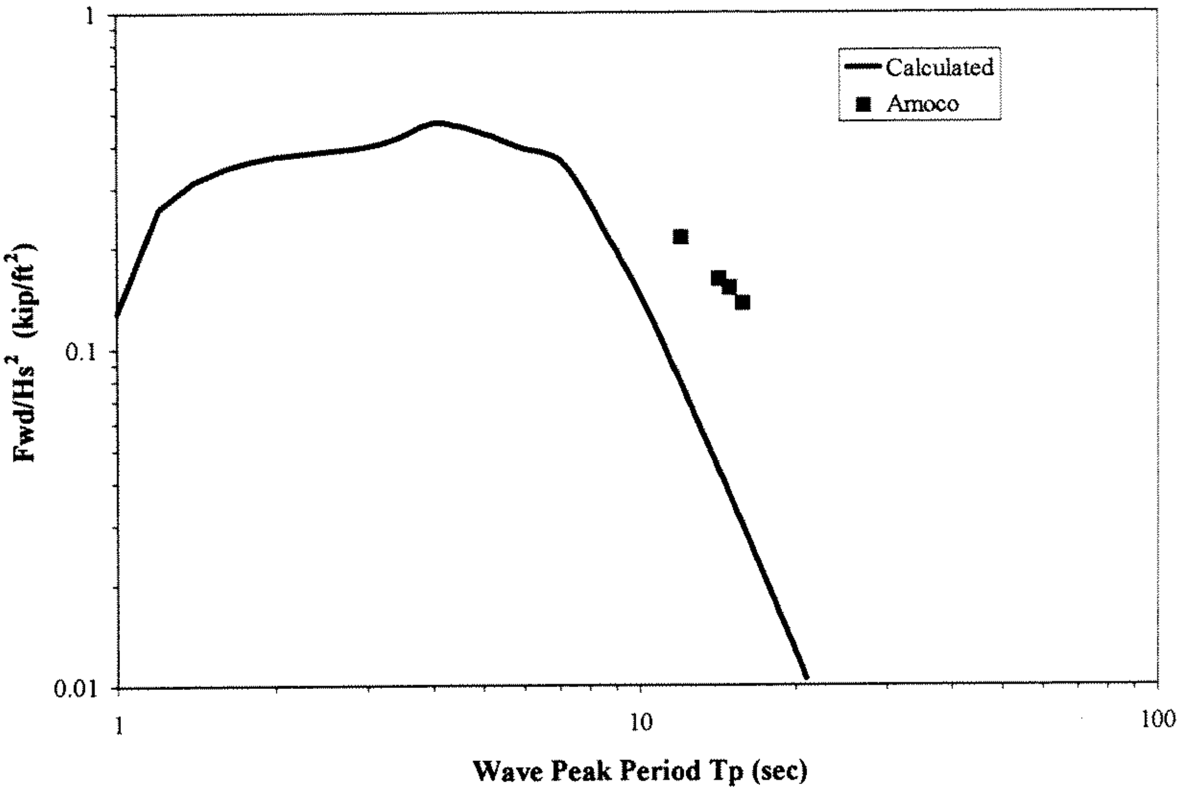

Figure 2-4. Wave drift force as a function of wave peak period Tp: calculated values versus Amoco values.

The power spectrum for the second-order low-frequency force due to waves is also given in terms of the wave spectrum and the wave-drift coefficient C_{wd}. The equation for the spectrum takes the form:

$$S_{ff}(\omega)=8\int_{0}^{\infty} S_{\eta\eta}(\omega+\Omega)\, S_{\eta\eta}(\omega)\left[C_{wd}(\Omega+\frac{\omega}{2})\right]^{2} d\Omega \qquad (2\text{-}23)$$

Calculations using this equation indicate that $S_{ff}(\omega)$ is nearly flat for ω in the range from 0 to 0.006 rad/sec (corresponding to periods of 100 sec or more). Thus, we can approximate $S_{ff}(\omega)$ by means of $S_{ff}(0)$. Figure 2-5 shows the calculated value of $S_{ff}(0)$ (normalized by Hs^4) as a function of wave period Tp, which we approximate as

$$\frac{S_{ff}(0)}{Hs^{4}}\approx 0.421\left[\max(\frac{T_{P}}{7},1)\right]^{-6.754} \qquad (2\text{-}24)$$

where S_{ff} has units of kips, Hs has units of feet, and Tp has units of seconds. Invoking again the narrow-band assumption, we obtain the following expression for the rms offset due to second-order wave forces:

$$X_{rms2V}=\frac{1}{K_h}\sqrt{\frac{\pi}{4\zeta}S_{ff}\left(\frac{2\pi}{Tz}\right)\left(\frac{2\pi}{T_Z}\right)}\approx\frac{1}{K_h}\sqrt{\frac{\pi}{4\zeta}S_{ff}(0)\left(\frac{2\pi}{T_Z}\right)} \tag{2-25}$$

This equation differs slightly from equation 2-19 because the spectral density functions for wind and wave forces have different units (force^2/Hz vs force^2/(rad/sec)). The rms offsets calculated using equations 2-24 and 2-25 are consistent with values calculated by Amoco.

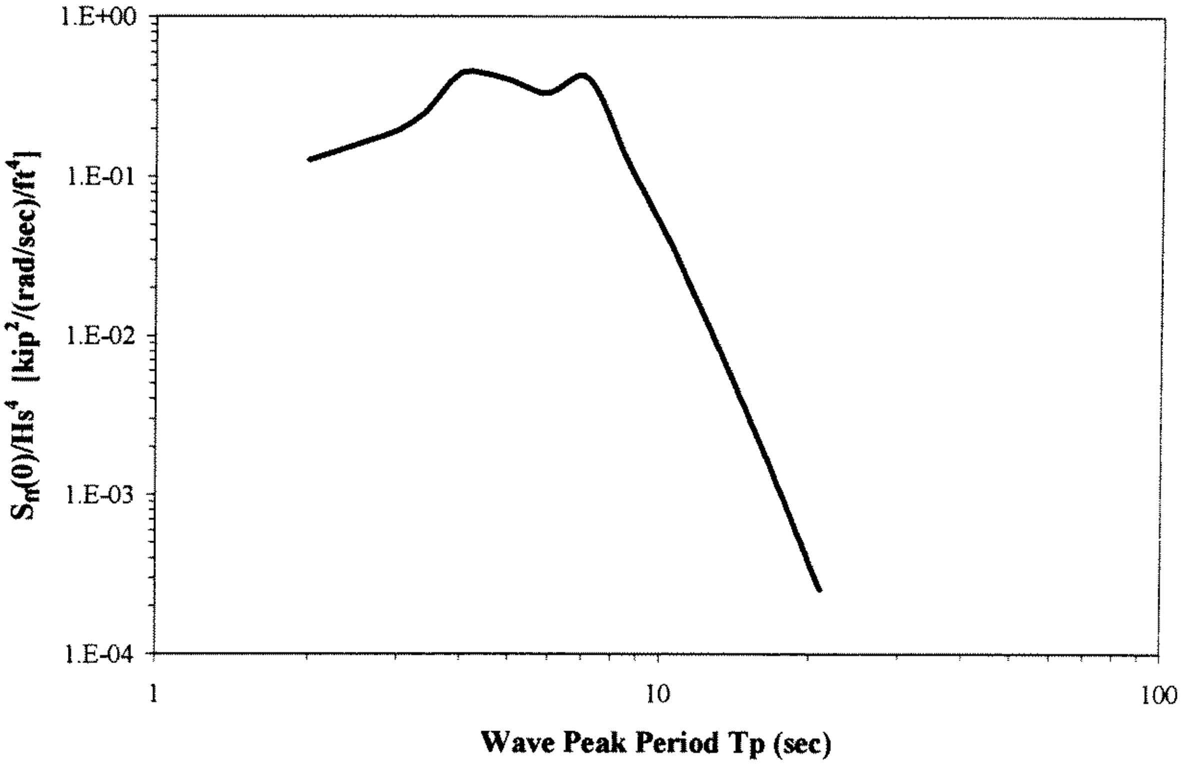

Figure 2-5. Calculated value of the spectral density function of low-wave force at zero frequency $S_{ff}(0)$ (normalized by Hs^4) shown as a function of the wave peak period Tp.

The combined low-frequency rms offset from wind and waves is computed from the respective rms offsets as:

$$X_{rmsLF}=\sqrt{X^2_{rmsLFW}+X^2_{rms2V}} \tag{2-26}$$

Under the narrow-band approximation invoked earlier, the zero-crossing period of the low-frequency motion is the same T_Z calculated earlier from the platform mass and stiffness, and the associated bandwidth is a function of the damping ratio ζ.

In addition to these static and low-frequency forces, the first-order forces acting on the vessel introduce wave-frequency motions, which are characterized by the RAO (response amplitude operator) shown in Figure 2-6

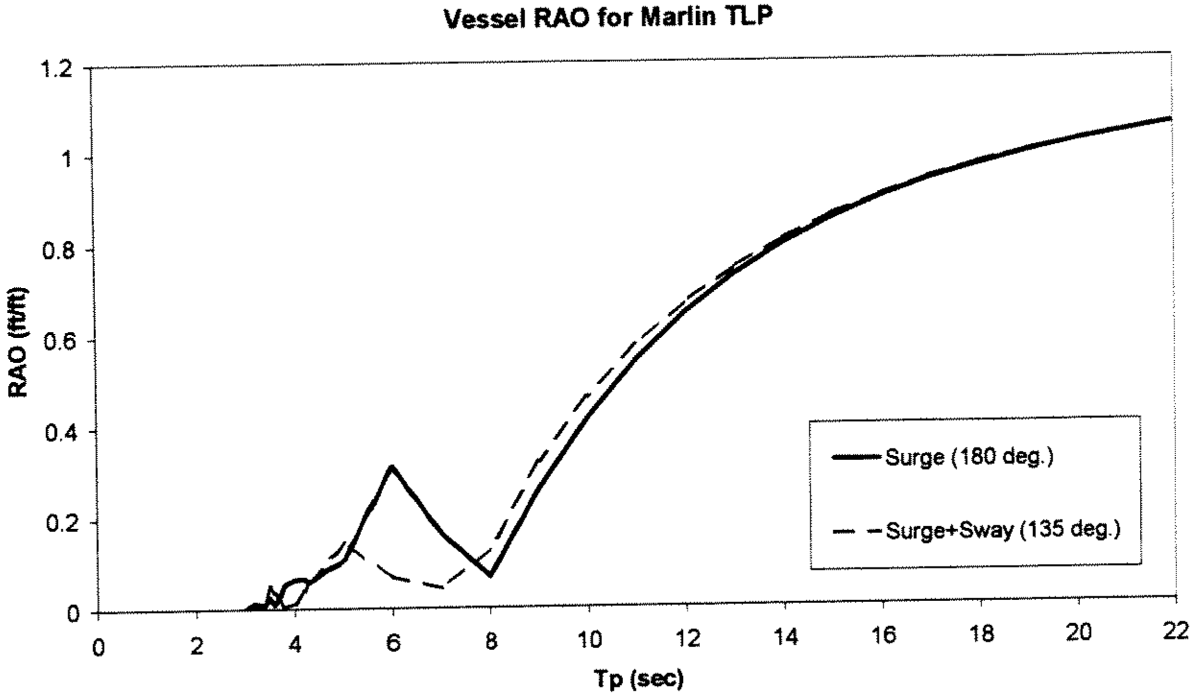

Figure 2-6. Vessel RAO for Marlin TLP. Source: J. Geyer.

2.3.4 Current Force

The expression for the horizontal force due to current is derived by fitting an equation to the values calculated by Amoco for the 10, 50, 100, and 1000-year environmental criteria. Theory suggests an expression of the form $F_C = C_{fc} V_c^2$, but this study obtains an expression with a slightly higher exponents, i.e.,

$$F_C(\text{kips}) = 11.86\left[V_C(\text{fps})\right]^{2.3} \tag{2-27}$$

because Amoco uses profiles that become slightly deeper for the more severe sea states.

2.3.5 Type-II Uncertainties in Global Response

Recognizing the limitations of the models used to compute global responses, this study considers Type-II uncertainty in the global-response quantities, namely static force, low-frequency rms offset, and wave-frequency RAO. We characterize each uncertain quantity by introducing a lognormal variable that represents the relative deviation of the calculated value from the true value of the quantity. The values chosen for the means and coefficients of variation of these variables, which are based on the values used by Banon et al. (1994), will be presented in Section 2.6.

2.4 CALCULATION OF EXTREME STRESSES

2.4.1 Experimental Design and TIARA Runs

This study uses the TIARA software, under license from Shell, to calculate the stresses in the riser. Multiple TIARA runs are used to quantify the effects of uncertain parameters (both Type-I and Type-II) on riser stresses. The following quantities are varied:

2. Met-Ocean Variables
    a. Significant wave height Hs
    b. Wave peak period Tp given Hs
    c. Current velocity Vc given Hs

3. Global-response variables
    a. Mean vessel offset X_m (uncertainty includes deviation between true and calculated value and effect of scatter in Vw given Hs)
    b. Low-frequency rms vessel offset X_{rmsLF} (uncertainty includes deviation between true and calculated value and effect of scatter in Vw given Hs)
    c. Low-frequency zero-crossing period Tz
    d. Deviation of true RAO from assumed RAO (taken as a multiplicative factor that applies to all frequencies)

4. Riser Drag Coefficients
    a. C_d in the wave zone (upper 500 feet)
    b. C_d at depth (depths greater than 500 feet)

If one were to consider three values of Hs (say, those associated with 50, 100, and 1000-year return periods[1]) and consider all combinations of the remaining variables, one would have a total of $3\times2^8=768$ parameter combinations to run. Instead, this study uses a 2^{8-4} design[2] (Box and Draper, 1987) plus one central point for each value of Hs. The resulting total number of parameter combinations is $3\times(2^4+1)=51$. Table 2-2 shows the design matrix for each value of Hs. A value of ±1 in the design matrix indicates that the corresponding variable will be given a value equal to its conditional mean (given the values of all variables to its left) ±1.5 its conditional standard deviation. These calculations used preliminary forms of the metocean model and global-response models, as well as the final model for uncertainties in the Cd's and modeling errors (to be discussed in Section 2.5). The resulting values of all quantities in the experimental design are given in Table 2-3.

---

[1] For location 5 in the riser, additional runs were performed for the 10,000-year Hs.

[2] In the 2^{m-n} design, one generates all possible combinations of values (-1 or 1) of the first $m-n$ variables. For each one of these combinations, the values of the remaining n variables are generated in a manner that preserves orthogonality. In this way, one samples an m-dimensional space using only 2^{m-n} orthogonal points. See Box and Draper (1987) for further details.

Table 2-2 Design Matrix used to Generate Runs for Extreme-Load Analysis (for one value of Hs)

Tp	V_C	Xm	X_{rmsLF}	Tz	ϵ_{RAO}	Cd (<500')	Cd(>500')
0	0	0	0	0	0	0	0
-1	-1	-1	-1	-1	-1	-1	-1
-1	-1	-1	1	-1	1	1	1
-1	-1	1	-1	1	1	1	-1
-1	-1	1	1	1	-1	-1	1
-1	1	-1	-1	1	1	-1	1
-1	1	-1	1	1	-1	1	-1
-1	1	1	-1	-1	-1	1	1
-1	1	1	1	-1	1	-1	-1
1	-1	-1	-1	1	-1	1	1
1	-1	-1	1	1	1	-1	-1
1	-1	1	-1	-1	1	-1	1
1	-1	1	1	-1	-1	1	-1
1	1	-1	-1	-1	1	1	-1
1	1	-1	1	-1	-1	-1	1
1	1	1	-1	1	-1	-1	-1
1	1	1	1	1	1	1	1

Table 2-3 Parameter Values Used in TIARA Runs for Extremes

run no.	Hs(ft)	Tp(sec)	Curr(fps)	Xm (ft)	XrmsLF (ft)	Tz(sec)	ϵ_{RAO}	Cd(<500')	Cd(>500')
1	37.4	14.2	3.8	184.9	17.73	136	1.00	1.20	0.80
2	37.4	12.9	3.5	124.8	9.72	126	0.93	0.66	0.62
3	37.4	12.9	3.5	124.8	25.74	126	1.08	1.74	0.98
4	37.4	12.9	3.5	235.1	9.72	145	1.08	1.74	0.62
5	37.4	12.9	3.5	235.1	25.74	145	0.93	0.66	0.98
6	37.4	12.9	4.0	132.1	9.72	169	1.08	0.66	0.98
7	37.4	12.9	4.0	132.1	25.74	169	0.93	1.74	0.62
8	37.4	12.9	4.0	248.3	9.72	105	0.93	1.74	0.98
9	37.4	12.9	4.0	248.3	25.74	105	1.08	0.66	0.62
10	37.4	15.4	3.5	124.8	9.72	170	0.93	1.74	0.98
11	37.4	15.4	3.5	124.8	25.74	170	1.08	0.66	0.62
12	37.4	15.4	3.5	235.1	9.72	107	1.08	0.66	0.98
13	37.4	15.4	3.5	235.1	25.74	107	0.93	1.74	0.62
14	37.4	15.4	4.0	132.1	9.72	125	1.08	1.74	0.62
15	37.4	15.4	4.0	132.1	25.74	125	0.93	0.66	0.98
16	37.4	15.4	4.0	248.3	9.72	142	0.93	0.66	0.62
17	37.4	15.4	4.0	248.3	25.74	142	1.08	1.74	0.98
18	41.7	14.9	4.2	214.4	19.00	130	1.00	1.20	0.80
19	41.7	13.6	3.9	144.7	10.41	122	0.93	0.66	0.62
20	41.7	13.6	3.9	144.7	27.58	122	1.08	1.74	0.98
21	41.7	13.6	3.9	272.4	10.41	136	1.08	1.74	0.62
22	41.7	13.6	3.9	272.4	27.58	136	0.93	0.66	0.98
23	41.7	13.6	4.5	153.2	10.41	164	1.08	0.66	0.98
24	41.7	13.6	4.5	153.2	27.58	164	0.93	1.74	0.62
25	41.7	13.6	4.5	287.9	10.41	98	0.93	1.74	0.98
26	41.7	13.6	4.5	287.9	27.58	98	1.08	0.66	0.62
27	41.7	16.2	3.9	144.7	10.41	166	0.93	1.74	0.98
28	41.7	16.2	3.9	144.7	27.58	166	1.08	0.66	0.62
29	41.7	16.2	3.9	272.4	10.41	101	1.08	0.66	0.98
30	41.7	16.2	3.9	272.4	27.58	101	0.93	1.74	0.62
31	41.7	16.2	4.5	153.2	10.41	121	1.08	1.74	0.62
32	41.7	16.2	4.5	153.2	27.58	121	0.93	0.66	0.98
33	41.7	16.2	4.5	287.9	10.41	133	0.93	0.66	0.62
34	41.7	16.2	4.5	287.9	27.58	133	1.08	1.74	0.98
35	46.9	15.8	4.7	251.6	20.53	123	1.00	1.20	0.80
36	46.9	14.4	4.4	169.8	11.25	118	0.93	0.66	0.62
37	46.9	14.4	4.4	169.8	29.81	118	1.08	1.74	0.98
38	46.9	14.4	4.4	319.7	11.25	125	1.08	1.74	0.62
39	46.9	14.4	4.4	319.7	29.81	125	0.93	0.66	0.98
40	46.9	14.4	5.1	179.9	11.25	158	1.08	0.66	0.98
41	46.9	14.4	5.1	179.9	29.81	158	0.93	1.74	0.62
42	46.9	14.4	5.1	338.0	11.25	90	0.93	1.74	0.98
43	46.9	14.4	5.1	338.0	29.81	90	1.08	0.66	0.62
44	46.9	17.2	4.4	169.8	11.25	160	0.93	1.74	0.98
45	46.9	17.2	4.4	169.8	29.81	160	1.08	0.66	0.62
46	46.9	17.2	4.4	319.7	11.25	93	1.08	0.66	0.98
47	46.9	17.2	4.4	319.7	29.81	93	0.93	1.74	0.62
48	46.9	17.2	5.1	179.9	11.25	116	1.08	1.74	0.62
49	46.9	17.2	5.1	179.9	29.81	116	0.93	0.66	0.98
50	46.9	17.2	5.1	338.0	11.25	121	0.93	0.66	0.62
51	46.9	17.2	5.1	338.0	29.81	121	1.08	1.74	0.98

2.4.2 TIARA Calculations

The TIARA program was used to calculate stresses in the riser for each combination of parameters in Table 2-4. In addition to the parameters in this table, other important inputs to TIARA are the riser configuration, the operational conditions (e.g., internal pressure), and the vessel's wave-frequency RAO. The TIARA runs were performed by Stress Engineering Services.

Figure 2-7 shows the production configuration of the Marlin riser and the locations for where stresses were calculated. The following quantities were reported at each location and for each run:

1. Mean stress due to pretension and vessel offset σ_{m1}
2. Mean stress due to local hydrodynamic forces on the riser σ_{m2}
3. Hoop and radial stresses
4. Wave-frequency rms stress (and associated Tz, Ochi factor, and bandwidth)
5. Low-frequency rms stress
6. Maximum stresses and von Mises stresses (these were calculated by using the Ochi factors generated by TIARA; they were not used in the reliability calculations).

The reason for decomposing the mean stress into σ_{m1} and σ_{m2} is that the former has negligible uncertainty (it is essentially a static problem) and the latter carries significant uncertainty (see Section 2.5). All stresses are measured at the midpoint of the riser wall and represent a combination of bending and axial stresses (bending stresses are dominant).

Figure 2-8 shows the various stresses calculated by TIARA as a function of location for the 100-year Hs (run number 18). Based on these results, we select Locations 1 (highest mean, maximum, and von Mises stresses), 4 (highest compressive hoop stress), and 5 (highest mean, maximum, and von Mises stresses near the top of the riser).
Figure 2-8 also shows the importance of the mean stress, particularly at the bottom of the riser.

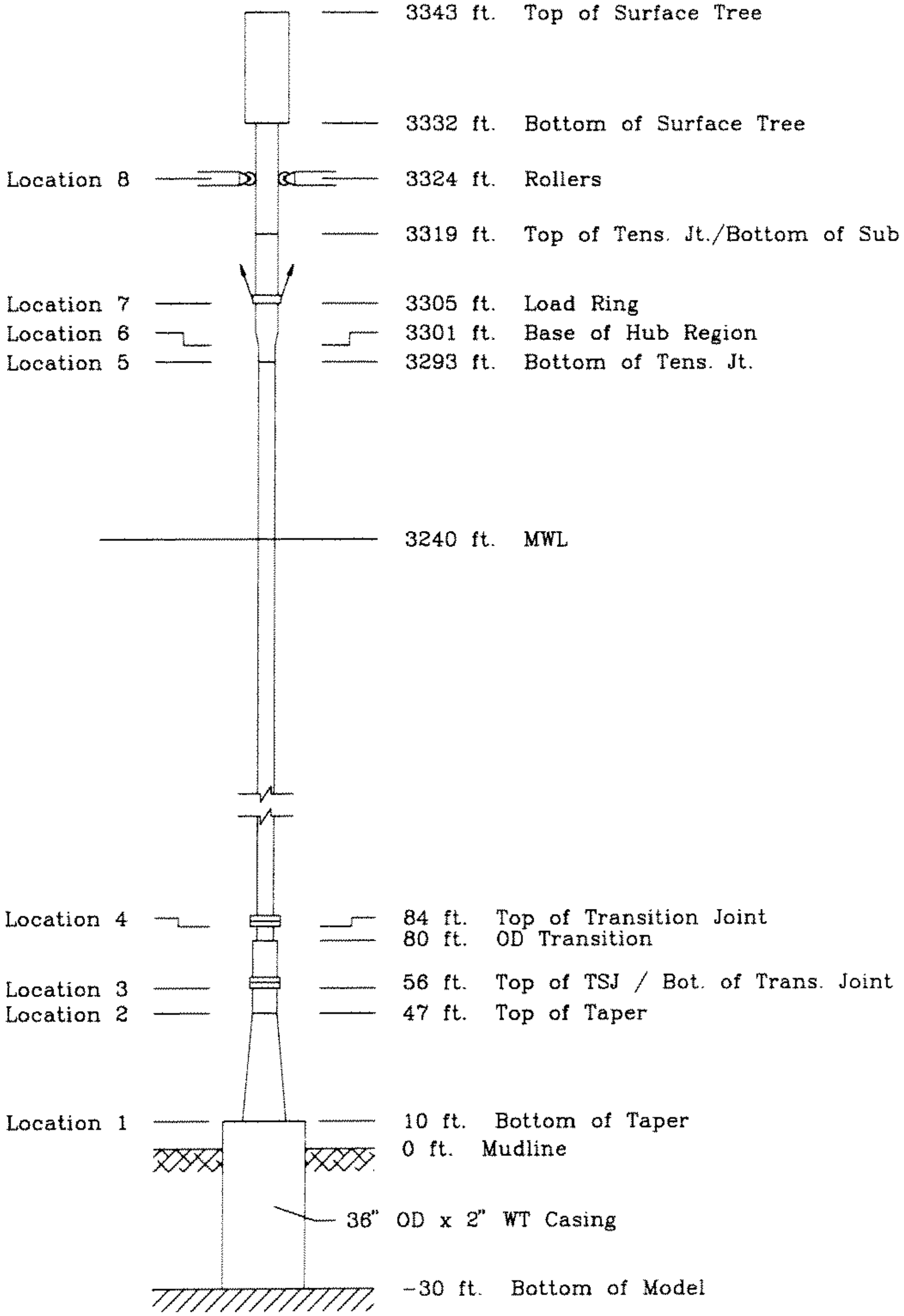

Figure 2-7. Diagram showing the Marlin riser and the locations of interest.

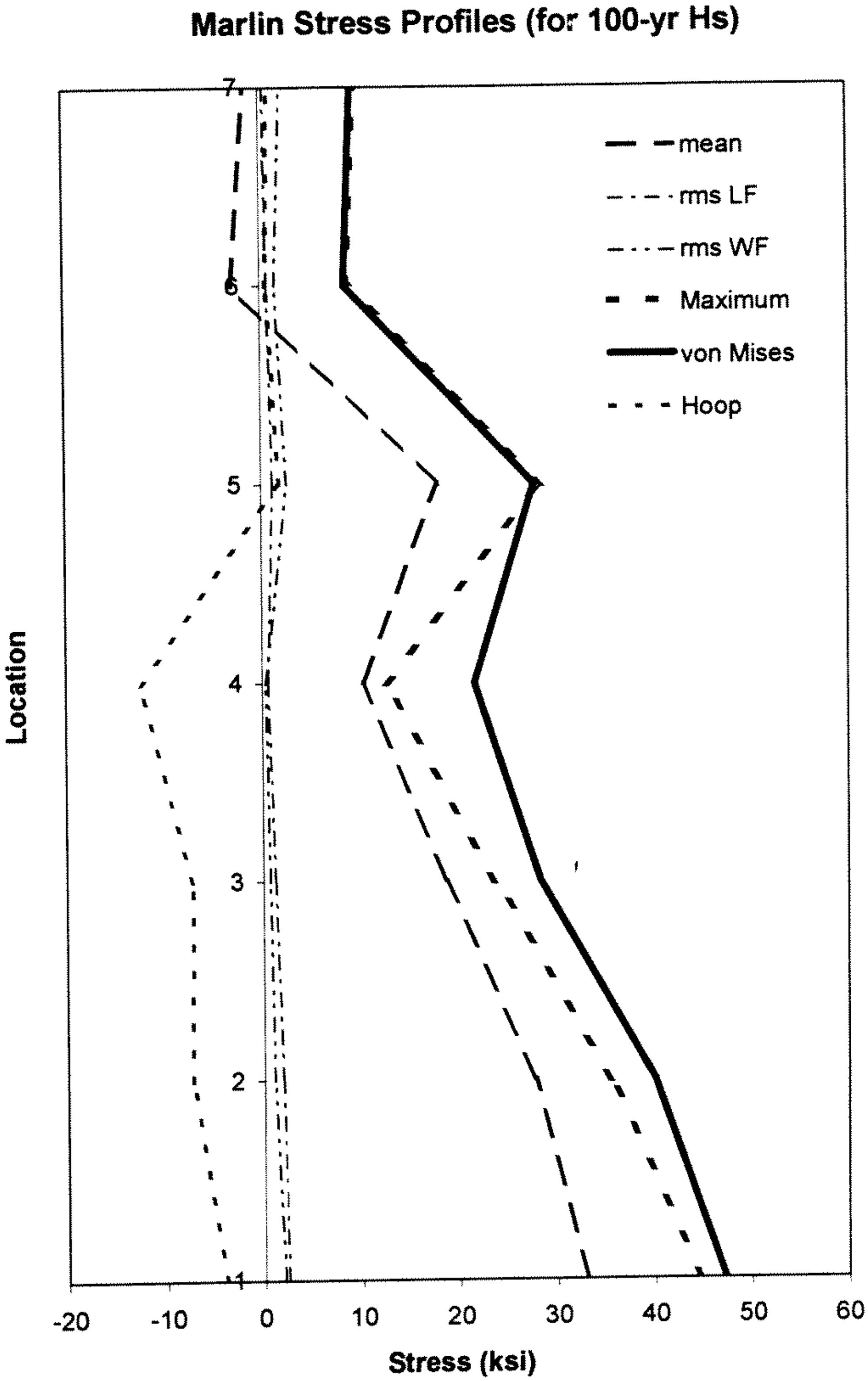

Figure 2-8. Stress profile along riser height (not to scale).

2.4.3 Fitting of Response Surfaces

We fit response surfaces for locations 1, 4, and 5 and for the following quantities: mean stresses σ_{m1} and σ_{m2}, low-frequency rms stress, wave-frequency rms stress, wave-frequency Tz, and wave-frequency bandwidth. The selection of functional forms is based on physical considerations and is kept as simple as possible. All response surfaces are fit by means of non-linear regression. The discrepancy between the TIARA results and the values predicted by the response surface is quantified by means of the residual standard deviation σ.

Response Surface for mean stress from pretension and mean offset σ_{m1}. This stress is due mainly to the geometric relations between the riser, the tensioner (much more flexible than the riser), and the tendons, as the vessel is offset laterally while maintaining a constant tendon length. For small angles, these relations may be approximated by polynomials on the mean offset X_m [ft].

$$\sigma_{m1}[\text{ksi}] = c_1 + c_2 X_m + c_3 X_m^2 \tag{2-28}$$

Table 2-4 shows the calculated coefficients and the standard deviation σ. At location 4, c3 has a negative value, which is counter-intuitive. The results labeled 4L are obtained after forcing c3 to 0. Figure 2-9 compares the values predicted by the response surface to the values calculated by TIARA. The σ values and the graphs indicate that the response surface matches the TIARA results very closely.

Table 2-4 Coefficients of Response Surface for Mean Stress from Pretension and Mean Offset σ_{m1}

Location	c1	c2	c3	σ [ksi]
1	4.692	0.116	6.39E-5	0.08
4	1.112	0.0445	-3.6E-5	0.02
4L	2.744	0.0282	0	0.14
5	11.72	0.0151	1.02E-4	0.12

Response surfaces for mean stress from direct hydrodynamic forces on riser σ_{m2}. One would expect these stresses to depend on Hs [ft], Vc [fps], and wave-zone Cd. Dependence on mean offset X_m is possible because X_m controls the mean tension on the riser and the angle between riser and tensioner. The resulting equation is of the form:

$$\sigma_{m2}[ksi] = \text{sign}(c_1) \times (|c_1| H_S + c_2 V_{curr})^{c_4} \, C_{d(<500')} \, X_m^{c_3} \tag{2-29}$$

Table 2-5 shows the calculated coefficients and the standard deviation σ. Figure 2-10 compares the values predicted by the response surface to the values calculated by TIARA. Figure 2-10 compares the values predicted by the response surface to the values calculated by TIARA.

Table 2-5 Coefficients of Response Surface for the Mean Stress from Direct Hydrodynamic forces on riser σ_{m2}

Location	c1	c2	c3	c4	σ [ksi]
1	0.00901	0.0718	0.146	3.656	0.06
4	0.0232	0.265	-0.983	3.676	0.01
5	-0.004146	0.283	0.105	2.210	0.21

Note that σ_{m2} is negative (helping) at location 5, because the rotation introduced by drag forces reduces the P-Delta moments from the surface tree. Note also that the magnitude of this stress is much greater at Location 5. This issue made it necessary to consider higher sea states in the development of the response surface for location 5. In addition, we will consider additional Type-II uncertainty in σ_{m2} for sea states higher than those considered here.

Response Surfaces for Low-frequency rms stress σ_{rmsLF}. Again, considering that this stress is controlled by geometric relations between the riser, the tensioner, and the tendons, one would expect a relation of the form

$$\sigma_{rmsLF} = f(X_m + X_{rmsLF}) - f(X_m) \tag{2-30}$$

where X_{rmsLF} is the low-frequency rms offset (due to wind and waves) and f() is a polynomial relation of the type used for σ_{m1} above (we use the resulting functional form, but not the numerical coefficients obtained for σ_{m1}). In addition, a drag term is required at location 5 (near the surface). The result is

$$\begin{aligned}\sigma_{rmsLF} = {} & c_1 X_{rmsLF} X_m + \frac{c_1}{2} X_{rmsLF}^2 + c_2 X_{rmsLF} \\ & + c_3 \left(\frac{X_{rmsLF}}{T_Z} + c_4 V_{curr} \right)^2 C_{d(<500')}\end{aligned} \tag{2-31}$$

Table 2-6 shows the calculated coefficients and the standard deviation σ. Figure 2-11 compares the values predicted by the response surface to the values calculated by TIARA. Note that the magnitude of the rms stress at location 4 is much smaller than at other locations.

Table 2-6 Coefficients of Response Surface for Low-Frequency rms Stress σ_{rmsLF}

Location	c1	c2	c3	c4	σ_{ln}
1	1.518E-4	0.0995	0	0	0.074
4	-5.94E-5	0.0432	0	0	0.026
4L	0	0.0295	0	0	0.14
5	1.06E-4	-0.0036	4.33	0.055	0.11

Response Surfaces for Wave-frequency rms stress σ_{rmsWF}. As in the case of the low-frequency rms motion, we use an expression of the type

$$\sigma_{rmsWF}=f(X_m+c\,H_S\,\epsilon_{RAO})-f(X_M) \tag{2-32}$$

where $c\,H_S\,\epsilon_{RAO}$ represents the rms wave-frequency vessel offset (recall that ϵ_{RAO} is a multiplier that represents deviation between the true and assumed the wave-frequency RAO of the TLP). An additional effect is the attenuation of wave-frequency motion near the bottom as a result of drag. The resulting equation is of the form

$$\sigma_{rmsWF}=\left[c_1\,(H_S\,M_{RAO})+c_2(H_S\,M_{RAO})\,X_m\right]C_{d(>500')}^{c_3} \tag{2-33}$$

Table 2-7 shows the calculated coefficients and the standard deviations. For location 5, this standard deviation is multiplicative, rather than additive. Note also that the scatter is greater than for other stresses. Figure 2-12 compares the values predicted by the response surface to the values calculated by TIARA.

Table 2-7 Coefficients of Response surface for wave-frequency rms Stress σ_{rmsWF}

Location	c1	c2	c3	σ [ksi]	σ_{ln}
1	0.0254	9.69E-5	-0.37	0.17	0
4	0.0104	-1.86E-5	-0.674	0.04	0
4L	0.00628	0	-0.682	0.08	0
5	0.0414	1.06E-4	0	0	0.09

Response Surfaces for Wave-frequency T_Z and Bandwidth. Complicated models for these quantities lead to somewhat lower scatter, but are not warranted given the secondary importance of T_Z and bandwidth ε. The model for T_Z is of the form:

$$T_Z=c_1T_P \tag{2-34}$$

where T_p is the wave peak period. Table 2-8 shows the calculated coefficients and the standard deviation σ. Figure 2-13 compares the values predicted by the response surface to the values calculated by TIARA.

Table 2-8 Coefficients of Response Surface for Wave-frequency Tz

Location	c1	σ [sec]
1	0.85	0.57
4	0.93	0.17
5	0.75	0.92

The expression for bandwidth ε is simply a constant value, i.e.,

$$\epsilon = c_1 \tag{2-35}$$

Table 2-9 shows the calculated coefficients and the standard deviation σ. Figure 2-14 compares the values predicted by the response surface to the values calculated by TIARA.

Table 2-9 Coefficients of Response Surface for Bandwidth Parameter ϵ

Location	c1	σ
1	0.54	0.03
4	0.50	0.02
5	0.50	0.02

The bandwidth parameter that we will need in the reliability calculations is Vanmarcke's parameter δ, which is different from the bandwidth parameter ϵ calculated by TIARA. To this effect, values of ε are converted to δ by means of the approximation (describe how expression was derived)

$$\delta = 0.064 + 0.19\epsilon + 0.57\epsilon^2 \tag{2-36}$$

and the σ values in the table above are raised to 0.09 to account for uncertainty in the conversion.

Ratio of Bending to Total Stress. Most limit-state functions for tubulars distinguish between longitudinal stresses due to bending and longitudinal stresses due to axial force. In principle, one could construct separate response surfaces for bending and axial stresses for each of the four stress components considered above. This would double the number of stress response surfaces from four to eight, which is not practical. Instead, this study uses approximate values for the bending/total stress ratio at each location, and considers the uncertainty in this ratio as another epistemic uncertainty. We calculated values of the bending/total stress ratio for σ_{ml} (Figure 2-15) from the TIARA runs and use these values to estimate the range of the bending/total ratio for the peak combined stress (mean stress + peak time-variant stress). Recognizing that this ratio may not be the same for σ_{ml} and for the peak combined stress, we increase the calculated epistemic standard deviations by 50%. Note that in Figure 2-15, the ratios for Location 1 are slightly greater than unity. This indicates that Location 1 is under slight compression, rather than in tension. The value of this compressive force is so low that we will not switch from a limit-state function for bending+tension+pressure to one for bending+compression +pressure in the reliability calculations.

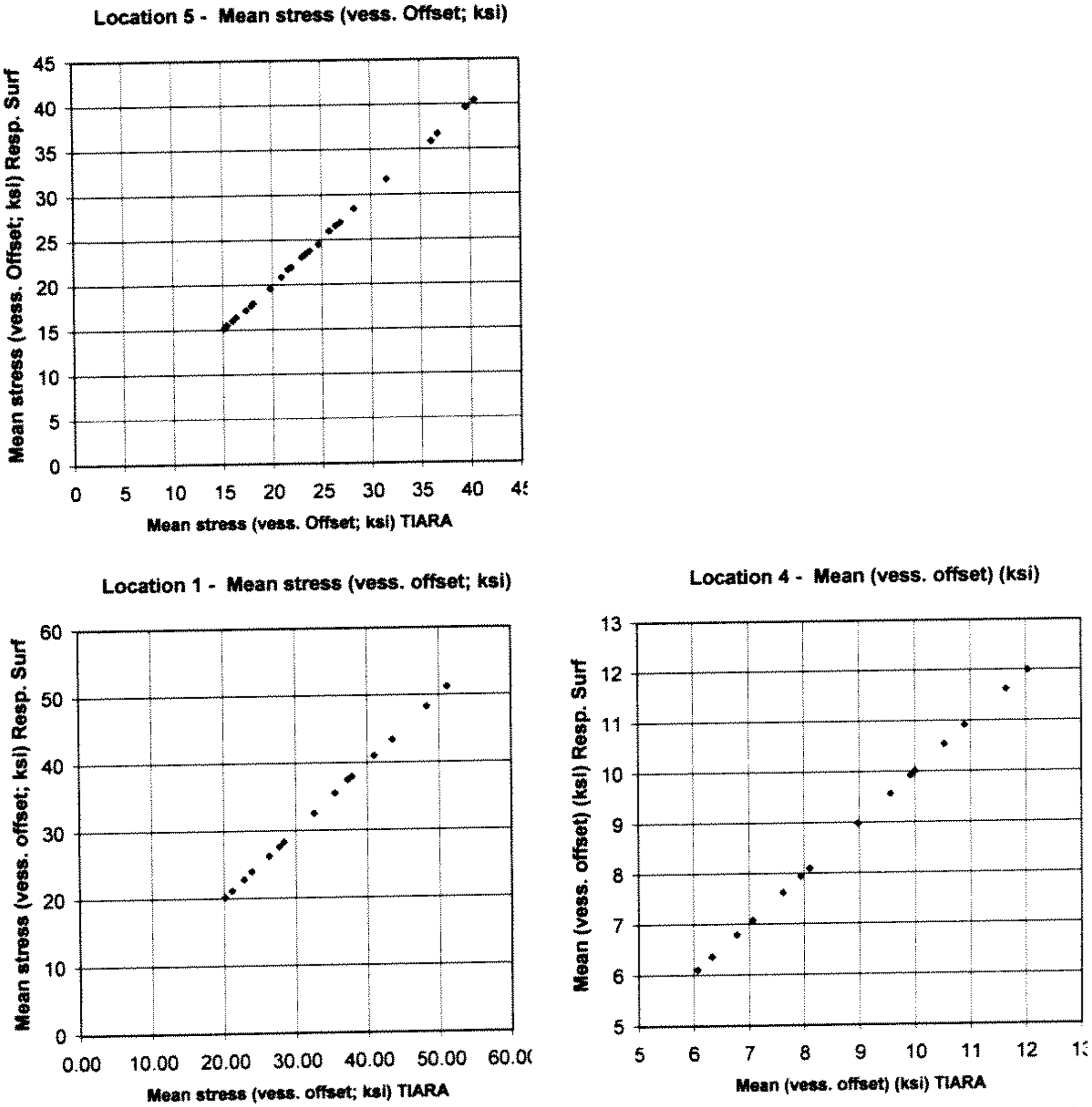

Location 5 - Mean stress (vess. Offset; ksi)

Location 1 - Mean stress (vess. offset; ksi)

Location 4 - Mean (vess. offset) (ksi)

Figure 2-9. Response surface vs. TIARA results: mean stress due to prestress and vessel offset.

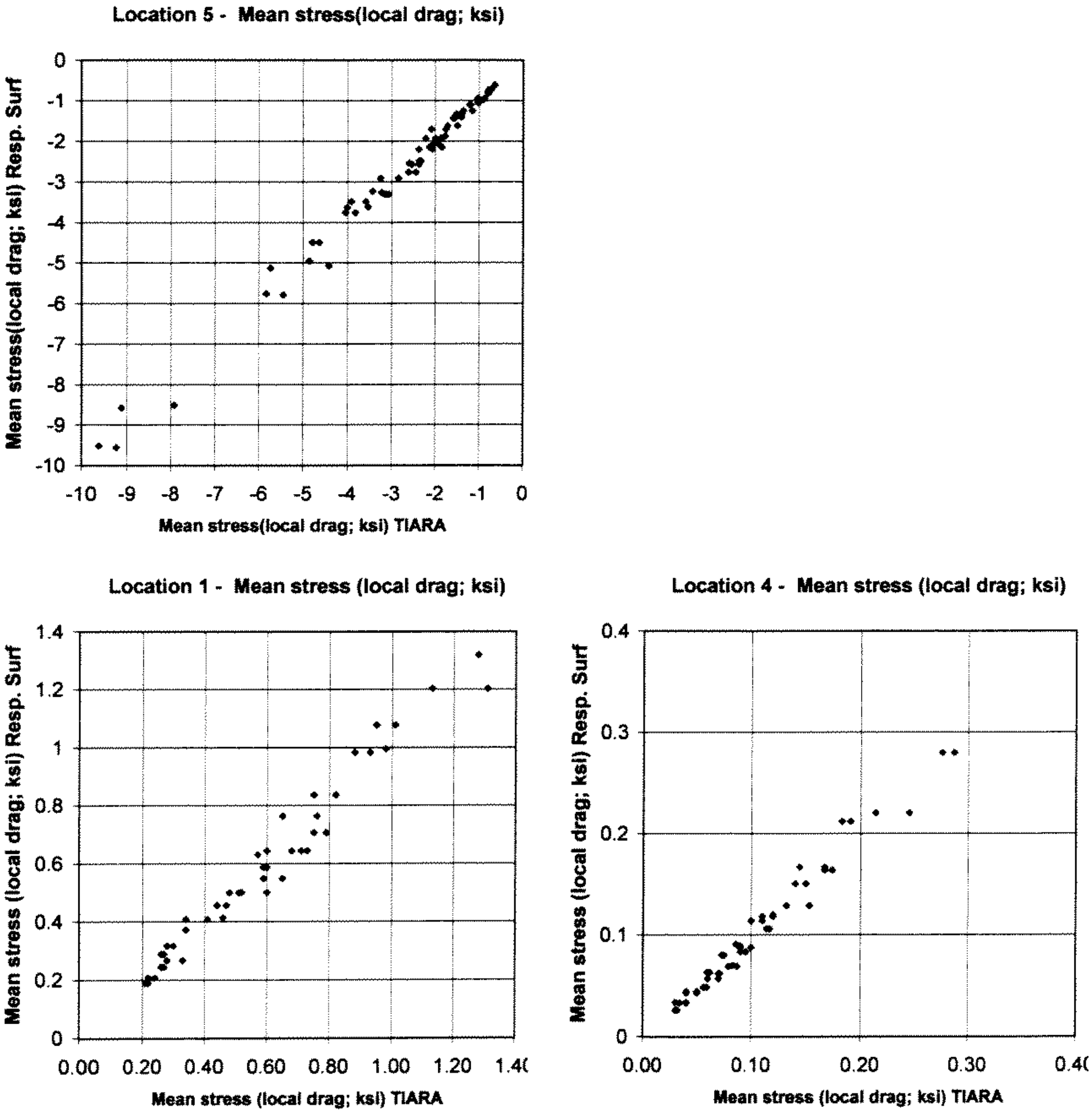

Figure 2-10. Response surface vs. TIARA results: mean stress due to local hydrostatic effects on riser.

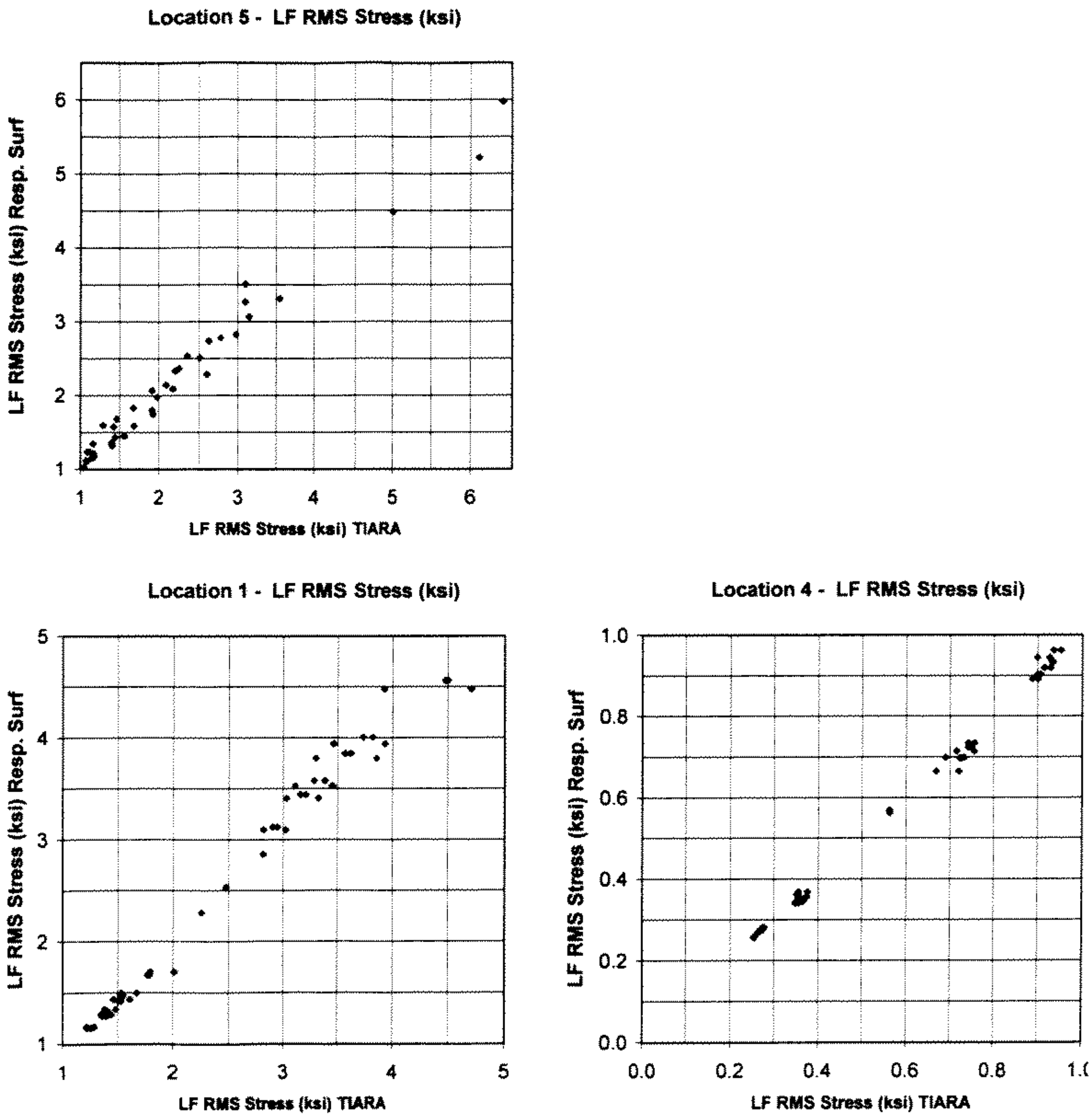

Location 5 - LF RMS Stress (ksi)

Location 1 - LF RMS Stress (ksi)

Location 4 - LF RMS Stress (ksi)

Figure 2-11. Response surface vs. TIARA results: low-frequency rms stress.

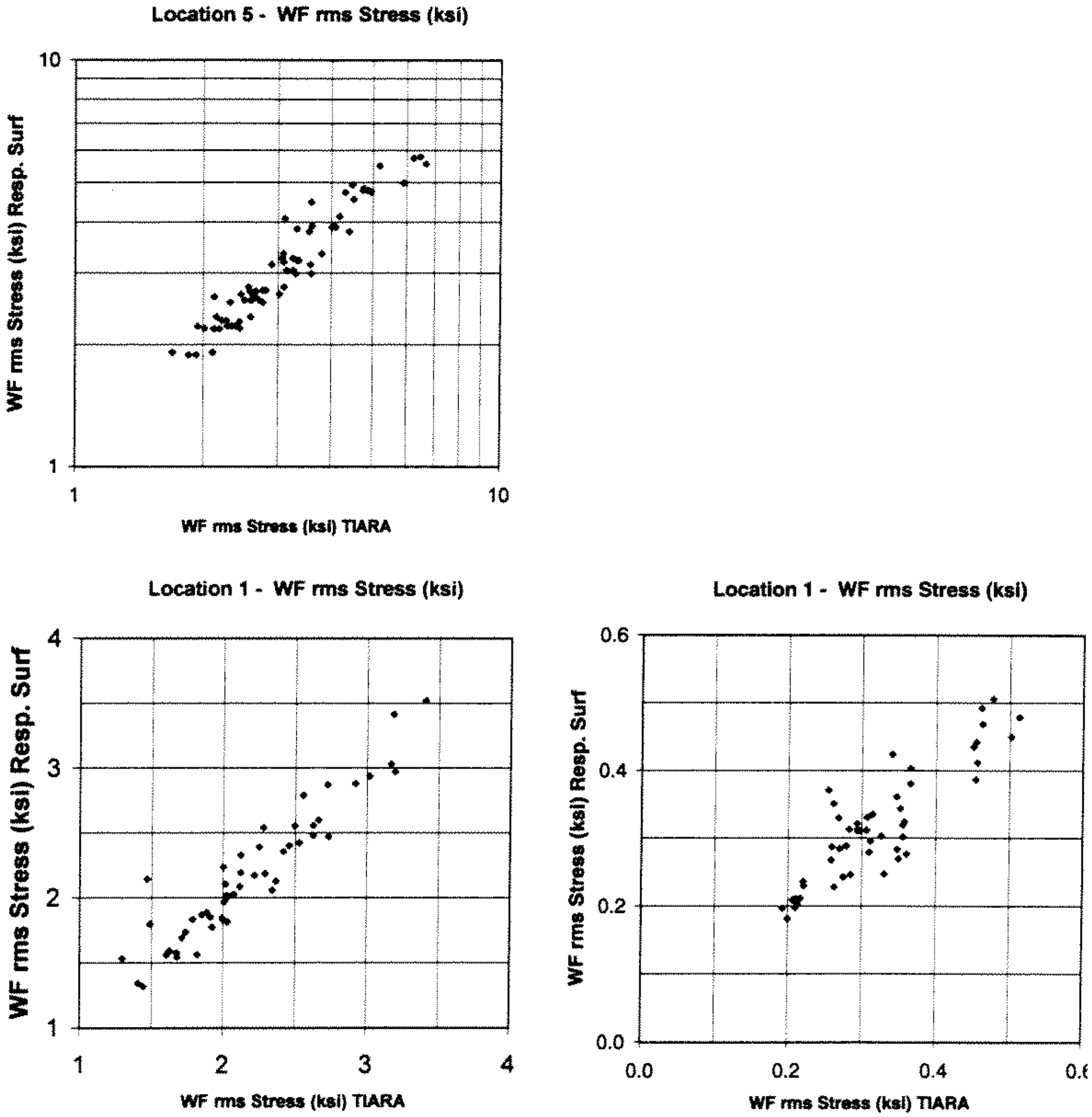

Figure 2-12. Response surface vs. TIARA results: wave-frequency rms stress.

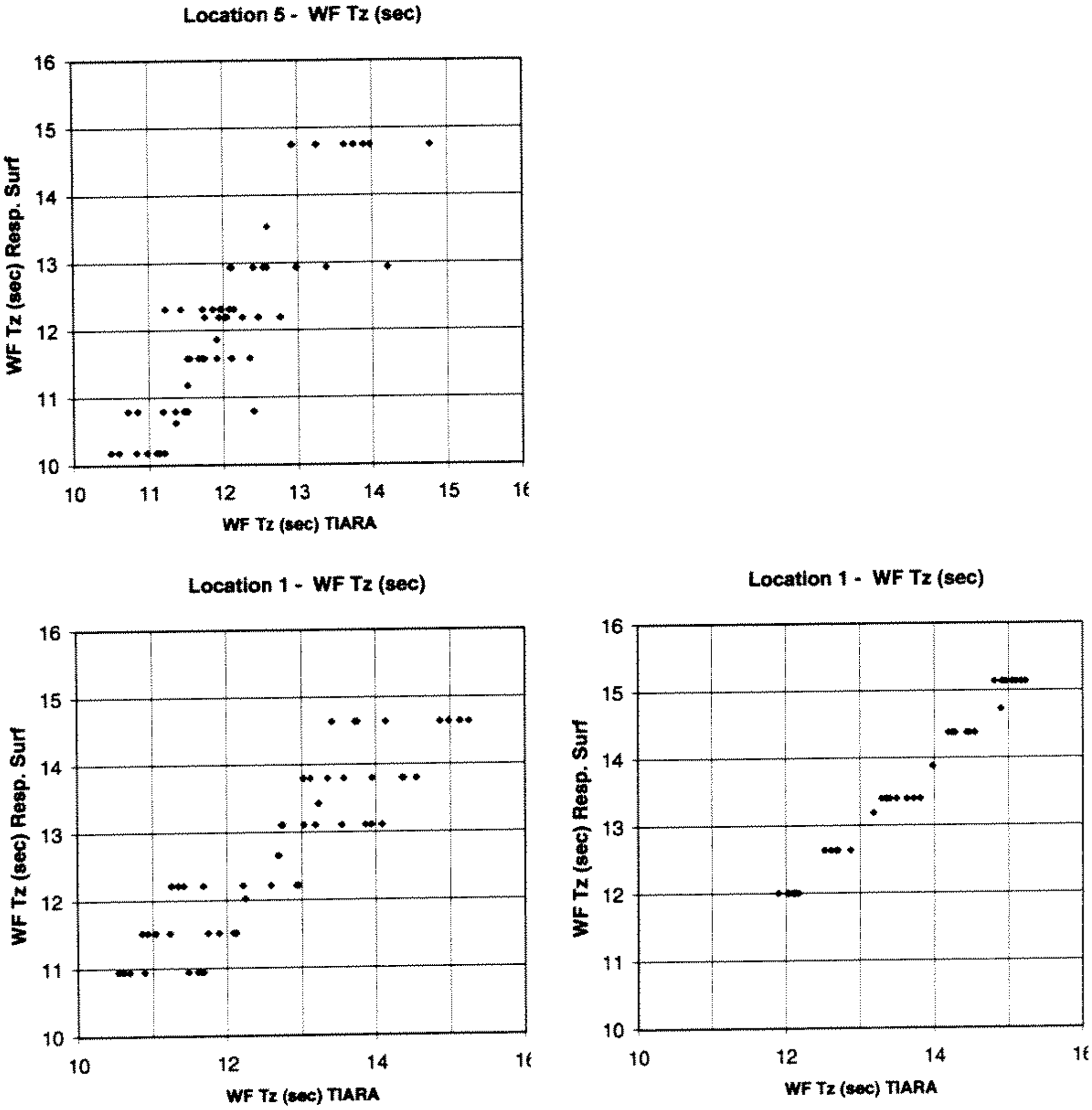

Figure 2-13. Response surface vs. TIARA results: Tz of wave-frequency stress.

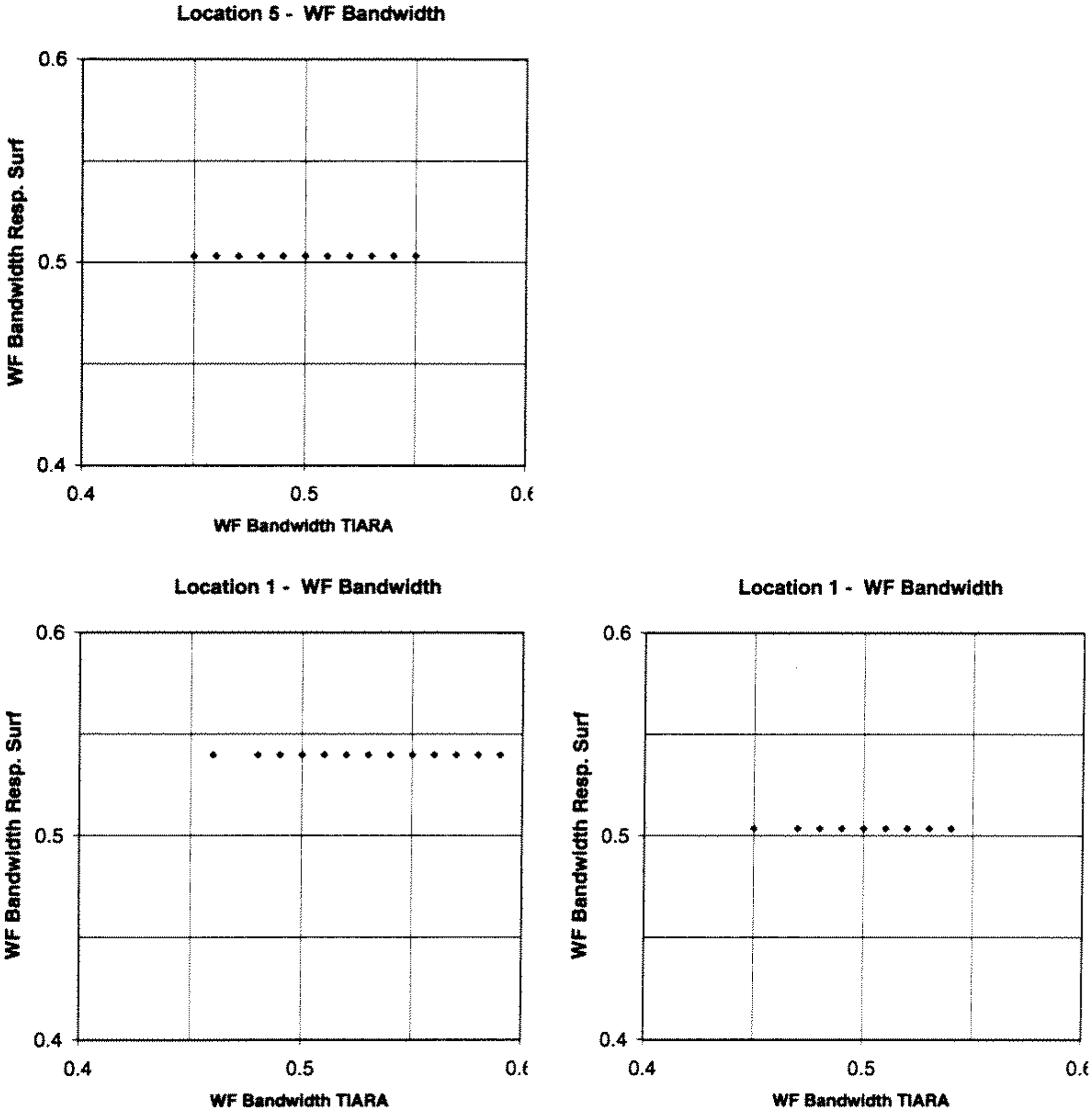

Figure 2-14. Response surface vs. TIARA results: bandwidth of wave-frequency rms stress.

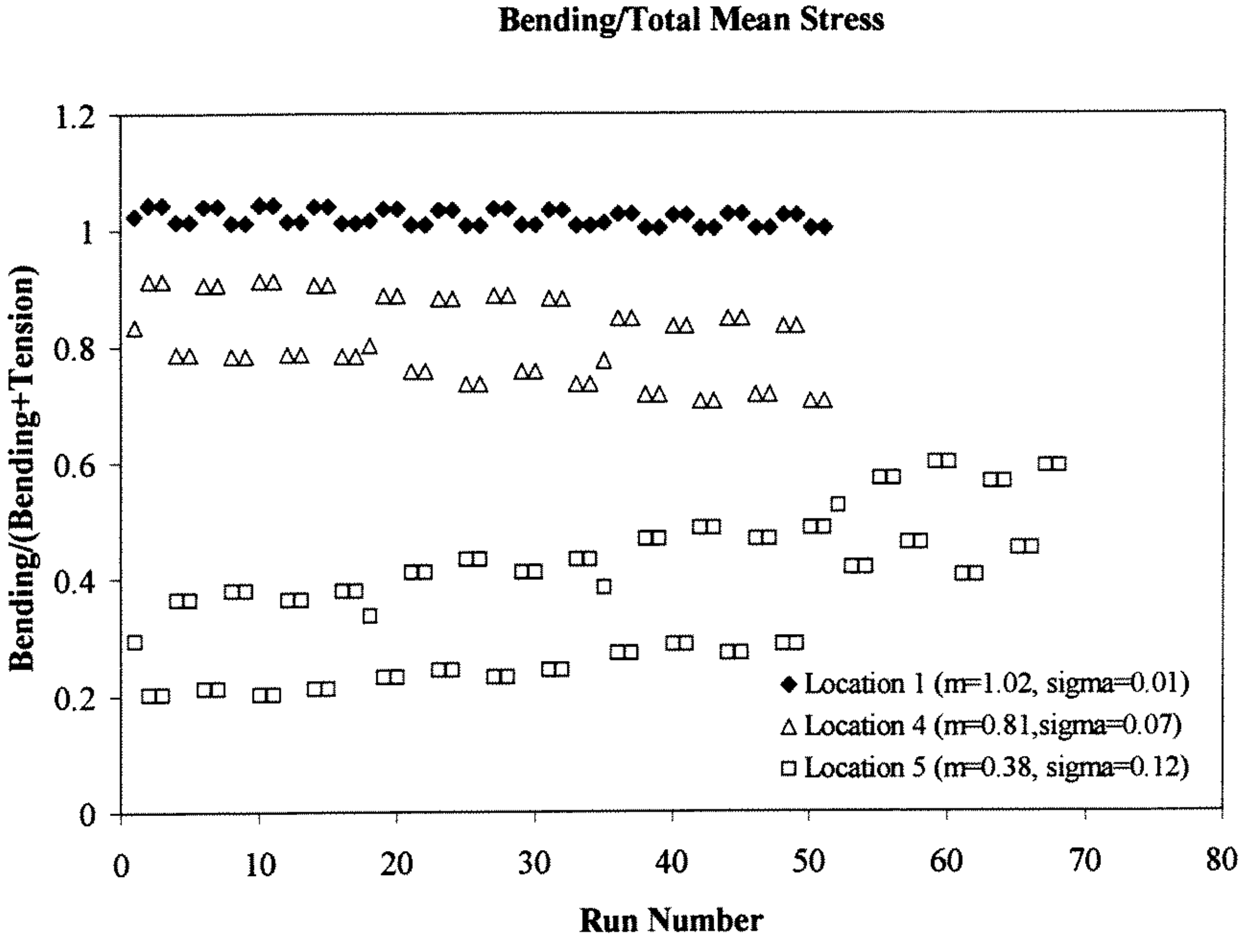

Figure 2-15. Calculated ratio of Bending/(Bending+Tension) stress for the mean stress from pretension and offset σ_{ml}. These values are used to estimate the corresponding ratio for the peak combined stress (the standard deviations will be increased by 50%). Ratios slightly greater than unity for Location 1 indicate slight compression.

2.5 LIMIT-STATE FUNCTIONS

The limit-state function specify whether a combination of stresses or forces (axial, bending, and hydrostatic) leads to failure of the riser or to some other undesirable state. Because failure-test data show significant scatter, limit-state functions also have a stochastic (or Type-I) component. There is also Type-II uncertainty associated with possible systematic tendencies to predict or under-predict failure for a given combination of stresses and riser dimensions.

This study has focused on limit-state functions for failure. There is also a need for limit-state functions associated with serviceability conditions. For instance, one may wish to calculate the probability of permanent deformations that will that will impede the introduction of tools through the riser, even though they will not lead to failure. We were not able to obtain serviceability limit-state functions from the literature or from inquiries with colleagues.

2.5.1 Limit-State Functions for Failure

Limit-state functions for the failure of tubulars should take into account the reserve tensile strength beyond yield, the reserve bending capacity beyond that associated with the elastic section modulus, as well as the effect of hydrostatic pressure.

This study considered and evaluated three limit-state functions from the recent literature; namely the published limit-state functions by Moan et al. (1994) and Mork et al. (1997), and the limit-state functions in the proposed ISO 13819-2. These limit-state functions use different mechanical formulations and their bias and uncertainties are evaluated by their respective authors using different data sets.

These three limit-state functions represent force checks. It was suggested at some of the project meetings that the conditions at the bottom of a top-tensioned riser are displacement controlled (i.e., formation of a plastic hinge does not necessarily lead to failure of the riser) and that one should use more generous displacement-based limit state functions (such as the one provided in Equations 27 and 28 of Mork et al., 1997). In spite of the merits of these arguments, this study will consider the more conventional force-based limit-state functions.

Moan et al. Limit-State Function. According to his limit-state function, failure occurs when the quantity

$$\left[\frac{f_t}{F_t}+\frac{f_b}{F_b}\right]^n+\frac{f_h}{F_h} \tag{2-37}$$

becomes equal or greater than unity. In the above equation (and in equations to follow), f indicates applied stress, F indicates capacity. The subscripts t, b, and h indicates tensile, bending, and hydrostatic stresses. The exponent n is itself a function of the tensile and bending utilization ratios; i.e.,

$$n=n\left(\frac{f_t}{F_t},\frac{f_b}{F_b}\right) \tag{2-38}$$

and may reach values of 10 or larger. The tensile capacity F_t is equal to the yield strength, the bending capacity F_b is predicted using an empirical formula in terms of the yield strength and the D/t ratio, and the hydrostatic capacity F_h is predicted using the Timoshenko formula[3]. The bias and uncertainty in this limit-state function are expressed in terms of the tensile, bending, and hydrostatic capacities rather than in terms of the utilization fraction as a whole. The biases are 1.2, 1.0, and 0.96, respectively. The COVs are 0.08, 0.07, and 0.14, respectively. These values were obtained using 245 test results and probabilistic arguments. The D/t ratio for Location 1 is slightly outside the range considered in the Moan et al. Study.

ISO 13819-2 Limit-State Function. This limit-state function was obtained from the ISO 13819-2 Draft C, setting all the capacity factors to unity. According to this limit-state function, failure occurs when the quantity

$$\frac{f_t}{F_{th}}+\frac{f_b}{F_{bh}} \tag{2-39}$$

becomes equal to unity. The quantities F_{th} and F_{bh} are the tensile and bending capacities, reduced for the effect of hydrostatic pressure. They are given by the expressions

$$F_{th}=F_y\left(\sqrt{1+0.09B^2-B^{2\eta}}-0.3B\right) \tag{2-40}$$

$$F_{bh}=F_b\left(\sqrt{1+0.09B^2-B^{2\eta}}-0.3B\right) \tag{2-42}$$

$$B=\frac{f_h}{F_h}; \qquad \eta=5-4\frac{F_h}{F_y} \tag{2-41}$$

where f_h and F_h are the hydrostatic stress and hydrostatic capacity, respectively. The characteristic bending strength F_b depends on the yield strength, the elastic section modulus, the plastic section modulus, and the D/t ratio.

The bias (1.075) and uncertainty (0.098) associated with this limit-state function were determined by Moses on the basis of comparisons to test data (draft ISO report provided by B. Stahl, Dec. 7, 1998).

---

[3] The three limit-state formulations considered here use different expressions to calculate hydrostatic capacity. In general, these expressions consider the Diameter/thickness (or D/t) ratio and the ovality of the pipe.

Mork et al. Limit-State Function. According to his limit-state function, failure occurs when the quantity

$$\left[\frac{f_b}{F_b}\right]^2 + \left[\frac{f_h}{F_h}\right]^2 \qquad (2\text{-}43)$$

becomes equal or greater than unity. The bending moment capacity F_b contains a reduction for the effect of axial force of the form

$$F_b = M_p \cos\left(\frac{\pi}{2}\frac{f_t}{F_t}\right) \qquad (2\text{-}44)$$

where M_p is the plastic moment capacity. The hydrostatic capacity is computed using the BSI (1993) formula. The bias (1.0) and uncertainty (0.13-0.17 [4]) associated with this limit-state function were determined using date from 148 tests.

Comparison of Limit-State Functions. Figures 2-16 and 2-17 compare the three limit-state functions summarized above for Locations 1 and 4. Location 1 (bottom of stress joint) is the location with the highest combined stresses. Location 4 is the location with the highest hydrostatic (hoop) stresses, as a result of its thinner wall. At both locations, the differences among the three models, as measured (for example) by the standard deviation of the radial distance for a given bending/tension ratio, is smaller than the nearly 10% coefficient of variation associated with each individual model. Thus, it is not necessary to consider multiple alternative limit-state functions in the reliability calculations. This study will use the ISO limit-state function, which falls between the other two for the bending dominated cases of interest here.

---

[4] Note that this uncertainty translates into an uncertainty of 0.7 to 0.9 in units of normalized stress (because the limit-state function is expressed in terms of stresses squared).

Limit State Function - Location 1

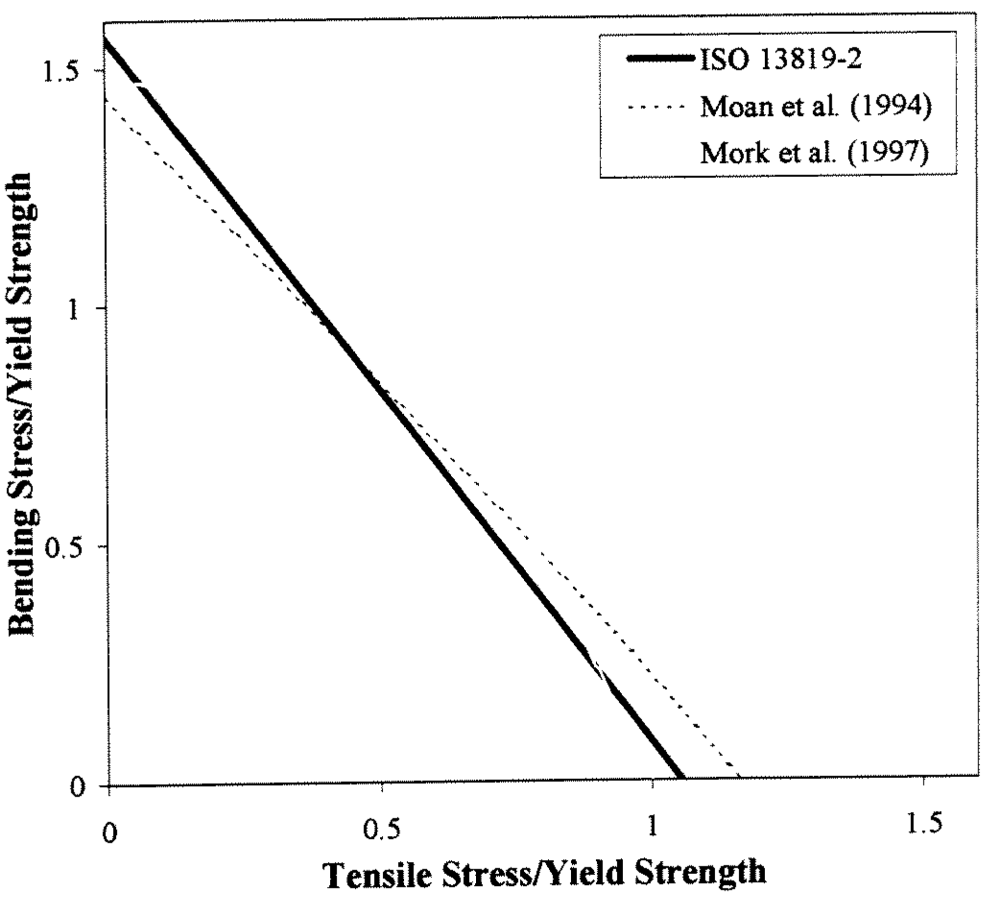

Figure 2-16. Limit-state functions shown as interaction equation between bending and tensile stresses at location 1. Outside diameter, 14.36 in; thickness, 2.3 in.

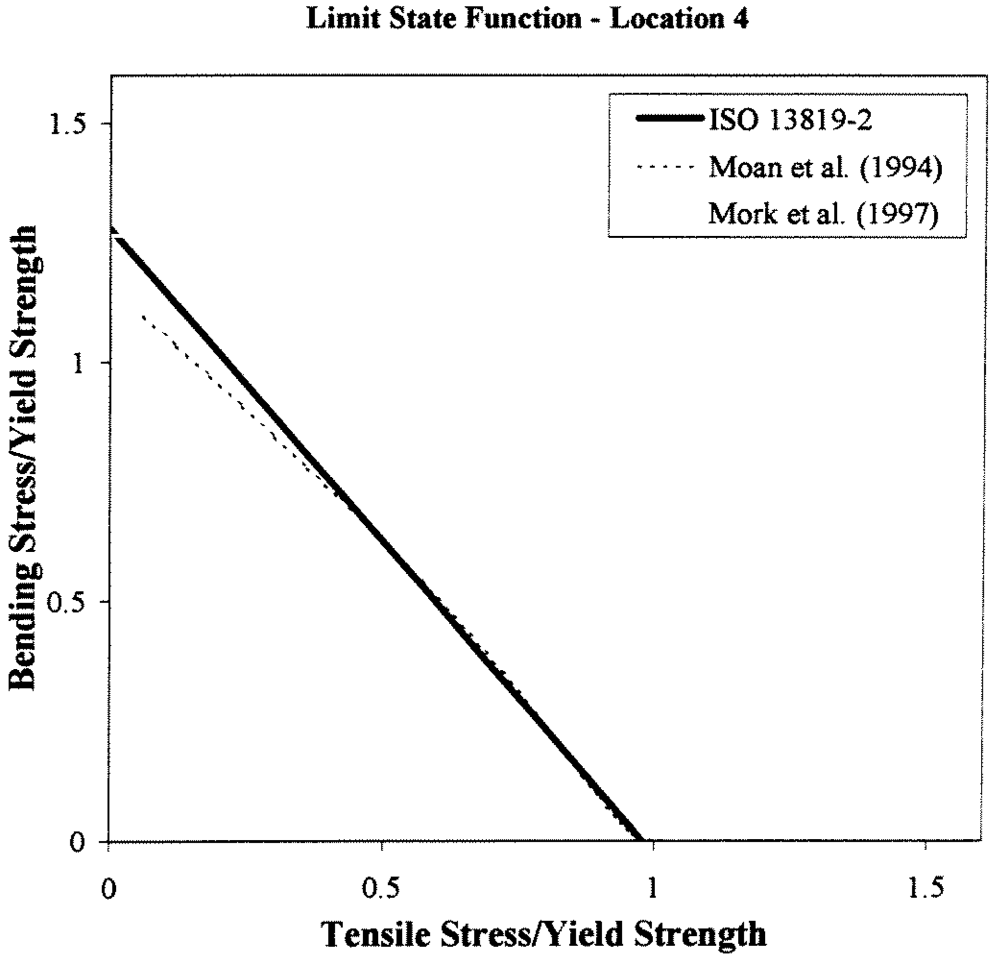

Figure 2-17. Limit-state functions shown as interaction equation between bending and tensile stresses at location 4. Outside diameter, 10.75 in; thickness, 0.5 in.

2.6 FORMULATION OF RELIABILITY MODEL

2.6.1 Background on Reliability Analysis and FORM/SORM Methods

FORM/SORM Methods. In the FORM/SORM reliability formulation used in this study, the state (safe or failed) of the riser location under consideration depends on the values of several random variables $X=[X_1,X_2,\ldots X_N]$ that represent met-ocean quantities, material properties, and other uncertain physical parameters. The limit-state function $g(X)$ indicates which values of X (i.e., which combinations of the random quantities) correspond to failure ($g<0$). Figure 2-18 contains a schematic representation of these quantities, for a problem with two random variables, such as a fixed structure of known capacity exposed to wind and waves. The same approach may be used to compute the probability that the total load will exceed some value of interest.

To calculate the probability of failure of the component (i.e., $P[g(X)<0]$), the FORM/SORM methodology (as implemented in the RELACS program; Risk Engineering, 1996) transforms the problem from the physical space (or X space) into standard normal space (or U space), where $U_1,U_2,\ldots U_N$ are independent standard normal random variables. A search algorithm then finds the most-likely failure point

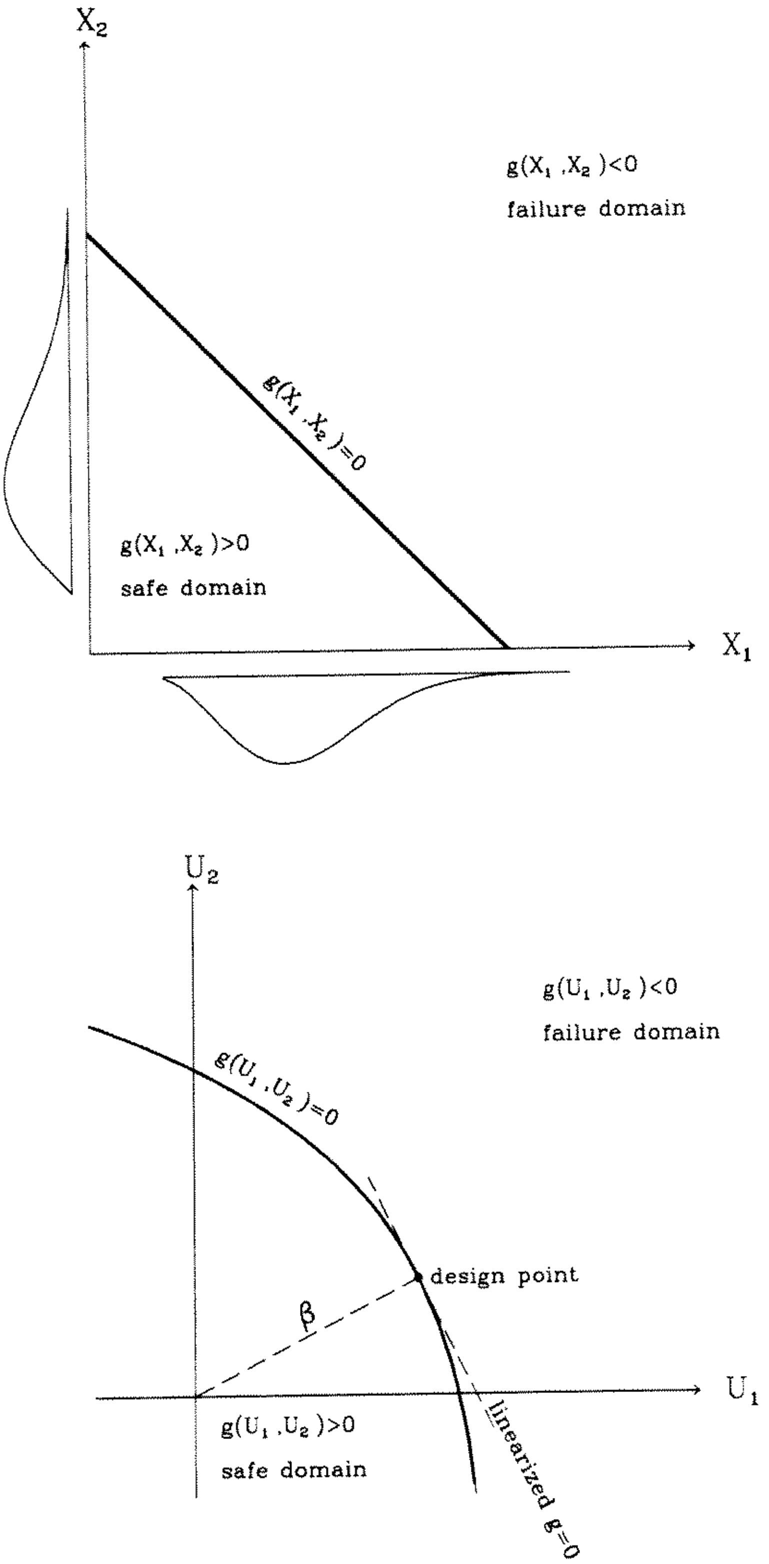

Figure 2-18. Schematic representation of a reliability problem and of FORM/SORM method. Top: formulation in physical (X) space. Bottom: formulation in normal (U) space.

(sometimes called the design point or β point). Because the probability-density contours are concentric and because the density drops rapidly as a function of distance from the origin, most of the failure probability is concentrated near the β point. The FORM/SORM methodology calculates an approximation to the failure probability by replacing the original $g(\boldsymbol{X})$ function with a simple approximation (e.g., linear or quadratic) to the g-function near the design point (see Figure 2-).

The failure probability P_f is sometimes expressed in terms of the safety index β, which measures the distance from the origin (in ***U*** space) to the design point. The relationship between P_f and β is expressed mathematically as $P_f = \Phi(-\beta)$, where Φ is the standard normal cumulative distribution function (CDF). The coordinates of the design point (converted from ***U*** space to physical or ***X*** space) indicate the combination of values of the physical variables that is most likely to lead to failure. This information is useful in the development of combined environmental criteria.

Another useful quantity is α, the normalized gradient vector of $g(\boldsymbol{U})$ at the design point (or, equivalently, the vector of direction cosines of the design point (with reversed sign). The squared values of entries in α (or importance factors) indicate the contributions of the various random variables to the probability of failure.

Types of Uncertainty. It is customary in reliability studies to distinguish between two types of uncertainty, as follows:

> Aleatory or Type-I Uncertainty. Uncertainty that is inherent to the unpredictable nature of future events. For example, aleatory uncertainty includes processes related to hurricane spawning, track, intensity, and dynamic structural response that cannot be quantified before the hurricane occurs. Aleatory uncertainty cannot be reduced by collection of additional information. One may be able, however, to obtain better estimates of the aleatory uncertainty by considering additional data.
>
> Epistemic of Type-II Uncertainty. Uncertainty that is due to incomplete knowledge and data about the physics of the hurricane and dynamic-response process, which translate into uncertainty in the parameters and functional forms of the models that we use for the aleatory uncertainty. In principle, epistemic uncertainty can be reduced by the collection of additional information.

Although this distinction is not absolute, it is useful for several reasons. In particular, it is useful to know how much the calculated failure probability may change as a result of additional data collection or detailed modeling efforts that are expected to reduce the epistemic uncertainty. Moreover, the importance factors associated with the epistemic quantities pinpoint which uncertainties contribute the most to epistemic uncertainty in the failure probability.

Nested FORM/SORM Formulation. This study utilized two nested FORM/SORM analyses for the calculation of the probability of failure. Although this nested approach turned out not to be absolutely necessary in this study, it is a useful device for presenting the aleatory and epistemic uncertainties separately.

The inner FORM/SORM module calculates the failure probability (or the probability that the peak stress will exceed a certain value of interest) during one severe storm by integrating over the aleatory uncertainties (e.g., storm characteristics, differences between the true values of the stresses and the values predicted by the response surfaces, and short-term details of the dynamic response), for fixed values of the quantities with epistemic uncertainty. The limit-state function for the inner FORM/SORM module takes the form

$$g(\boldsymbol{X}) = B - \left[\frac{f_t(\boldsymbol{X})}{F_{th}} + \frac{f_b(\boldsymbol{X})}{F_{bh}} \right] \tag{2-45}$$

where B is the uncertain (type-II) bias in the ISO-13819-2 limit-state function. The bending and tensile stresses f_t and f_b depend on the physical random (type-I) quantities $\boldsymbol{X}$. If the limit-state function had no bias and no uncertainty, B would be exactly 1.

The failure probability during one storm, given the values of the quantities with epistemic uncertainty (which are represented by the vector $\boldsymbol{Z}$), is converted into an annual failure probability by means of the expression:

$$P_{f,\ 1\ \mathrm{year}}(\boldsymbol{Z}) = 1 - \exp\left(-\nu\, P_{f,\ 1\ \mathrm{storm}}(\boldsymbol{Z})\right) \tag{2-46}$$

where ν is the annual rate of severe storms (see Eq. 2-2)[5].

The outer FORM/SORM module integrates over the epistemic uncertainties and computes the expected value of $P_{f,\ 1\ \mathrm{year}}(\boldsymbol{Z})$ over all the epistemic uncertainties in $\boldsymbol{Z}$. This expectation calculations is transformed into a FORM/SORM problem by using the approach of Wen and Chen (1987), in which limit-state function is of the form:

$$g_{\mathrm{outer}}(\boldsymbol{Z}) = Z_{\mathrm{aux}} - \Phi^{-1}\left(P_{f,\ 1\ \mathrm{year}}(\boldsymbol{Z})\right) \tag{2-47}$$

where Z_{aux} is an additional random quantity in the outer FORM/SORM loop and has a standard normal distribution. Z_{aux} represents the effect of all aleatory uncertainties in the problem (i.e., the Poisson occurrences of rare storms and the probability failure during one storm).

2.6.2 Peak Values of Short-Term Time-Variant Response

The peak dynamic stress during the duration of the storm (1.5 hours)--given the rms stress and the frequency content--is a random (more precisely, aleatory or type I) quantity. Except for a few special cases, closed-form solutions to this problem are approximate. These approximate solutions characterize the frequency content by means of a bandwidth parameter, which may be defined in several ways (e.g., Cartwright and Longett-Higgins, Ochi, Vanmarcke). In deterministic applications, and in some probabilistic ones, the ratio of peak to rms stress, sometimes referred to as the "peak factor" or "Ochi factor," is treated as deterministic. Alternatively, one may include the peak factor as another aleatory uncertainty (as will be done here), although its coefficient of variation is not too large.

---

[5] The above equation assumes that the arrivals of rare storms constitute a Poisson process. Because ν is small, the expression can be linearized and simplified into $P_{f,\ 1\ \mathrm{year}}(\boldsymbol{Z}) \approx \nu\, P_{f,\ 1\ \mathrm{event}}(\boldsymbol{Z})$. Also because ν is small, this linearized expression is a good approximation to the annual failure probability, even if the arrivals of severe storms are not Poisson.

A single bandwidth parameter is not a good spectral representation for stresses in TLPs because the dynamic stress consists of two well-separated narrow-band responses; namely, the slow-drift response (with a period equal to the fundamental surge period of the TLP, more than 100 seconds) and the wave-frequency response (with periods of 10 to 20 seconds). The bandwidth parameter for this bimodal spectrum is large, suggesting a wide-banded response and leading to ever-estimation of the peak factor.

The formulation by Toro (1984; see also Toro and Cornell; 1986) considers the bimodal character of the response and yields a more accurate calculation of peak factors, as validated by Monte Carlo simulations. In this formulation, the peak factor Y_T over a duration T has a cumulative distribution of the form

$$F_{Y_T}(y)=A(y)\exp(-\alpha(y)T) \tag{2-48}$$

where y is the peak-factor value of interest, $A(y)$ is the probability that the response is lower than y at the beginning of the time period ($A(y)$ may be taken as unity), and[6]

$$\alpha(y)=\nu_Y(y)\frac{\left\{1-e^{-\sqrt{2\pi}\,\delta_a(y-1/y)}\right\}\left\{1-e^{-\sqrt{2\pi}\,\delta_b y}\right\}}{A(y)\left[1-e^{-\sqrt{2\pi}\,\delta_a(y-1/y)}\left\{1-\frac{1}{\sqrt{2\pi}\,\delta_b y}\left(1-e^{-\sqrt{2\pi}\,\delta_b y}\right)\right\}\right]} \tag{2-49}$$

where $\nu_Y(y)=\exp(-y^2/2)/T_Z$ is the gaussian up-crossing rate and δ_a and δ_b are parameters that depend on the bandwidth, separation, and relative rms's of the long and short-period responses (see Eqs. 1-51 and 1-53b in Toro, 1984). The ratio term in Equation 2-49 is smaller than unity and represents Toro's correction for the effect of bimodality.

2.6.3 Summary of Epistemic and Aleatory Variables used in Calculations

Table 2-10 lists the random variables in the outer FORM/SORM formulation, nearly all of which represent epistemic uncertainties. The values of the biases and COVs were generally chosen on the basis on consensus among meeting participants. The values associated with global-response quantities are the same values used in the TLP Global-Response Calibration study (see Banon et al., 1994). Table 2-11 lists the random variables in the inner FORM/SORM formulation. These quantities represent the met-ocean variables and response characteristics during one storm. Among the response characteristics, we include the error introduced by our use of response surfaces to calculate stresses, zero-crossing frequencies, and bandwidth. Because Equation 2-48 is difficult to solve for the peak factor y, we use the Wen-Chen approach to represent uncertainty in the peak factor.

---

[6] The equation shown here applies to the single-barrier problem, where only crossings in one direction are counted. The equation in Toro (1984) applies to the double-barrier problem.

Table 2-10 RANDOM VARIABLES IN OUTER FORM/SORM FORMULATION

Var. No.	Description	Bias	COV
1	Uncertainty in shape term (slope) of Vw distribution (see Eq. 2-2)	1	0.1
2	Uncertainty in assumed Vcurr|Hs distribution (see Eq. 2-5)	1	0.1
3	Uncertainty in Cd in wave zone (<500'; mean 1.2)	1	0.3
4	Uncertainty in Cd at depth (>500'; mean=0.7)	1	0.3
5	Uncertainty in calculated mean force on vessel	1	0.2
6	Uncertainty in calculated slow-drift rms vessel offset	0.95	0.3
7	Uncertainty in calculated vessel RAO (introduced as a multiplier on the RAO and applies equally to all frequencies)	1	0.05
8	Uncertainty in riser-stress calculations (does not apply to the mean stress from pretension and mean offset, σ_{m1})**	1	0.1 (bottom) 0.2 (surface)
9*	Uncertainty in Limit-State Function	1.08	0.10
10*	Uncertainty in Yield Strength (nom. 80 ksi)	1.1	0.03
11*	Uncertainty in Bending/Total Axial stress (mean 0.7-0.9)	1	0.05-0.10
12	Z_{aux} (Wen-Chen trick) Represents all aleatory uncertainties (including occurrence [passing] of severe storms near site)	mean=0	σ=1

* Only in P[failure] calculations

** At Location 5, we consider additional epistemic uncertainty as a result of extrapolation of the mean stress from hydrodynamic forces acting directly on the risers (σ_{m2}). If the value of σ_{m2} calculated by the response surface is smaller than -10 ksi (i.e., greater than 10 ksi in absolute value), it has a standard deviation of $[-\sigma_{m2}-(-10\text{ ksi})]/2$.

Table 2-11 RANDOM VARIABLES IN INNER FORM/SORM FORMULATION

Var. No.	Description	Reference
1	Wind speed Vwind (fps)	Eq. 2-2
2	Hs|Vwind (ft)	Eq. 2-3
3	Tp|Hs (sec)	Eq. 2-4
4	Curr|Hs (fps)	Eq. 2-5
5	Error in Response Surface (mean stress from vessel offset, σ_{m1})	Table 2-4
6	Error in Response Surface (mean stress from local drag forces on riser, σ_{m2})	Table 2-5
7	Error in Response Surface (rms stress LF)	Table 2-6
8	Error in Response Surface (rms stress WF)	Table 2-7
9	Error in Response Surface (Tz WF)	Table 2-8
10	Error in Response Surface (bw WF)	Table 2-9
11	U_{aux} (Use Wen-Chen trick to represent aleatory uncertainty in the peak factor)	Eqs. 2-47 and 2-48

2.7 RESULTS

2.7.1 Failure Probabilities and Associated Design Points

Table 2-12 shows the failure probabilities from extreme hurricane loads at locations 1, 4, and 5. The failure probability is low at location 1 and very low at locations 4 and 5. For the sake of comparison, the Norwegian Draft Design Standard specifies annual probabilities of failure of 1E-3 to 1E-5 (depending on safety class) for ultimate limit states.

Table 2-12 FAILURE PROBABILITIES FOR THREE LOCATIONS IN RISER

Location (elev., ft)	Description	Annual Failure Probability	Safety Index (β)
5 (3293)	Bottom of tensioner joint	2.8E-7	5.0
4 (84)	Top of transition joint	~0	-
1 (10)	Bottom of stress-joint taper	1.2E-5	4.2

Table 2-13 shows the design points for the inner loop. The importance factors (α^2) indicate the relative contributions of the various random quantities to the calculated failure probability. The most important storm characteristics are wind speed and current. Other environmental quantities are take values near their conditional medians (given wind speed or Hs)[7]. The terms associated with the response surfaces (which represent differences between the true stresses and those predicted by the response surface, given the global response and the seastate) also have very low importance factors. This indicates that no price is paid by using the response surfaces as a surrogate for the riser-response calculations. Similarly, the auxiliary variable used to control the peak factor has a low importance factor.

A low importance factor does not mean a low sensitivity to the parameter in question, in a deterministic sense. It simply means that the randomness in that parameter has a small effect in the results and that the parameter could have been treated as deterministic.

Table 2-14 shows the values of other important physical quantities at the design point. The first eight quantities relate to the vessel motions. The remaining quantities relate to riser stresses and their associated dynamics. The mean stress (due mostly to static offset) represents 75% of the

---

[7] It is worth noting that, when quantities are correlated, the probabilistic importance factors depend on which variable is defined as primary (the one that appears first in the list of random variables). If we had used Hs as the primary variable, it would appear as much more important than it appears here.

Table 2-13. INNER-LOOP DESIGN POINT FOR FAILURE CONDITION AT LOCATION 1

No.	Description	Value	U	α (direction cosine)		α^2
1	Windspeed (fps)	276.0	3.430	-0.990	▬	0.980
2	Hs (feet) | Vw	75.0	0.206	-0.059		0.004
3	Tp (sec) | Hs	20.5	-0.039	0.011		0.000
4	Vcurr (fps) | Hs	8.5	0.394	-0.114	▪	0.013
5	$\varepsilon_{resp.\ surf}$ (mean stress from prestress and mean offset)	0.3	0.005	-0.002		0.000
6	$\varepsilon_{resp.\ surf}$ (mean stress from hydro. forces on riser)	0	0.004	-0.001		0.000
7	$\varepsilon_{resp.\ surf}$ (LF rms stress)	0.042	0.042	-0.012		0.000
8	$\varepsilon_{resp.\ surf}$ (WF rms stress)	0.038	0.038	-0.011		0.000
9	$\varepsilon_{resp.\ surf}$ (Tz of WF stress)	-0.005	-0.005	0.001		0.000
10	$\varepsilon_{resp.\ surf}$ (bandwidth of WF stress)	-0.015	0.005	-0.001		0.000
11	Auxilliary Variable (controls peak factor)	0.170	0.190	-0.055		0.003

Table 2-14
Values of Interesting Physical Quantities at the Failure Design Point for Location 1

No.	Description	Value
1	Mean force (wind; kips)	3314.7
2	Mean force (waves; kips)	556.6
3	Mean force (current; kips)	1809.6
4	Mean vessel offset	523.7
5	XrmsLF(wind; ft)	24.0
6	XrmsLF(waves; ft)	2.35
7	XrmsLF(srss; ft)	24.1
8	Tz LF (sec)	73.2
9	bandwidthWF	0.54
10	mean stress (ksi)	90.7
11	rms stress (LF; ksi)	4.5
12	rms stress (WF; ksi)	7.0
13	Peak dynamic stress (ksi)	30.5
14	peak factor	3.69
15	bimodal effect	0.94

peak stress. The wave-frequency and low-frequency rms stresses are comparable in magnitude. The reduction in the peak factor as a result of considering bimodality is 6% of the peak dynamic response (or 1.8 kips).

Table 2-15 OUTER-LOOP DESIGN POINT FOR FAILURE AT LOCATION 1

No.	Description	Value	U	α (direction cosine)		α^2	COV of Pf
1	Uncertainty in Vwind Distribution	1.07	0.758	-0.177	■	0.031	0.94
2	Uncertainty in Vcurr Distribution	1.03	0.317	-0.074	▪	0.005	0.34
3	Cd (wave zone)	1.20	0.155	-0.036		0.001	0.16
4	Cd (>500')	0.64	-0.168	0.039		0.002	0.18
5	Uncertainty in Mean force	1.11	0.605	-0.141	■	0.020	0.70
6	Uncertainty in Slow-Drift Offset	0.96	0.175	-0.041		0.002	0.19
7	Uncertainty in Vessel RAO	1.00	0.077	-0.018		0.000	0.08
8	Uncertainty in riser stresses	1.02	0.266	-0.062		0.004	0.28
9	Capacity Factor (max/yield)	1.00	-0.761	0.178	■	0.032	0.94
10	Yield Strength	87.4	-0.229	0.054		0.003	0.24
11	Bending Stress/Total Stress	0.882	-0.477	0.112	▪	0.012	0.53
12	Auxiliary Variable (Inner Loop)	-4.030	-4.030	0.942	▬▬▬	0.887	-
-	All Type II	-	-	0.335	▬	0.113	2.94

Table 2-15 shows the design-point for the outer-loop. For quantities such as the uncertainty in the wind-speed distribution, the "Value" column indicates the deviation between reality and the base-case model (expressed as a factor) at the failure design point. The most-important Type-II uncertainties are those in the wind-speed distribution, in the limit-state function (Capacity Factor), and in the calculation of mean force on the vessel (which controls mean vessel offset). The last column (labeled COV of Pf) indicates the uncertainty in the failure probability (expressed as a coefficient of variation) due to the respective Type-II uncertainty. Thus, the uncertainty in wind speed introduces a 94% COV in the failure probability (roughly a factor of 2 uncertainty). All Type-II uncertainties combined introduce a 294% COV (roughly an uncertainty of a factor of 4 or an uncertainty of one-half order of magnitude).

2.7.2 Values of Variables at the 100- and 1000-year Design Points

It is also interesting to note the values of the storm quantities at the design points associated with the 100-, 1,000, and 10,000-year stresses at locations 1, 4, and 5. These values are shown in Table 2-?, which shows that the values of storm quantities for a given return period differ somewhat for locations at the bottom (more sensitive to mean offset) and locations at the top (more sensitive to wave-frequency motions).

Table 2-17 shows the outer-loop design point for location 5 and 10,000-year return period. The values in this table show that for locations at the top of the riser, the most important contributors to uncertainty in the calculated failure probability are uncertainty in mean force on the vessel, uncertainty in the distribution of wind speed, and uncertainty in riser stress calculations. Uncertainty in the Cd in the wave zone is somewhat important. Note that the uncertainties in

Table 2-16 VALUES OF STORM PARAMETERS AND PEAK FACTOR FOR VARIOUS RETURN PERIODS

100-year Values

	Loc. 1	Loc. 4	Loc. 5
Tensile Stress (ksi)	47.1	11.6	28.0
Descr.			
Vwind(fps)	136	136	134
Hs(ft)	36.9	37	36.3
Tp(sec)	14.2	14.2	14.1
Vcurr(fps)	3.39	3.39	3.27
Peak Factor	3.633	3.505	3.82

1,000-year Values

	Loc. 1	Loc. 4	Loc. 5
Tensile Stress (ksi)	71.5	15.5	39.8
Descr.			
Vwind(fps)	186	187	181
Hs(ft)	50.7	50.7	49.2
Tp(sec)	16.5	16.5	16.2
Vcurr(fps)	5.12	5.11	47.9
Peak Factor	3.67	3.56	3.81

10,000-year Values

	Loc. 1	Loc. 4	Loc. 5
Tensile Stress (ksi)	98.0	19.1	65.7
Descr.			
Vwind(fps)	237	238	220
Hs(ft)	64.4	64.6	59.7
Tp(sec)	18.7	18.8	17.9
Vcurr(fps)	6.88	6.87	6.02
Peak Factor	3.69	3.592	3.82

yield strength and in the limit-state function are zero because these calculations consider peak stresses, not failure. If we were considering failure, these terms would appear.

Calculations were also performed using Hs as the primary variable in the metocean model. Results (not included here; see handouts from 12/15/98 meeting) indicate differences of 10% or less in the calculated stresses for 1,000 and 10,000 years.

Table 2-17 OUTER-LOOP DESIGN POINT FOR THE 10,000-YEAR PEAK STRESS AT LOCATION 5

No.	**Description**	**Value**	**U**	**α (direction cosine)**		**α^2**	**COV of Pf**
1	Uncertainty in Vwind Distribution	1.05	0.568	-0.152	▪	0.023	0.66
2	Uncertainty in Vcurr Distribution	0.99	-0.043	0.011		0.000	0.05
3	Cd (wave zone)	1.04	-0.339	0.091	▪	0.008	0.37
4	Cd (>500')	0.67	0.000	0.000		0.000	0.00
5	Uncertainty in Mean force	1.14	0.759	-0.203	▬	0.041	0.96
6	Uncertainty in Slow-Drift Offset	0.98	0.239	-0.064		0.004	0.26
7	Uncertainty in Vessel RAO	1.01	0.166	-0.044		0.002	0.18
8	Uncertainty in riser stresses	1.08	0.498	-0.133	▪	0.018	0.57
9	Capacity Factor (max/yield)	-	0.000	0.000		0.000	0.00
10	Yield Strength	-	0.000	0.000		0.000	0.00
11	Bending Stress/Total Stress	-	0.000	0.000		0.000	0.00
12	Auxiliary Variable (Inner Loop)	-3.550	-3.550	0.950	━━━━	0.903	-
-	All Type II	-	-	0.311	▬	0.097	1.90

2.8 SUMMARY AND CONCLUSIONS

The developments and results in this chapter demonstrate the process for the reliability analysis of a top tensioned riser and show that the process is feasible and practical. This process includes a joint probability model of environment, a model for the global response of the vessel, response surfaces to calculate riser stresses, and a realistic limit-state equation. All these elements are considered within a FORM/SORM reliability analysis, which considers Type I and II uncertainties.

The material developed in this study and presented here provides the road map for future applications, for both top-tensioned risers and other riser types.

The most delicate steps in the formulation is the development of response surface (design of experiments, TIARA runs, and fitting of response surfaces). Three important lessons in this regard are the following:

a. We should have expanded the experimental design (more values of Hs, particularly high ones; more parameter combinations for each Hs). The incremental cost of performing additional TIARA runs is small compared to the setup cost and to the cost of fitting the response surfaces. Results from these additional runs facilitate the fitting of the response surfaces and will make them more robust.

b. The decomposition of stresses is critical. We calculated two types of static stresses (from pretension and mean offset, from direct hydrodynamic forces on risers), and two types of dynamic stresses (low-frequency and wave frequency). We could have decomposed each of these into their tensile and bending components--for the sake of the limit state functions, which treat tensile and bending separately. Instead, we treated the ratio of bending to total stress as an uncertain quantity, and found that this uncertainty contributes modestly to the total uncertainty.

c. The most difficult response surfaces to fit, and those with the highest scatter, were those associated with wave-frequency stresses. One should explore other, more analytical, approaches for this response surface. For instance, one should explicitly consider the vessel RAO and the wave spectrum. This is more important for SCR risers than for top-tensioned risers, as the former are more sensitive to wave-frequency motions.

Use of response surfaces (instead of "calling" the riser-analysis software directly during the reliability calculations) does not introduce a significant penalty (extra scatter) in the results. The development of the response surfaces is, as discussed above, a delicate step that must be performed carefully.

The results obtained here from application of this methodology to the Marlin platform indicate that failure probabilities as a result of hurricane loads are low at the bottom and very low at the top. Most of the stress on the riser is due to mean offset. The most important environmental quantity is wind speed (this is in part a consequence of the way the metocean model was set up, with wind as the primary variable).

The most important Type-II uncertainties are the distribution of wind speed (i.e., uncertainty in Vw value associated with a certain exceedence probability), the uncertainty in capacity (limit-state equation), and the uncertainty in the calculation of the mean force on the vessel (which controls vessel offset). Also important are the uncertainty in the stress calculations (for surface locations), Cd at depth (for bottom locations), and Cd in wave zone (for surface locations). These conclusions about uncertainty depend, of course, on the coefficients of variation selected for the various Type-II uncertainties (see Table 2-10).

3. Analysis of Wave-Cycle Fatigue

3.1 INTRODUCTION

The inputs to the probabilistic analysis of wave-cycle fatigue for a floating structure fall in the same general categories as the inputs for the analysis of extreme loads. These inputs consist of a probabilistic characterization of the long-term metocean environment, models for the calculation of vessel motions given the metocean conditions, models for the calculation of stresses in the riser given the metocean conditions and global response, and limit-state models that define the occurrence of failure (i.e., fatigue curves). All these inputs are then used to construct a reliability model, which is used to calculate the probability of failure due to wave effects and vessel motions during the riser 15-year life.

3.2 LONG-TERM METOCEAN MODEL

The long-term metocean model for this study was developed from GLOW (Gulf Long Term Weather) results for a site located approximately 100 mi SE of the Mississippi Delta. These GLOW results contain hindcast values of wind speed, wind direction, significant wave height (Hs), and wave peak period (Tp) at three-hour intervals during five years. These five years were selected as representative of the long-term average environment.

As was done in the analysis of extremes, the wind speed Vw will be treated as the primary metocean variable for the long-term model. Significant wave height Hs is defined by means of the conditional distribution of Hs given Vw. Peak period Tp will be defined by means of a conditional distribution of Tp|Hs. Although direction information is available in the GLOW results, this information will not be used. Table 3-1 show the scatter tables for Vw and Hs and for Hs and Tp that were calculated from the GLOW results.

For the purposes of the fatigue reliability calculations, one can characterize the environment in terms of scatter diagrams or in terms of continuos probability distributions. This study will use continuous distributions, which will described below.

The distribution of wind speed Vw (m/sec) is given by a shifted lognormal distribution of the form

$$f_{V_w}(v)=\frac{1}{(v-v_0)\sigma}\phi\left[\frac{\ln(v-v_0)-m}{\sigma}\right] \qquad (3\text{-}1)$$

where v_0=1.58m/s, m=1.65, σ=0.412, and φ is the standard normal density function. Figure 3-1 compares this distribution shape to the observed GLOW results and to other distribution shapes. The conditional distribution of Hs given Vw is fit with a lognormal distribution, with a conditional median given by the expression:

$$\hat{H}_S(m) = 0.0472\left[V_W(m/\sec)\right]^{1.6396} \tag{3-2}$$

which is shown in Figure 3-2.

The conditional standard deviation of ln[Hs(m)|Vw] is not constant, as shown in Figure 3-3. We fit this standard deviation as linear for Vw < 8 m/sec, with values of 0.27 and 0.11 for Vw=4 and 8 m/sec respectively, and equal to 0.11 for Vw>8 m/sec.

The conditional distribution of peak period Tp|Hs is also lognormal, with conditional median and logarithmic standard deviation given by the expressions:

$$\hat{T}_P(\sec) = 4.55\left[H_S(m)\right]^{0.534} \tag{3-3}$$

$$\sigma_{\ln(T_p|H_S)} = 0.125\left[H_S(m)\right]^{-0.546} \tag{3-4}$$

Figures 3-4 and 3-5 compare these expressions to the GLOW results. Note that the above equations imply that $\sigma_{T_p|H_S}$ is roughly constant (i.e., the exponents in the above two equations are nearly identical), which is consistent with the fractile curves in Figure 3-5

This metocean model does not include the effect of hurricanes, which will contribute to sea states with Hs higher than 6 m. The calculations will consider values of Vw and Hs higher than those in the Glow results, but this will be done by extending the tail of the Vw distribution. This approach will consider hurricane sea states in the calculations, but the associated rates of occurrence will underestimate the true rates for these sea states. The inclusion of hurricanes would have increased the fatigue failure probabilities at locations sensitive to high seastates (near the top of the riser).

Current was neglected in these fatigue calculations. This practice is conservative because current has the effect of increasing the mean offset, thereby increasing the stiffness of the vessel in the direction of the mean offset, thereby decreasing the amplitude of wave and wind-induced motions in that direction.

In addition to the above metocean models, we also fit the following shifted lognormal model for the marginal distribution of Hs, for use in generating the figures of contribution to fatigue as a function of Hs and Tp (this model was not used in the reliability calculations)

$$f_{H_S}(h) = \frac{1}{(h-h_0)\sigma}\phi\left[\frac{\ln(h-h_0)-m}{\sigma}\right] \tag{3-5}$$

where h_0=0.1636 m, m=-0.09145 m, and σ=0.1636.

Table 3-1. Scatter diagrams of Vw, Hs, and Tp. Values of variables represent bin lower bounds.

	Hs (m)													
Vw (m/s)	**0.00**	**0.25**	**0.75**	**1.25**	**1.75**	**2.25**	**2.75**	**3.25**	**3.75**	**4.25**	**4.75**	**5.25**	**5.75**	**Total**
0.00	0.0000	0.0000	0.0000	0.0000	0.0000	0.0000	0.0000	0.0000	0.0000	0.0000	0.0000	0.0000	0.0000	0.0000
1.25	0.0029	0.0180	0.0005	0.0001	0.0000	0.0000	0.0000	0.0000	0.0000	0.0000	0.0000	0.0000	0.0000	0.0215
3.75	0.0005	0.2496	0.1543	0.0095	0.0010	0.0000	0.0001	0.0001	0.0000	0.0000	0.0000	0.0000	0.0000	0.4151
6.25	0.0000	0.0021	0.1861	0.1379	0.0142	0.0019	0.0002	0.0001	0.0000	0.0000	0.0000	0.0000	0.0000	0.3424
8.75	0.0000	0.0000	0.0001	0.0332	0.0831	0.0376	0.0042	0.0003	0.0001	0.0000	0.0000	0.0000	0.0000	0.1587
11.25	0.0000	0.0000	0.0001	0.0000	0.0023	0.0191	0.0222	0.0058	0.0010	0.0010	0.0000	0.0000	0.0000	0.0514
13.75	0.0000	0.0000	0.0000	0.0000	0.0000	0.0003	0.0011	0.0046	0.0025	0.0005	0.0003	0.0000	0.0000	0.0093
16.25	0.0000	0.0000	0.0000	0.0000	0.0000	0.0000	0.0000	0.0001	0.0003	0.0005	0.0003	0.0002	0.0001	0.0015
Total	0.0034	0.2696	0.3410	0.1807	0.1007	0.0589	0.0278	0.0110	0.0039	0.0000	0.0000	0.0000	0.0000	1.0000

	Hs (m)													
Tp (sec)	**0.00**	**0.25**	**0.75**	**1.25**	**1.75**	**2.25**	**2.75**	**3.25**	**3.75**	**4.25**	**4.75**	**5.25**	**5.75**	**Total**
0.00	0.0000	0.0000	0.0000	0.0000	0.0000	0.0000	0.0000	0.0000	0.0000	0.0000	0.0000	0.0000	0.0000	0.0000
1.00	0.0031	0.0678	0.0000	0.0000	0.0000	0.0000	0.0000	0.0000	0.0000	0.0000	0.0000	0.0000	0.0000	0.0709
2.00	0.0000	0.1585	0.0138	0.0000	0.0000	0.0000	0.0000	0.0000	0.0000	0.0000	0.0000	0.0000	0.0000	0.1724
3.00	0.0001	0.0180	0.0297	0.0000	0.0000	0.0000	0.0000	0.0000	0.0000	0.0000	0.0000	0.0000	0.0000	0.0478
4.00	0.0002	0.0221	0.2443	0.0164	0.0000	0.0000	0.0000	0.0000	0.0000	0.0000	0.0000	0.0000	0.0000	0.2830
5.00	0.0001	0.0024	0.0493	0.1352	0.0125	0.0001	0.0000	0.0000	0.0000	0.0000	0.0000	0.0000	0.0000	0.1995
6.00	0.0000	0.0003	0.0020	0.0264	0.0615	0.0035	0.0000	0.0000	0.0000	0.0000	0.0000	0.0000	0.0000	0.0937
7.00	0.0000	0.0003	0.0009	0.0021	0.0247	0.0443	0.0062	0.0001	0.0000	0.0000	0.0000	0.0000	0.0000	0.0786
8.00	0.0000	0.0002	0.0007	0.0005	0.0017	0.0103	0.0198	0.0075	0.0009	0.0000	0.0000	0.0000	0.0000	0.0417
9.00	0.0000	0.0000	0.0001	0.0001	0.0002	0.0007	0.0018	0.0032	0.0025	0.0010	0.0003	0.0000	0.0000	0.0099
10.00	0.0000	0.0000	0.0001	0.0001	0.0001	0.0000	0.0000	0.0001	0.0005	0.0008	0.0003	0.0002	0.0001	0.0023
11.00	0.0000	0.0000	0.0000	0.0000	0.0000	0.0001	0.0000	0.0001	0.0000	0.0001	0.0000	0.0000	0.0000	0.0002
Total	0.0034	0.2696	0.3410	0.1807	0.1007	0.0589	0.0278	0.0110	0.0039	0.0019	0.0006	0.0002	0.0001	1.0000

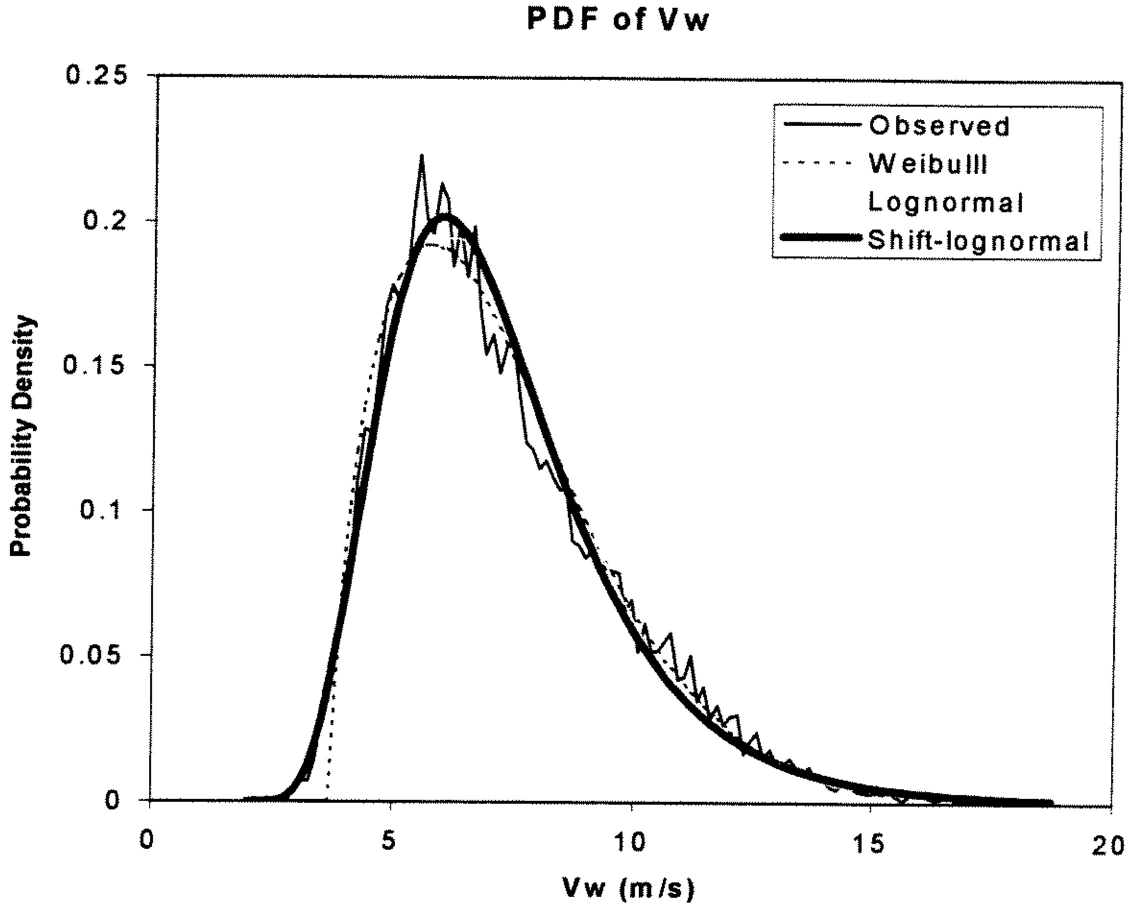

Figure 3-1. Observed distribution of wind speed from GLOW results and shifted lognormal distribution fit. Other distribution fits also shown.

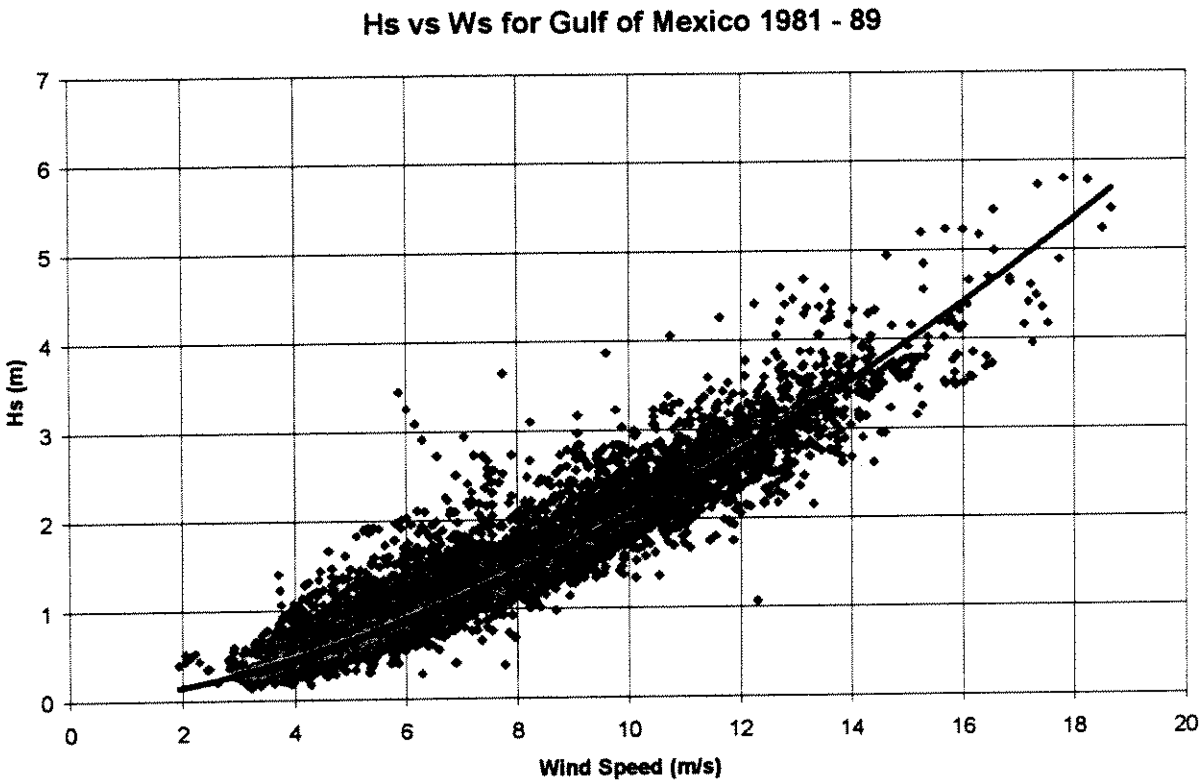

Figure 3-2. Model for median value of Hs|Vw is compared to GLOW results.

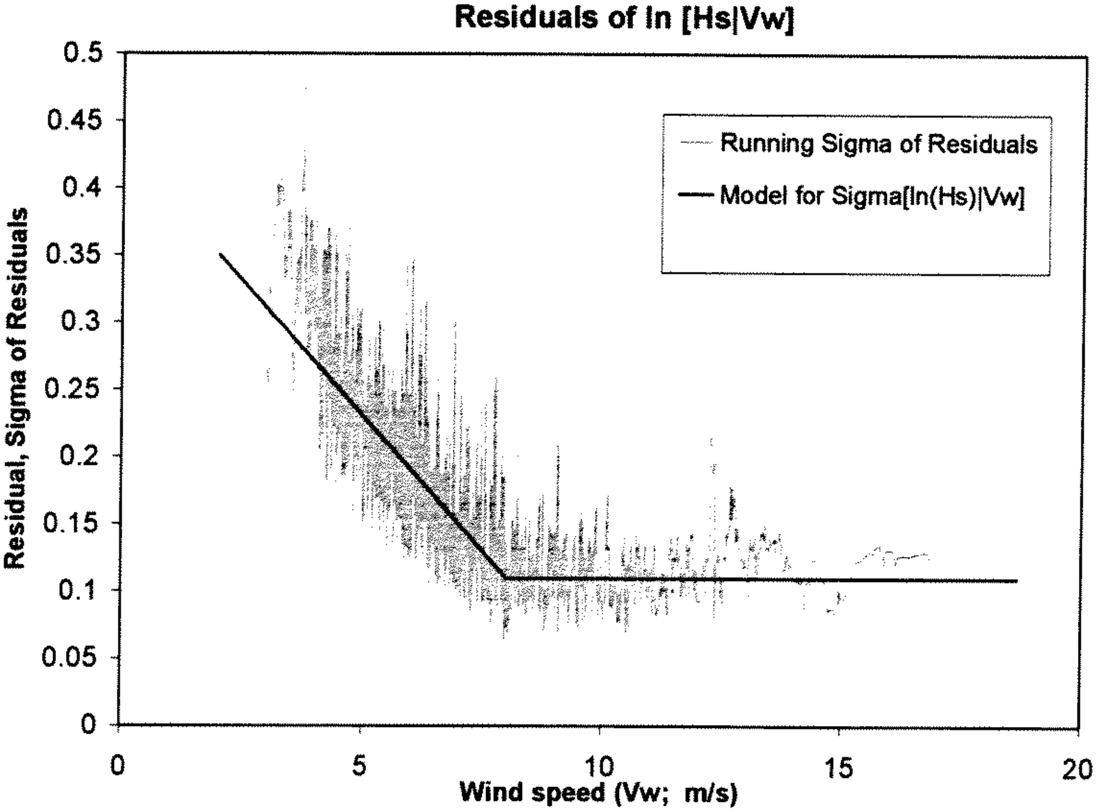

Figure 3-3. Model for the standard deviation of ln[Hs|Vw] and running average of observed residuals.

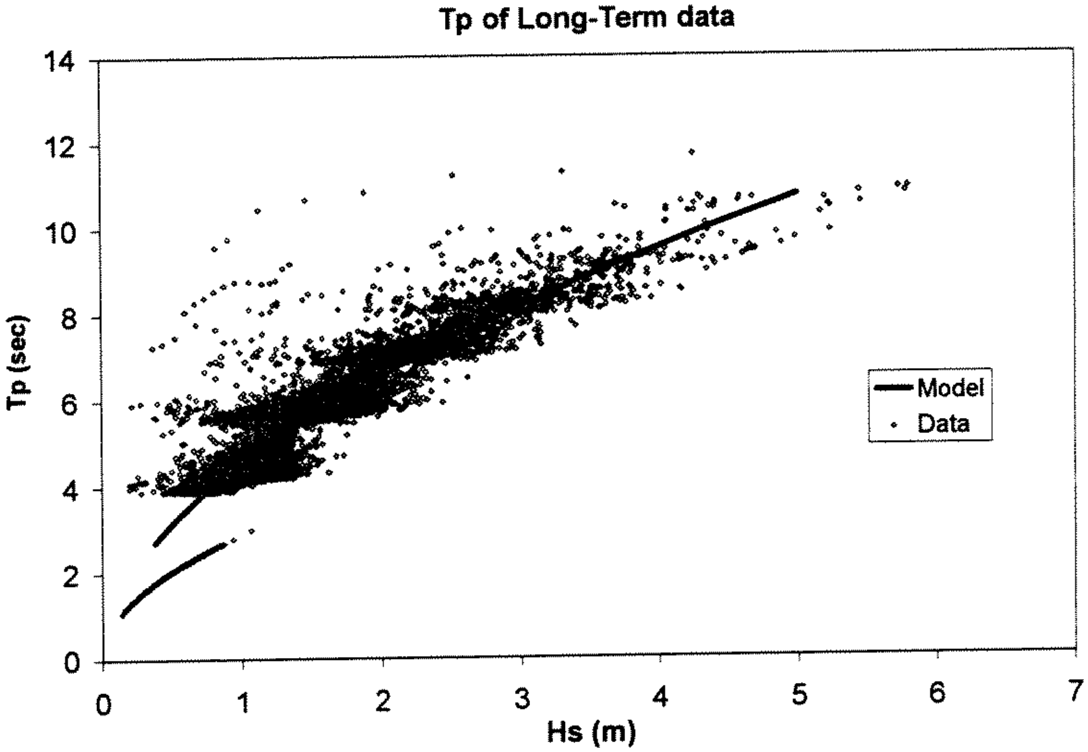

Figure 3-4. Model for the median value of Tp|Hs is compared to GLOW results.

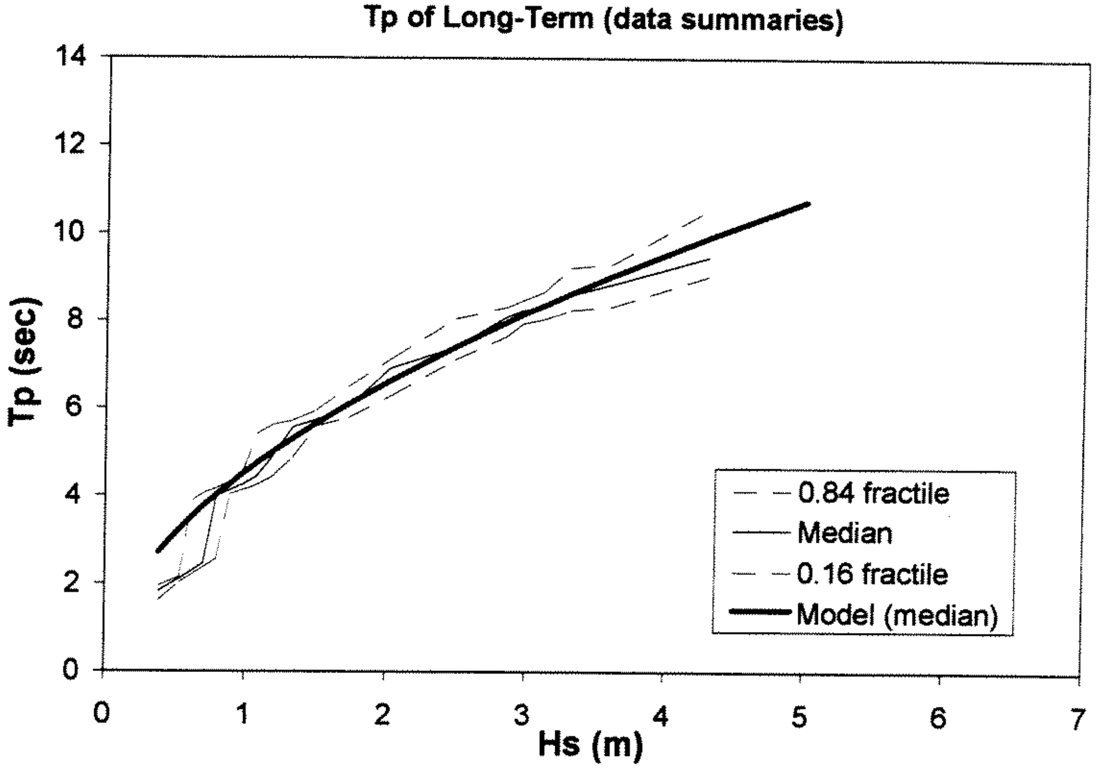

Figure 3-5. Model for median Tp|Hs is compared to fractiles from GLOW results.

3.3 GLOBAL RESPONSE MODELS

In principle, the fatigue calculations used the same global-response models documented in Section 2.3 to describe the vessel motions. These models consist of algorithms to calculate the mean offset and the rms low-frequency offset, as well as the wave-frequency RAO used to calculate the wave-frequency vessel motions. In addition, this study obtained from Amoco the following information on the mean and low-frequency offsets used in the Marlin riser design (Table 3-2).

Table 3-2 TLP Offsets used in the Marlin Riser Fatigue Calculations

Bin No.	Hs (ft)	Tp (sec)	Vw (fps)	Mean Offset (ft)	rms Offset (ft)*	Tz (sec)
1	2.25	4.5	22.5	4.3	4.7	408
2	3.75	5.5	22.5	6.1	4.0	335
3	5.25	6.5	27.5	10.5	5.1	254
4	6.75	7.5	32.5	15.0	5.3	211
5	8.25	7.5	37.5	19.7	5.7	182
6	9.75	8.5	42.5	24.2	5.9	165
7	11.25	9.5	45.0	26.9	6.3	164
8	13.00	9.5	48.8	31.8	8.4	171
9	15.00	10.5	52.5	35.8	9.1	171
10	17.00	10.5	52.5	38.1	10.2	168
11	20.00	10.5	57.0	44.5	11.3	167
12	20.00	11.5	57.0	42.0	9.9	170
13	24.00	10.5	66.0	60.0	14.9	162
14	24.00	12.5	66.0	53.2	11.8	168
15	28.00	12.5	84.4	80.4	15.9	158
16	32.00	12.0	96.4	102.6	19.3	148
17	37.40	14.2	108.3	134.7	17.9	137
18	41.70	14.9	120.2	156.6	18.8	128

* 45-degree heading (worst direction) is assumed.

Figures 3-6 through 3-8 compare the mean offset, low-frequency rms offset, and zero-crossing period (Tz) obtained using the models from Section 2.3 ("Calculated") to those used in the Marlin design ("Amoco"). Results are consistent for the mean offset and for low-frequency vessel motions for bins 5 and above. No explanation was found for the discrepancies that occur at bins 1 through 4. Focusing on the Tz value, we note that the lengthening that occurs at those sea states is due to either 1) a shift in the fundamental period of the vessel as a result of a drastic reduction (by a factor of 4) in the lateral stiffness of the vessel, or 2) to a shift in Tz away from the fundamental period of the vessel as a result of a significant change in the spectra of the low-frequency wind and wave forces acting on the vessel. The factor of four discrepancy in low-frequency rms is consistent with the first of these explanations. Our analysis shows no indication of stiffness reduction or of shifts in the force spectra that would cause shifts in Tz.

In spite of communications with Amoco personnel, we were not able to determine the source of these discrepancies. This study will use the response models from Section 2.3. Use of the Amoco model would have produced higher failure probabilities for those locations that are most affected by low and intermediate sea states (locations at the bottom of the riser).

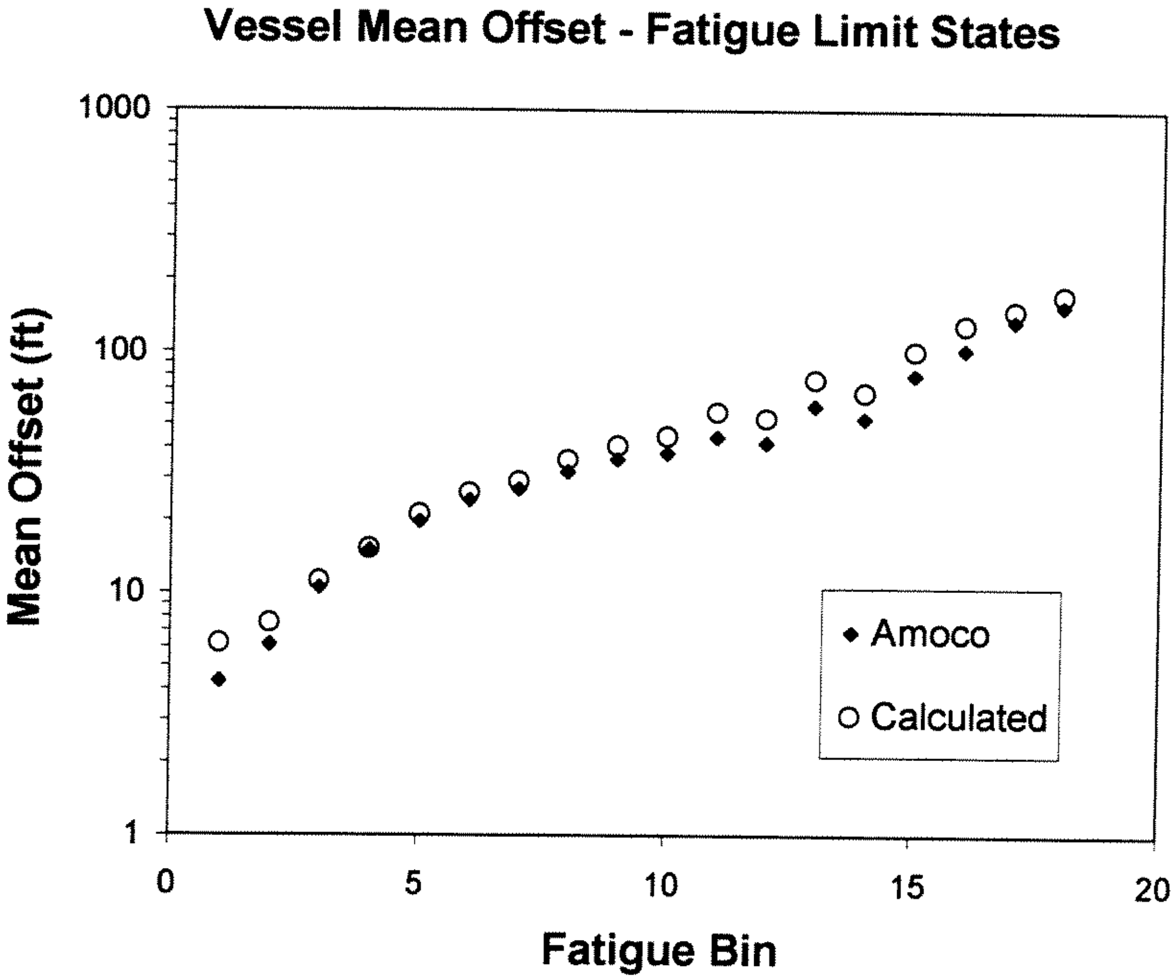

Figure 3-6. Comparison of mean offset calculated in this study to values used in the fatigue design of the Marlin risers.

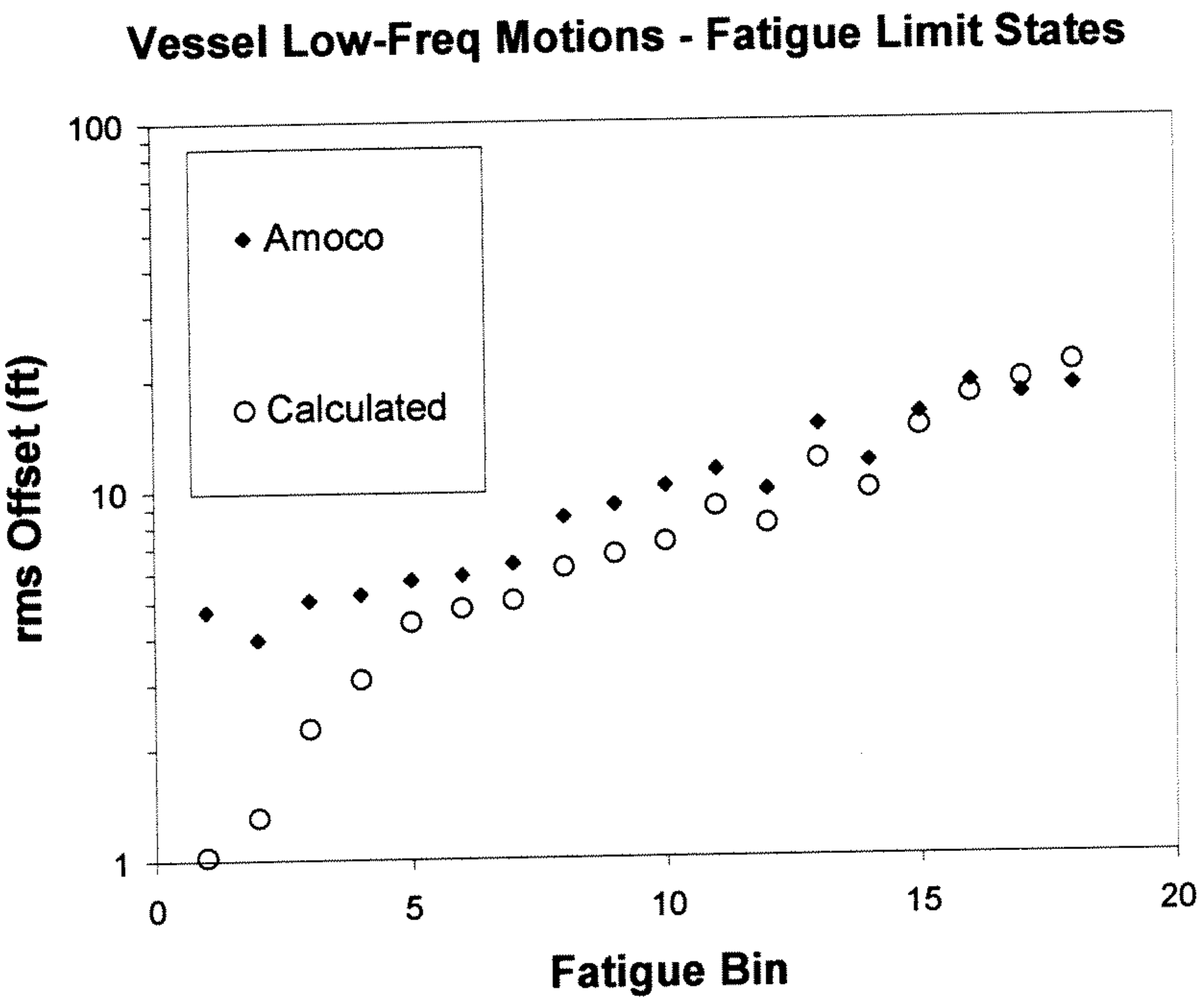

Figure 3-7. Comparison of low-frequency rms offset calculated in this study to values used in the fatigue design of the Marlin risers.

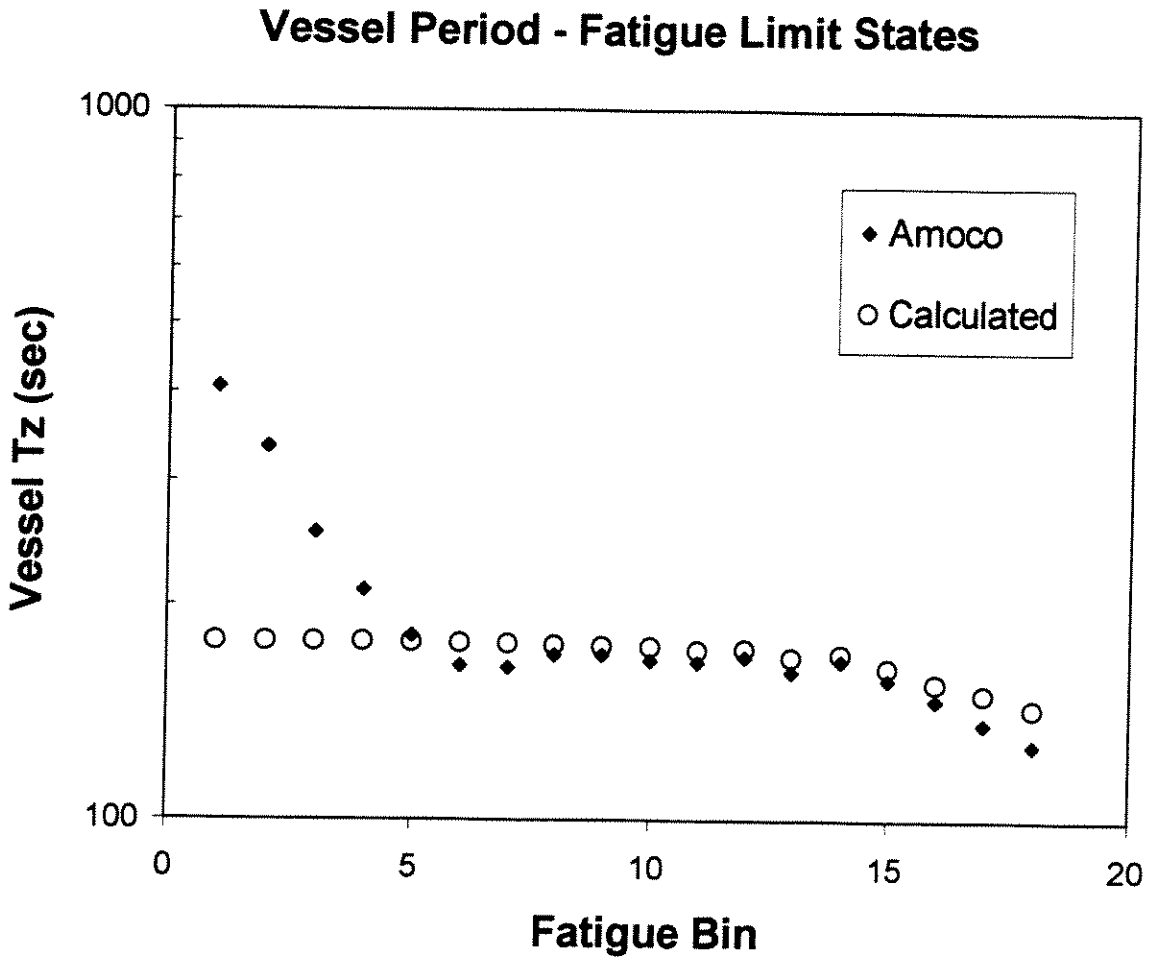

Figure 3-8. Comparison of low-frequency zero-crossing period Tz calculated in this study to values used in the fatigue design of the Marlin risers.

3.4 CALCULATION OF FATIGUE STRESSES

The calculation of fatigue stresses consists of two parts, as follows: 1) calculation of rms stresses in the riser pipe for given combinations of sea state and global response, and 2) calculation of stress amplification factors (SAF) that convert stresses on the riser pipe into hot-spot stresses at the fatigue-sensitive locations. The calculation of rms stresses follows a procedure similar to that of Section 2.4, and consists on the selection of parameters combinations to run (experimental design), the TIARA runs to calculate stresses for each combination of parameters, and the fitting of response surfaces. The calculation of stress amplification factors considers the local configuration of the connector or weld and the associated fabrication tolerances.

3.4.1 Experimental Design and TIARA Runs

The parameter combinations for the TIARA runs were developed as follows:

1. Consider five different values of windspeed (5, 7.5, 11, 16, and 24 m/sec).

2. For each value of wind speed Vw, use a "2^{7-3} + central point" design (see Box and Draper, 1987) to generate 8 combinations of Hs|Vw, Tp|Hs, Cd(<500'), Cd(>500'), and the modeling errors in the RAO, the static offset, and the low-frequency offset. This corresponding design matrix for one value of Vw is shown in Table 3-3. A value of ±1 indicates that the corresponding variable will be given a value equal to its conditional mean (given the values of all variables to its left) ±1.5 its conditional standard deviation. These calculations used preliminary forms of the metocean model, as well as the final model for uncertainties in the Cd's and modeling errors (to be discussed in Section 3.5).

3. For each combination of Vw, Hs|Vw, Tp|Hs, Cd(<500'), Cd(>500'), and modeling errors, compute values of mean offset and rms offset using the global-response model. Table 3-4 shows the resulting table of all the metocean and global-response inputs to TIARA. These calculations were performed by Stress Engineering Services.

The calculation of rms stresses used the TIARA program and the same riser configuration that was used in Section 2.4. Calculations did not consider wave-zone effects, as these require more

Table 3-3 Design Matrix used in Fatigue Runs
(for one value of Wind Speed)

Hs|Vw	Tp|Hs	Cd(<500')	Cd(>500')	ϵ_{RAO}	ϵ_{Xmean}	ϵ_{XrmsLF}
0	0	0	0	0	0	0
-1	-1	-1	1	1	1	-1
-1	-1	1	1	-1	-1	1
-1	1	-1	-1	1	-1	1
-1	1	1	-1	-1	1	-1
1	-1	-1	-1	-1	1	1
1	-1	1	-1	1	-1	-1
1	1	-1	1	-1	-1	-1
1	1	1	1	1	1	1

Table 3-4 Parameter Values used in the TIARA Runs for Wave-Cycle Fatigue

run no.	Hs(ft)	Tp(sec)	Curr(fps)	Mean Offsset (ft)	X_{rmsLF} (ft)	Tz(sec)	ϵ_{RAO}	Cd (<500')	Cd (>500')
1	2.2	3.5	0.0	4.5	0.51	178	1.00	1.20	0.70
2	1.5	1.8	0.0	6.8	0.23	178	1.08	0.66	1.02
3	1.5	1.8	0.0	3.7	0.66	178	0.93	1.74	1.02
4	1.5	4.4	0.0	2.2	0.66	178	1.08	0.66	0.39
5	1.5	4.4	0.0	4.2	0.23	178	0.93	1.74	0.39
6	3.1	3.1	0.0	9.3	1.02	178	0.93	0.66	0.39
7	3.1	3.1	0.0	5.0	0.37	178	1.08	1.74	0.39
8	3.1	5.7	0.0	3.0	0.37	178	0.93	0.66	1.02
9	3.1	5.7	0.0	5.5	1.02	178	1.08	1.74	1.02
10	4.2	5.0	0.0	9.7	1.48	178	1.00	1.20	0.70
11	3.5	3.3	0.0	14.1	0.66	178	1.08	0.66	1.02
12	3.5	3.3	0.0	7.6	1.86	178	0.93	1.74	1.02
13	3.5	6.0	0.0	5.4	1.86	178	1.08	0.66	0.39
14	3.5	6.0	0.0	10.1	0.66	178	0.93	1.74	0.39
15	5.1	4.4	0.0	16.8	2.73	178	0.93	0.66	0.39
16	5.1	4.4	0.0	9.1	0.98	178	1.08	1.74	0.39
17	5.1	7.0	0.0	6.4	0.97	178	0.93	0.66	1.02
18	5.1	7.0	0.0	11.8	2.71	178	1.08	1.74	1.02
19	7.9	7.0	0.0	20.3	4.36	178	1.00	1.20	0.70
20	6.7	5.2	0.0	28.1	1.86	177	1.08	0.66	1.02
21	6.7	5.2	0.0	15.1	5.26	178	0.93	1.74	1.02
22	6.7	7.9	0.0	12.0	4.43	178	1.08	0.66	0.39
23	6.7	7.9	0.0	22.2	1.57	178	0.93	1.74	0.39
24	9.3	6.4	0.0	32.5	8.16	177	0.93	0.66	0.39
25	9.3	6.4	0.0	17.5	2.95	178	1.08	1.74	0.39
26	9.3	9.1	0.0	13.7	1.69	178	0.93	0.66	1.02
27	9.3	9.1	0.0	25.4	4.70	177	1.08	1.74	1.02
28	14.5	9.7	0.0	41.7	6.67	176	1.00	1.20	0.70
29	12.3	7.6	0.0	55.4	4.34	174	1.08	0.66	1.02
30	12.3	7.6	0.0	29.8	12.57	177	0.93	1.74	1.02
31	12.3	10.3	0.0	25.4	8.71	177	1.08	0.66	0.39
32	12.3	10.3	0.0	47.2	3.02	175	0.93	1.74	0.39
33	17.1	9.3	0.0	63.7	11.89	172	0.93	0.66	0.39
34	17.1	9.3	0.0	34.3	4.43	177	1.08	1.74	0.39
35	17.1	12.0	0.0	29.0	3.19	177	0.93	0.66	1.02
36	17.1	12.0	0.0	53.8	8.61	174	1.08	1.74	1.02
37	28.2	13.8	0.0	88.6	11.96	167	1.00	1.20	0.70
38	23.9	11.3	0.0	114.6	6.16	160	1.08	0.66	1.02
39	23.9	11.3	0.0	61.7	19.88	173	0.93	1.74	1.02
40	23.9	14.0	0.0	55.7	18.38	174	1.08	0.66	0.39
41	23.9	14.0	0.0	103.5	5.80	163	0.93	1.74	0.39
42	33.2	13.7	0.0	129.9	16.44	156	0.93	0.66	0.39
43	33.2	13.7	0.0	69.9	7.00	171	1.08	1.74	0.39
44	33.2	16.4	0.0	62.8	6.53	172	0.93	0.66	1.02
45	33.2	16.4	0.0	116.7	15.69	160	1.08	1.74	1.02

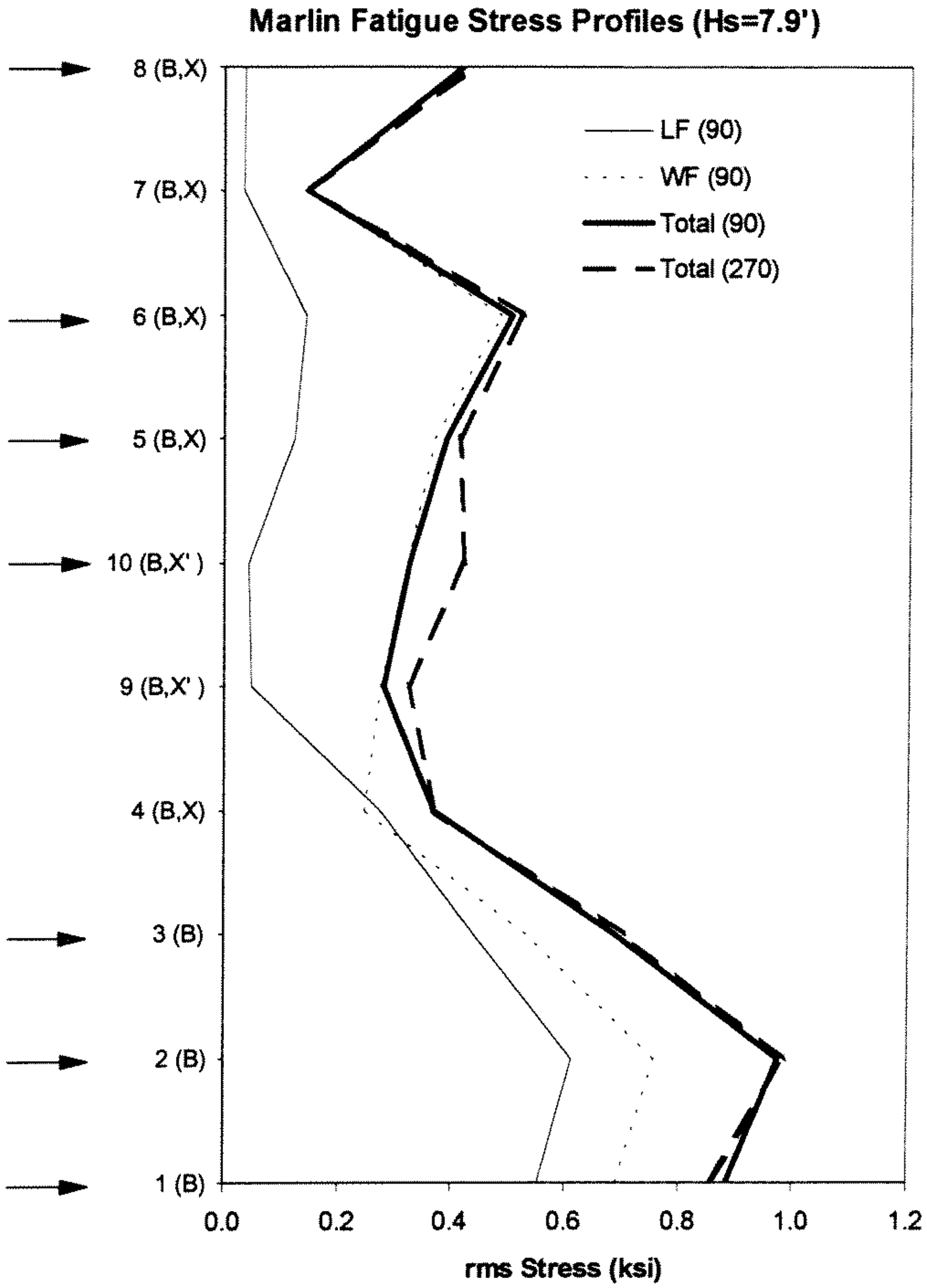

Figure 3-9. Vertical distribution of rms stresses for run number 19. Numbers along vertical axis (not to scale) indicate key locations along riser. Letters (B, X, X') indicate type of connector or weld. Arrows indicate locations selected for reliability analysis.

computationally intensive simulations in the time domain. TIARA calculations were performed for the eight locations considered in Section 2.4 and for the following two additional locations:

- Location 9, corresponding to the lowest API X' weld, at 240 feet elevation.

- Location 10, corresponding to the highest API X' weld, at 3220 feet elevation (20 feet below mean water level).

TIARA calculations were performed for weather headings of 90 degrees and 270 degrees, in order to consider the effect of seabed offset (21.9 feet). Results are in the form of low-frequency and wave-frequency rms stresses and their associated Tz and bandwidth.

Figure 3-9 shows stresses as a function of elevation for run number 19 (Hs=7.9 feet). Stresses for the 90-degree direction are decomposed into low-frequency and wave-frequency. The vertical axis (not to scale) indicates Location number and the type of connector or weld (see next section). Low-frequency stresses are comparable to wave-frequency stresses at Location 4 and below, but are negligible at higher locations. Based on the observed stress profile, Locations 1, 2, 3, 10, 5, 6, and 8 are selected for consideration in the reliability analysis. Location 3 was selected because it has a high stress amplification factor, as we will see in Section 3.4.3. The 90-degree results will be used for all locations except 10.

3.4.2 Fitting of Response Surfaces

As done in Section 2.4, the functional forms of the response surface are relatively simple and guided by physical considerations. Whenever possible, the same functional forms of Section 2.4 were used. The scatter of the TIARA results about the response surface is capture by an error term ε with standard deviation σ_ε. For the rms stresses, this scatter term is multiplicative and is captured by a logarithmic standard deviation $\sigma_{\ln\epsilon}$.

The response surface for the low-frequency rms stress σ_{rmsLF} uses the same functional form used in Section 2.4 (except for the current term, which is removed), obtaining

$$\sigma_{rmsLF} = c_1 X_{rmsLF} X_m + \frac{c_1}{2} X_{rmsLF}^2 + c_2 X_{rmsLF} + c_3 \left(\frac{X_{rmsLF}}{T_Z} \right)^2 C_{d(<500')} \tag{3-6}$$

where X_{rmsLF} is the low-frequency rms offset, X_m is the mean offset, and the c_is are empirical constants. Table 3-5 shows the calculated values of the constants and residual standard deviation. Figure 3-9 compares the response-surface results to the TIARA results for Locations 1, 3, 10, and 5. Note that low-frequency stresses are roughly ten times greater at the bottom than at the top. Note also that the scatter, as represented by $\sigma_{\ln\epsilon}$ (which is roughly equivalent to the coefficient of variation), is a few percent near the bottom and 10 to 20 percent near the surface. This scatter will be considered in the reliability calculations, where it will have the effect of amplifying the stress ranges by a factor of approximately $(1 + m^2 \sigma_{\ln\epsilon}^2 / 2)$, where m is the slope of the fatigue curve.

Table 3-5 Coefficients of Response Surface for Low-Frequency rms Stress X_{rmsLF}

Location	c_1	c_2	c_3	σ_{lne}
1	5.19E-05	0.1241	0.0000	0.0255
2	1.00E-09	0.1376	0.0000	0.0309
3	1.00E-09	0.0982	0.0000	0.0443
10	1.63E-05	0.0149	0.0000	0.1950
5	1.93E-04	0.0218	0.0000	0.1361
6	2.75E-04	0.0249	0.0000	0.1122
8	7.14E-05	0.0075	7.4854	0.1085

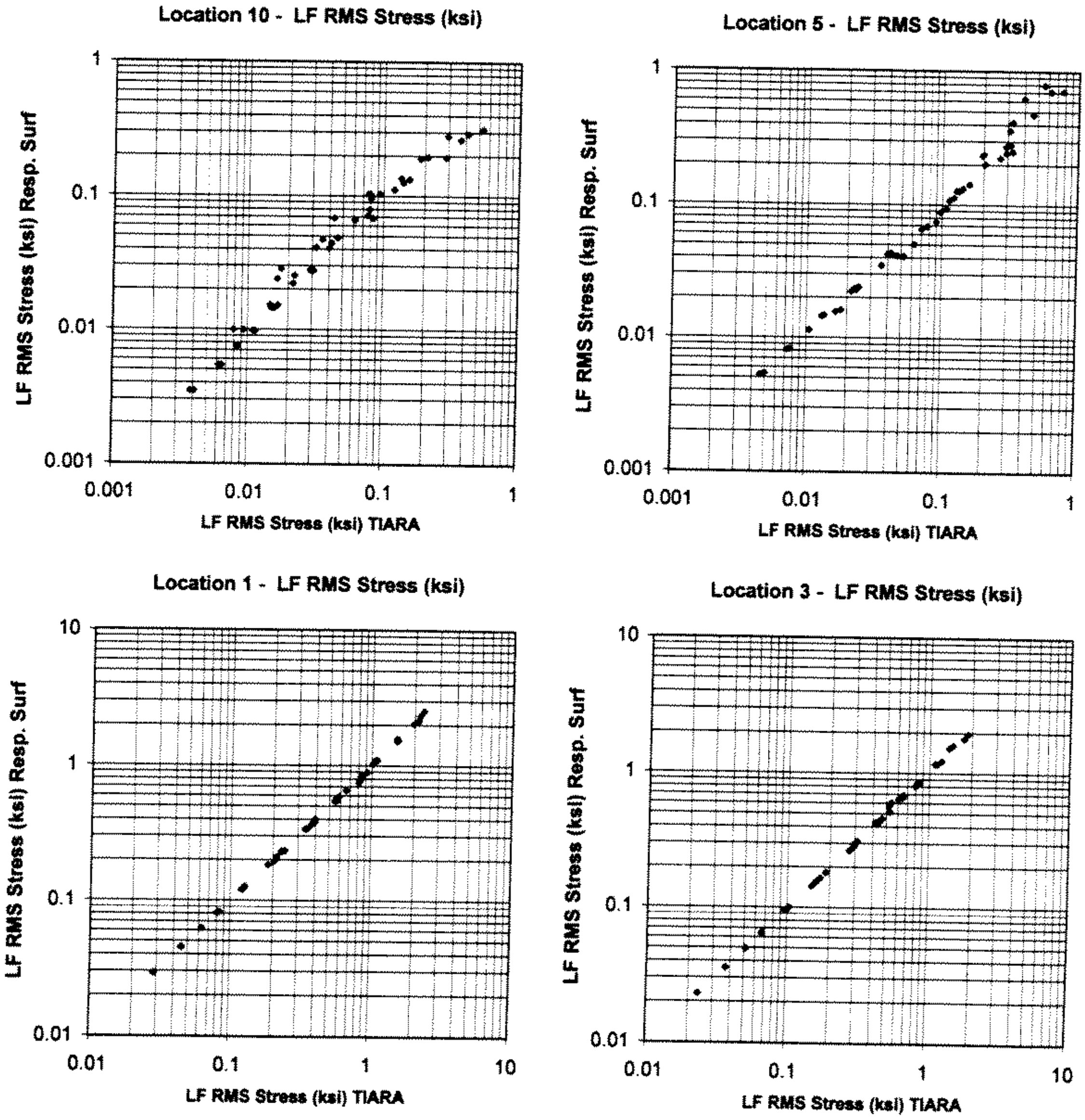

Figure 3-10. Comparison of response-surface predictions to TIARA results for low-frequency rms offset X_{rmsLF}.

The functional form of the response surface for the wave-frequency rms offset X_{rmsWF} differs from the one used in Section 2.4 in the following two respects: (1) terms involving the mean offset are not important (because the mean offset is so small), and (2) there is a significant dependence on Tp (partly as a result of the jagged shape of the vessel RAO at the wave Tp values of interest, as shown in Figure 3-11, and partly as a result of other factors related to the dynamics of the riser itself).

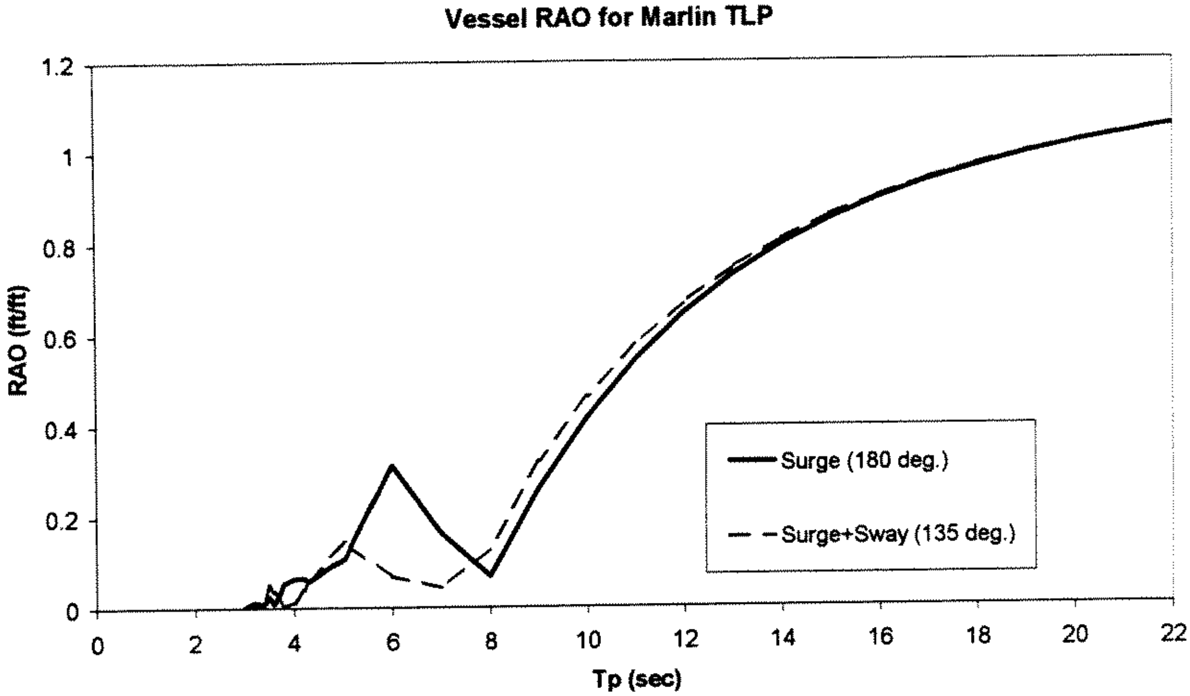

Figure 3-11. Vessel RAO shown as a function of wave peak period Tp. Source: J. Geyer, personal communication (March, 1999).

The resulting expression for the wave-frequency rms offset is

$$\sigma_{rmsWF}=\left[c_1 \left(H_S\, \epsilon_{RAO} \psi(T_P)\right)+c_2\left(H_S^2\, C_{d(<500')}\right)\right] C_{d(>500')}^{c_3} \tag{3-7}$$

where ϵ_{RAO} is an uncertain (Type-II) quantity that represents deviation from the assumed RAO, $\psi(T_p)$ is a piecewise linear function with control points at 2, 6, 10, and 15 sec. Tables 3-6 and 3-7 show the calculated coefficients. Only Location 10 (located in the wave zone) has a non-zero value of c_2, which represents the effect of wave forces acting directly on the riser. Locations at the bottom have c_3 values of approximately -0.4, indicating the beneficial effect of $C_{d(>500')}$, which provides energy dissipation. Figure 3-12 shows the term $\psi(T_p)$ for the various sites and indicates that the dependence on Tp is not due entirely to the vessel RAO, but depends on other factors related to the dynamics of the riser. Figure 3-13 compares the response-surface results to the TIARA results for Locations 1, 3, 10, and 5. Note also that the scatter, as represented by $\sigma_{\ln\epsilon}$, is larger at the bottom (roughly 17%) than at the top (roughly 10%).

As an alternative to the empirical approach used here to obtain $\psi(T_P)$, one could have used a more physical approach, where one considers the dominant modes of riser response and one integrates the associated modal transfer functions together with the vessel RAO and the wave spectrum, to obtain an numerical form for $\psi(T_P)$. Hybrid approaches, where some of the terms in

Table 3-6. Coefficients of Response Surface for Wave-Frequency rms Offset X_{rmsWF}

Location	c_1	c_2	c_3	$\sigma_{\ln\epsilon}$
1	0.06300	0.00E+00	-0.38866	0.1660
2	0.05997	0.00E+00	-0.43061	0.1754
3	0.03851	0.00E+00	-0.44673	0.1816
10	0.02434	3.96E-04	-0.01037	0.0985
5	0.05522	0.00E+00	-0.04367	0.1072
6	0.06848	0.00E+00	-0.03995	0.1041
8	0.04813	0.00E+00	0.02314	0.1135

Table 3-7. Values of Function $\psi(T_p)$ at Control Points

Location	Ψ(2 sec)	Ψ(6 sec)	Ψ(10 sec)	Ψ(15 sec)
1	1.222	1.424	0.788	0.730
2	0.976	1.666	0.896	0.686
3	0.766	1.850	0.974	0.725
10	1.942	2.091	1.309	0.188
5	1.129	0.797	1.012	1.098
6	1.026	0.849	1.021	1.123
8	0.873	1.090	1.011	1.039

these transfer functions are determined empirically, are also possible. This physical approach may become necessary in the analysis of catenary or lazy-wave riser, for which dynamic effects are more important.

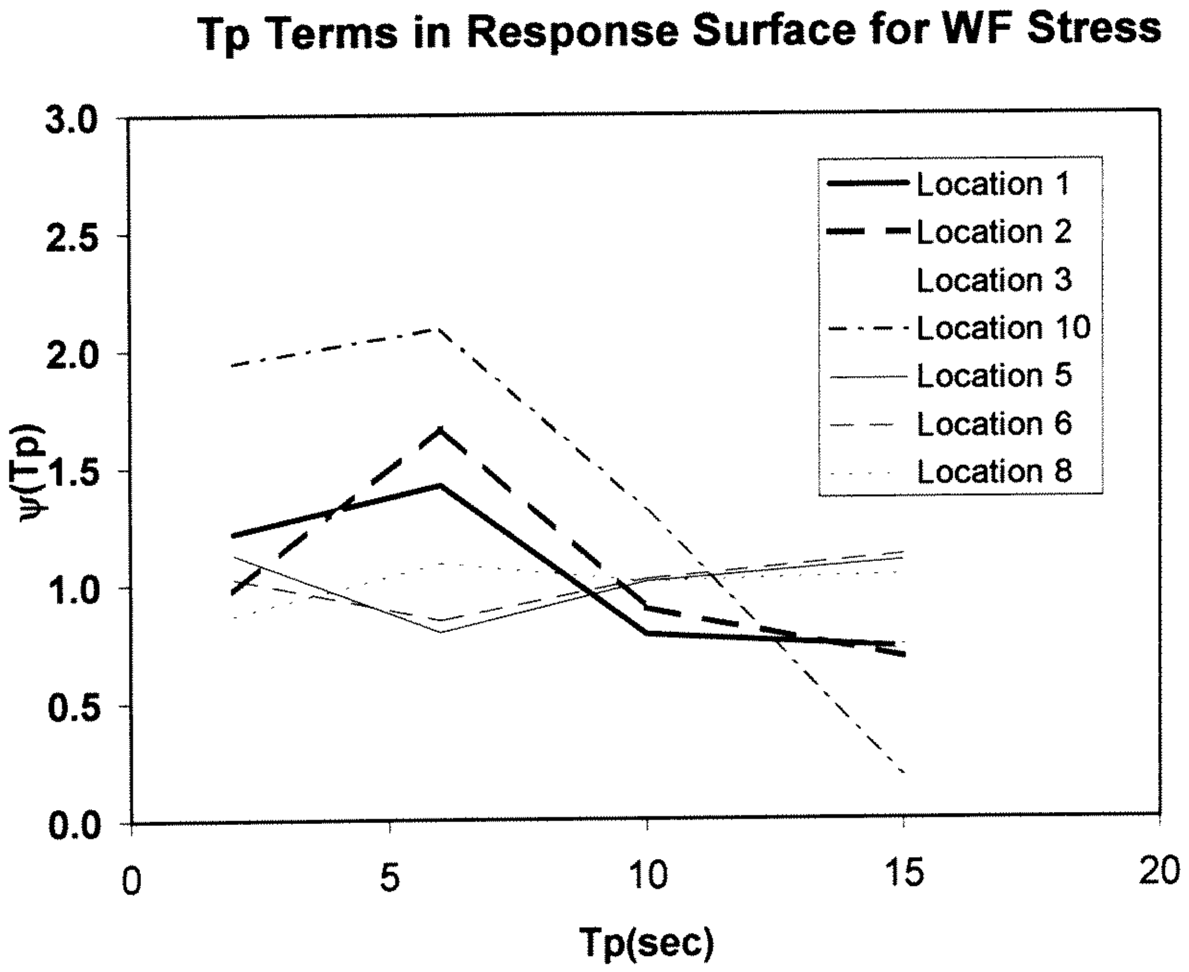

Figure 3-12. Tp-dependent term $\psi(T_p)$ in the response surface for rms wave-frequency offset.

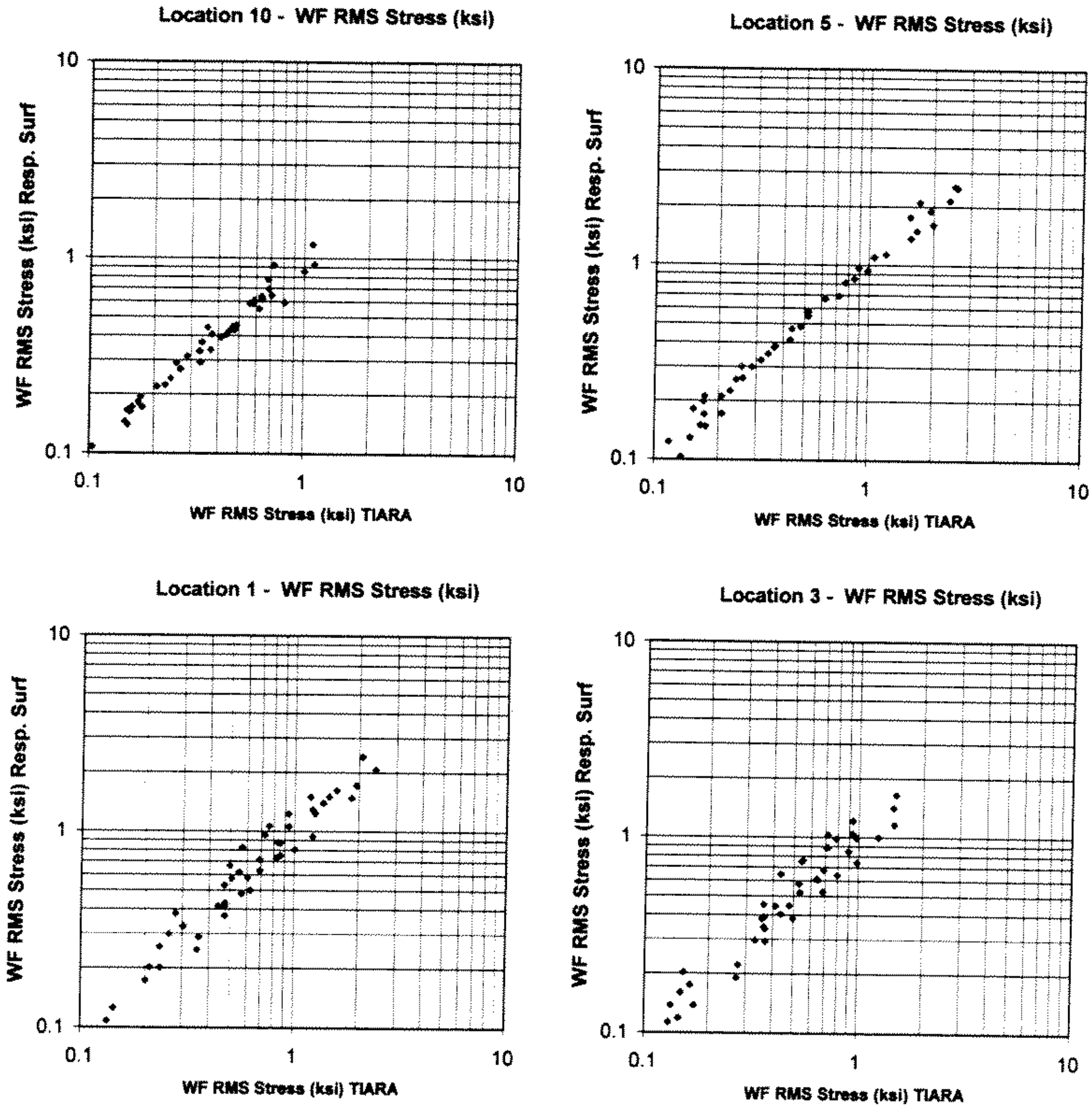

Figure 3-13. Comparison of response-surface predictions to TIARA results for wave-frequency rms offset X_{rmsWF}.

The response surface for the zero-crossing period T_Z of the wave-frequency stress has the same functional form

$$T_Z = c_1 T_P \tag{3-8}$$

Table 3-8 shows the calculated coefficient and standard deviation. Figure 3-14 compares the response-surface results to the TIARA results for Locations 1, 3, 10, and 5. Results for these four sites show a sag in the range of 3-6 sec, indicating the influence of the vessel RAO and of the riser's dynamic response. Because T_p has a moderate effect on fatigue results, this sag introduces no difficulties. In fact, the scatter in T_Z will be neglected in the reliability calculations.

Table 3-8. Coefficients of Response Surface for Wave-Frequency Zero-Crossing Period T_Z

Location	c1	σ (sec)
1	0.875	0.509
2	0.878	0.462
3	0.882	0.469
10	0.608	0.920
5	0.815	0.364
6	0.816	0.335
8	0.783	0.406

Bandwidth information for the wave-frequency components is available, but we use a constant value of $\varepsilon=0.55$ (which corresponds $\delta=0.341$ according to Equation 2-35) for all locations and sea states because bandwidth has only a moderate effect on fatigue results. In addition to the bandwidth of these two components of the dynamic stress, the reliability calculations will consider the bimodal nature of the stress. See Section 3.5 for more details.

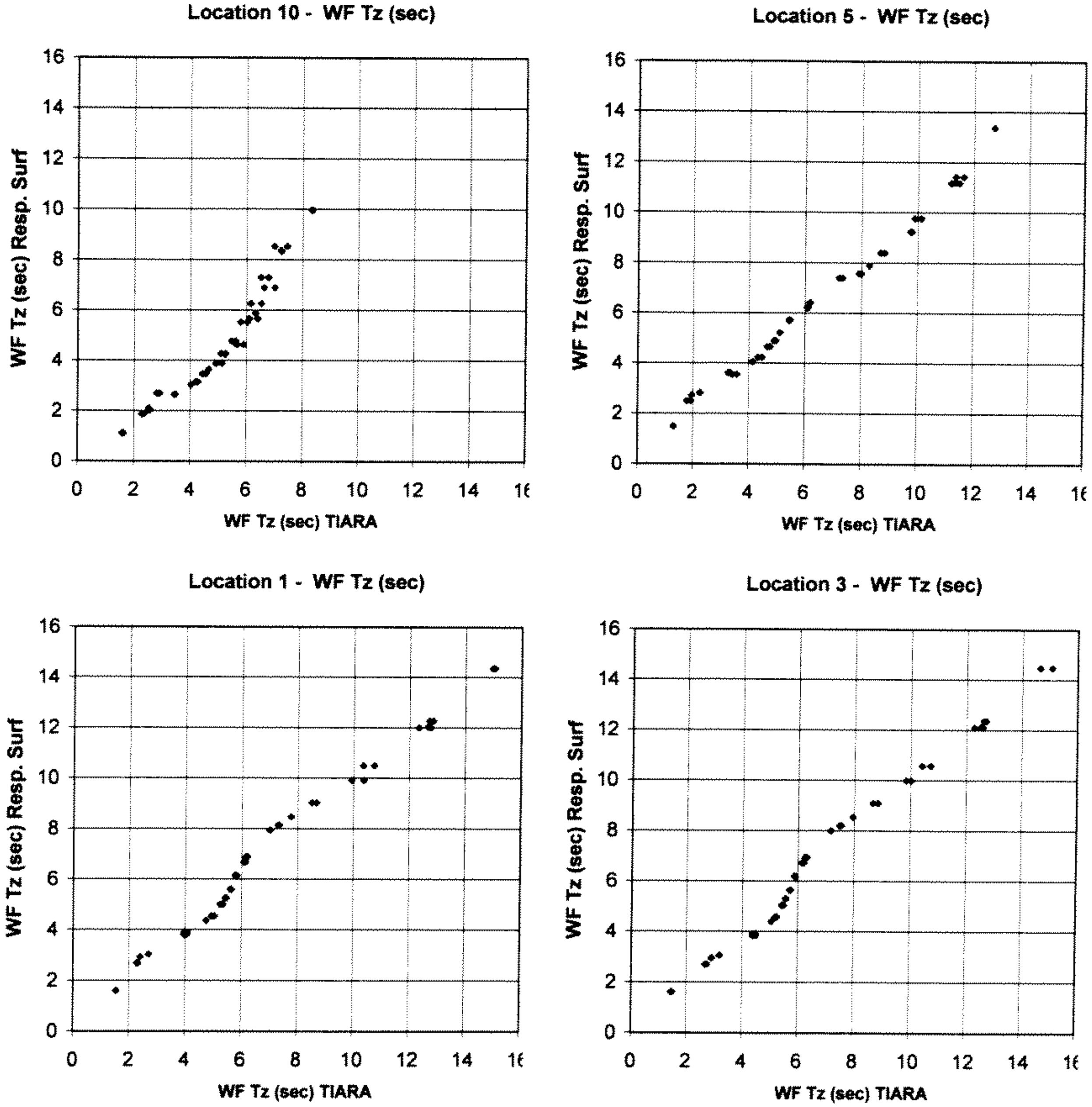

Figure 3-14. Comparison of response-surface predictions to TIARA results for wave-frequency zero-crossing period T_z.

3.4.3 Stress Amplification Factors

The riser global analysis used in the previous section assumes the riser to be composed strictly of smooth cylindrical or mildly tapered sections. Locally high component stresses arising from threads, notches, and other non-smooth profiles are not directly predicted in this analysis. In order to perform fatigue analysis for such components using the global analysis results, the ratio of peak stress in the component to nominal stress in the nearby riser wall must be known from detailed analyses performed outside of the riser analysis program. This ratio, or stress amplification factor (SAF), is then used as a multiplier for the basic pipe wall stress range at the location of interest when performing fatigue damage calculations. Alternately, if the SAF for a component is not known, the relationship between SAF and fatigue life at the location of interest can be established by post-processing the global analysis results for various SAF values. With this relationship, one can determine for a given "target" fatigue life the maximum value that the SAF may have.

The stress amplification factors obtained for the various components are given in Table 3-9. The SAFs given in "{}" were obtained from finite element analyses. The SAFs given in "[]" were estimated values. The value of the SAF was not available for the ellipse transition at the base of the stress joint (location 1), so for these components the alternate procedure of providing the maximum allowable SAF for a given target fatigue life was followed to arrive at the value in Table 3-9. This SAF is given in "()". The SAF value to use in the fatigue reliability calculations, and its associated uncertainty, were based on judgment.

Table 3-9 STRESS AMPLIFICATION FACTORS

Loc.	Component	Stress Amplification Factor	Reference Section OD x ID (inches)	Estimated Uncertainty
1	Ellipse transition at base of stress joint	(1.76)	14.360 x 9.760	-
2	Transition at top of stress joint taper	[1.10]	11.640 x 9.760	+5% / -10%
3	Connector between the TSJ and SJTP	{3.16}	11.640 x 9.760	+10% / -20%
4	Riser connector at top of SJTP Riser connector at top of SJTP weld (API-X)	{1.60} [1.00]	10.750 x 9.760 10.750 x 9.760	+10% / -20% +10% / - 0%
5	Riser connector at bottom of tens. joint Riser connector at bottom of tens. joint weld (API-X)	{1.60} [1.00]	10.750 x 9.760 10.750 x 9.760	+10% / -20% +10% / - 0%
6	Transition at bottom of tensioner joint hub region	[1.10]	10.750 x 9.760	+5% / -10%
7	Tensioner joint at load ring	{45.2} Tens. {3.00} Bend.	14.230 x 9.760 14.230 x 9.760	+10% / -80% +10% / -20%
8	Riser at tensioner rollers	[1.10]	12.750 x 9.760	+0% / -0%
9	Lowest API-X' weld	[1.00]	10.750 x 9.760	+20% / - 0%
10	Uppermost API-X' weld	[1.00]	10.750 x 9.760	+20% / - 0%

The estimated uncertainties given in Table 3-9 are intended to provide an estimate of the variation that may actually exist for the reported SAFs. For example, an SAF of 1.10 was given for the transition at the top of the stress joint taper with an estimated uncertainty of +5%/-10%. Thus, it is estimated that this SAF may actually be as high as 1.10 + (0.05) 1.10 @ 1.16, or as low as 1.10 - (0.10) 1.10 @ 1.00. In the reliability calculations, the central value will be taken as representative of the mean and the positive uncertainty range will be takes as representative of the coefficient of variation.

The SAF at the load rings constitute a special case. Two values for SAF are given in Table 3-9 for the tensioner joint at the load ring location. These two values are separate factors to be applied to the stresses arising from axial force and bending moment, respectively. These numbers represent worst-case scenarios and are therefore conservative. The large disparity in the two numbers arises from the fact that bending moment fluctuation in the tensioner joint does not have nearly as large an effect on the peak stress as do fluctuations in the tension, which are taken directly by the load ring. There is not an appreciable moment transfer between the load ring and the tensioner joint, but there is a very large transfer of tension from the load ring to the tensioner joint. Under worst-case conditions for interference between the hubs of the load ring and those of the tensioner joint, fluctuations in this tension cause very large fluctuations in peak stress.

In many fatigue reliability studies, the uncertainty in the stress amplification factor is taken as 20 to 25%. This value represents the combined effect of all factors affecting the calculated stress, not just the uncertainty in stress-amplification factors. Because this study treats the uncertainties in the global response and the stress calculations explicitly (see next section), the uncertainty of 20 to 25% is not appropriate for this study.

3.5 Fatigue Reliability Analysis: Approach and Data

According to the Palmgren-Miner hypothesis (Miner's Law), the number of cycles until failure under constant cyclical stress is related to the stress range S by the relation

$$N=KS^{-m}=e^{A}S^{-m} \tag{3-9}$$

where the intercept A and slope m are properties of the material. To extend this result to variable stresses, one defines the damage D during one cycle with stress range S as:

$$D(S)=\frac{1}{N}=e^{-A}S^{m} \tag{3-10}$$

The total damage from stress ranges with amplitudes S_1, S_2, S_3, .is then calculated as

$$D=\sum_i D(S_i)=e^{-A}\sum_i S_i^{m} \tag{3-11}$$

and it is assumed that failure will occur when D reaches unity.

For a riser exposed to the wave and wind environment during T years, the total damage is given

by

$$D=e^{-A}\sum_{\substack{i \\ \text{(all seastates)}}} E_{\text{stress amplitude}|\,i}[S^{m}]\left(\frac{T}{T_{Z_i}}\right)p_i \tag{3-12}$$

where the summation considers all sea states, and each sea state acts during a fraction p_i of the time. The dynamic stress during each sea state has an associated rms value, a zero-crossing period T_{zi}, etc. The expectation considers the random stress-range variation given the sea state. The distribution of stress range is Rayleigh if response is narrow-band. T will be taken as 15 years.

Calculation of the expectation of S^m for this study is somewhat complicated as a result of the following two factors:

1. The scatter in the response-surface fits does not allow us to predict the exact values of the low-frequency and wave-frequency rms stresses for a given sea state. Recall from Section 3.4 that the response-surface residuals have coefficients of variation of up to 20%.

2. The presence of well-separated low-frequency and wave-frequency stresses makes the assumption of Rayleigh-distributed stress ranges very conservative (see Jiao and Moan, 1990).

The approach developed here, modified from Jiao and Moan (1990) and Jiao (1992), decomposes the total damage into the sum of damage from two kinds of stress ranges. The first kind corresponds to the wave-frequency stresses alone, the second kind corresponds to the low-frequency stress ranges and contains contributions from both the low-frequency and the wave-frequency stresses. This decomposition is consistent with methods such as rainflow counting, which are used to determine the stress ranges of arbitrary stress histories.

Using a Rayleigh distribution for the first kind of stress ranges (because the wave-frequency stress is narrow-banded) and considering the lognormal scatter of the response surface for wave-frequency stress, we obtain the following expression:

$$E[S^m]_{WF} = \left(2\sqrt{2}\,\hat{\sigma}_{rms\,WF}\right)^m \Gamma\left(\frac{m}{2}+1\right) \exp\left(\frac{1}{2}\left(m\,\sigma_{\ln\sigma_{rms\,WF}}\right)^2\right)$$

where $\hat{\sigma}_{rms\,WF}$ is the wave-frequency rms stress predicted by Equation 3-7 (we include the hat here to emphasize that this quantity is a median value) and $\sigma_{\ln X_{rms\,WF}}$ is the standard deviation in Table 3-6. The first kind of stress ranges have zero-crossing period $T_{Z_{WF}}$.

Evaluation of the expectation $E[S^m]_{WF+LF}$ for the second type of stress ranges involves the expected value of the quantity $[2(R_{LF}+R_{WF})]^m$, where R_{LF} and R_{WF} have Rayleigh distributions. Note that both the wave-frequency and low-frequency stresses contribute to the amplitude of this stress range. Furthermore, the rms values of the random processes that generate these two Rayleigh distributions are lognormal (with medians given by Eqs. 3-6 and 3-7 and logarithmic standard deviations contained in tables 3-5 and 3-6, respectively). Thus, evaluation of $E[S^m]_{LF+WF}$ involves a quadruple integral, which is evaluated numerically using gaussian quadrature. Alternatively, one could have avoided numerical integration over the two Rayleigh distributions by using the approximate result in Equation 38 of Jiao and Moan (1990). Jiao (1992) also proposes an approach using a binomial expansion, but the resulting integrals converge only for integer values of the slope m. The zero-crossing period associated with these stress ranges is obtained using Eq. 20 of Jiao (1992), which may be written as:

$$T_{Z_{LF+WF}} = \frac{T_{Z_{LF}}}{\lambda_{LF}\sqrt{1+\frac{1-\lambda_{LF}}{\lambda_{LF}}\left(\frac{T_{Z_{LF}}}{T_{Z_{WF}}}\,\delta_{WF}\right)^2}} \tag{3-14}$$

where

$$\lambda_{LF} = \frac{\sigma^2_{rms LF}}{\sigma^2_{rms LF}+\sigma^2_{rms WF}} \tag{3-15}$$

is the ratio of the low-frequency variance to the total stress variance. Note that equation 3-14 depends on the bandwidth of the wave-frequency stress but not on the bandwidth of the low-frequency stress.

Thus, by considering separate contributions to damage from two kinds of stress ranges, the equation for the total damage becomes

$$D = e^{-A} \sum_{\substack{i \\ \text{(all seastates)}}} \left\{ \frac{E_i[S^m]_{WF}}{T_{Z_{WF,i}}} + \frac{E_i[S^m]_{LF+WF}}{T_{Z_{LF+WF,i}}} \right\} \left(Tp_i \right) \qquad (3\text{-}16)$$

From a reliability standpoint, we can view the total damage D as a function of the uncertain quantities that affect the stress-range calculations and of the uncertain parameters of the fatigue law, to be described below. The associated limit-state function for the reliability calculations may be written as

$$g(\text{Uncertain Quantities}) = -\ln\{D(\text{Uncertain Quantities})\} \qquad (3\text{-}17)$$

Note that g is negative if the total damage D is greater than unity, signifying fatigue failure.

Uncertainty in the calculated stress ranges arises from uncertainty in the calculation of global response given the sea state, in the calculation of riser stresses given the sea state and global response, and in the stress-amplification factor.

There is also uncertainty in the parameters A and m of Miner's Law, even though the latter uncertainty is often neglected. In addition, fatigue test data (in the form of ln N vs. ln S) show significant scatter, which is represented by a random quantity Δ.

Typically, epistemic and aleatory uncertainty in the metocean model are neglected because the dominant sea states are relatively common. This study will neglect these uncertainties, although results for locations near the top of the riser will show that rare hurricanes contribute significant to fatigue damage at these locations.

Table 3-10 Lists the uncertain quantities considered in this study. Most of these values come from Section 2. A number of the values are location-dependent and are contained in Table 3-11 (based on Table 3-9). Note that we perform two separate analyses for location 5, as follows: 5B applies to the connectors (DNV B) and 5X applies to the welds (API X). Table 3-12 shows the parameters for the three kinds of fatigue curves considered.

Table 3-10. Uncertain Quantities Considered in the Fatigue Reliability Analysis

Var. No.	Description	Bias	COV
1	Deviation from calculated mean force on vessel (multiplicative)	1	0.2
2	Deviation from calculated slow-drift rms vessel offset (multiplicative)	0.95	0.3
3	Deviation from calculated vessel RAO (multiplicative)	1	0.05
4	Deviation from stresses calculated by TIARA (given inputs; multiplicative)	1	0.1 (bottom) 0.2(surface)

Var. No.	Description	mean	σ
5	Cd in wave zone (<500)	1.2	0.36
6	Cd deep (>500)	0.7	0.21
7	S/N ln(Intercept) (A)	var.[1]	var.[1]
8	S/N Slope (m)	var.[1]	0
9	Δ (Miner's Law uncertainty)	0	0.3 [2]
10	Stress Amplification Factor	var.[1]	var.[1]

[1] Value is location-dependent

[2] Typical value (e.g., Wirsching et al., 1984)

Table 3-11 Properties of Locations Considered in Fatigue Analysis

Location	Elev. (ft)	S/N	SAF	
			mean	COV
1	10	B	1.3	0.15
2	47	B	1.1	0.05
3	56	B	3.16	0.1
10	3220	X'	1.0	0.2
5B	3293	B	1.6	0.1
5X	3293	X	1.0	0.1
6	3301	B	1.1	0.05
8	3324	B	1.1	0.05

Table 3-12 Parameters of Fatigue Model

Model	Applicability	A [ln(ksi)]		m (slope) [1]
		mean [1]	σ [2]	
DNV B	Connectors (parent material)	27.66	0.42	4
API X	Welds (higher quality)	28.12	0.97	4.38
API X'	Welds (lower quality, middle portion of riser)	25.51	0.97	3.74

[1] Design values for A (or for K=exp(A)) were provided by Chuck Miller and converted to unbiased values assuming that design value corresponds to a 97.5 percentile.

[2] Values for DNV B and API X taken from Gran (1992). Value for API X' assumed equal to value for API X.

3.6 RESULTS

Reliability calculations for fatigue were performed for selected locations using the RELACS software and a problem-specific limit-state function written for this project. In addition, portions of the limit-state function code were modified into a stand-alone program to generate graphs showing contributions to damage as a functions of Hs and Tp (or wind speed and Tp).

Table 3-13 shows the calculated failure probabilities for all sites considered, as well as the percentage of the damage associated with the low-frequency and wave-frequency motions. Locations at the bottom have the highest failure probabilities, particularly location 3, which has a high stress amplification factor[8]. With the exception of location 10, which is near the mean water level and has lower-grade welds, locations near the top have failure probabilities lower than 10^{-10}. Wave-frequency stresses contribute 59 to 65% of the damage for locations near the bottom and 87 to 97% for locations at the bottom.

Table 3-13 Fatigue Failure Probabilities (exposure: 15 years)

Location	Elev. (ft)	Fatigue Model	Failure Prob.	β	% Low Freq. Damage	% Wave Freq. Damage
1	10	B	1.3E-08	5.57	41	59
2	47	B	3.4E-12	6.86	35	65
3	56	B	6.4E-04	3.22	37	63
10	3220	X'	2.3E-07	5.04	6	94
5B	3293	B	3.2E-11	6.53	13	87
5X	3293	X	6.2E-10	6.08	13	87
6	3301	B	3.5E-14	7.49	12	88
8	3324	B	4.2E-19	8.86	3	97

Tables 3-14 through 3-20 show the values of the uncertain quantities (see Table 3-10) at the design point (combination of parameters with the highest contribution to the failure probability), the corresponding values in standard-normal (U) space, and the associated direction cosines (α). At locations near the bottom of the riser, the most important uncertainties, as measured by the importance factor α^2, are those associated with the TIARA stress calculations, the intercept A of the fatigue law, and the stress amplification factor. The Cd at depths greater than 500 feet[9] and the scatter in Miner's Law are also important contributors. At locations near the top of the riser,

---

[8] There are a number of conservative assumptions in our analysis of Location 3, such as the assumption that all weather comes from the same direction, the calculation of the stress-amplification factor at this site, and the fatigue curves used. Thus, a more realistic estimate of the failure probability of Location 3 is likely to be significantly lower than the value obtained here.

[9] The value used here for the Cd at depths greater than 500 feet, which is the same value used in Section 2, may not be appropriate because the associated Reynold numbers are lower for the low seastates of interest in fatigue analysis.

the most important uncertainty is that associated with the TIARA stress calculations. Recall our assumption that the deviations of the true stress from the calculated stress has a COV of 20% near the top and 10% near the bottom. Also important are the Miner-Law intercept, the Miner-Law scatter, and the stress amplification factor. The relative importance of these three vary from site to site, as a result of the differences in fatigue model and uncertainty in stress amplification between welds and connectors.

Figures 3-15 through 3-19 show the contributions of various Hs-Tp ranges to the damage associated with low-frequency and wave-frequency motions, as well as to the total damage, when all uncertain quantities are set to their design-point values. Results are shown as surfaces and as contours (with a contour interval of 0.05). At locations near the bottom of the riser, the contribution from low-frequency motions is noticeable (on the order of 30%, as we saw earlier). The peak of this contribution occurs at higher Hs values than the peak of the Hs distribution, as a result of the quadratic dependence of low-frequency motions on Hs and Vw. The peak contribution from wave-frequency motions at locations near the bottom and at location 10 occurs at Tp ~ 6 sec, largely as a result of the Tp-dependent term $\psi(T_p)$ introduced in Section 3.4.2 (see Figure 3-12). For locations 5, 6, and 8 (above the wave zone), $\psi(T_p)$ is much flatter. As a result, this pronounced peak near 6 sec does not occur.

An interesting side effect of the shape of $\psi(T_p)$ for Locations 5, 6, and 8 is that the contribution to damage from high sea states (in the 100-yr hurricane regime) becomes more important, at least in a relative sense. In an absolute sense, however, this contribution is still small because the fatigue-failure probability for these Locations is very low. Two points are worth noting about the fatigue associated with these high sea states. First, the rate of those sea states is probably under-estimated by our metocean model, because the rate we use is simply an extrapolation of our fit to the GLOW results and does not consider hurricane occurrence rates explicitly. Second, if these rare sea states became important in the analysis of a fatigue-sensitive location, it would be necessary to consider the Type-I uncertainty associated with hurricane occurrences. The assumption that each sea state will occur with a rate equal to its long-term rate during the riser's 15-year life is not appropriate for these rare sea states.

In Appendix A, we show how the results obtained here may be expressed in terms of the simplified fatigue reliability model of Wirsching (1984). Results from Appendix A indicate that the Type-II uncertainties in the metocean model, global-response calculation, and stress calculations, are equivalent to a COV of 22% in the stress range. This result is applicable to all locations and materials considered in this section.

3.7 SUMMARY AND CONCLUSIONS

This section demonstrated the fatigue reliability analysis for a top-tensioned riser. As was the case in the extreme-load calculations, the highest failure probabilities occur near the bottom of the riser. Unlike the extreme-load calculations, the wave-frequency stresses are much more important than the low-frequency motions. Also, the wave-frequency stresses show a strong dependence on Tp, which arise from the vessel RAO and from the dynamics of the riser. These dynamics issues will become even more important in the fatigue analysis of a steel catenary or lazy wave riser.

Locations near the top of the riser show much lower failure probabilities. The actual failure probabilities at these locations are higher than the calculated values, because hurricanes are not included explicitly and because their aleatory uncertainty is neglected. In spite of these factors, the actual failure probabilities are believed to be acceptably low.

The relative importance of the various uncertain quantities differ as a function of locations (top vs. bottom), connector vs. weld, and uncertainty in the stress amplification factor. In general, the most important contributors to uncertainty are the uncertainty in the calculated stresses (particularly at the top), uncertainty in the fatigue-law intercept, and uncertainty in the stress amplification factor, and scatter in the fatigue data.

Table 3-14 Design Point Associated with Fatigue Failure: Location 1

No.	Description	Value	U	α (direction cosine)		
1	Δ in mean force	0.975	-0.027	0.005		
2	Δ in slow-drift rms offset	1.350	1.360	-0.240	▮▮▮	
3	Δ in WF RAO	1.040	0.902	-0.160	▮▮	
4	Δ in TIARA Stresses	1.250	2.260	-0.400	▮▮▮▮▮▮	
5	Cd (wave zone)	1.150	0.000	0.000		
6	Cd (deep)	0.366	-2.060	0.365		▮▮▮▮▮
7	S/N: ln [Intercept]	26.700	-2.380	0.422		▮▮▮▮▮▮
8	S/N: Slope	4.000	0.000	0.000		
9	S/N: Delta	1.560	1.660	-0.295	▮▮▮▮	
10	Stress Amplif. Factr.	2.130	3.380	-0.599	▮▮▮▮▮▮▮▮	

Table 3-15 Design Point Associated with Fatigue Failure: Location 3

No.	Description	Value	U	α (direction cosine)		
1	Δ in mean force	0.978	-0.016	0.005		
2	Δ in slow-drift rms offset	1.120	0.694	-0.211	▮▮▮	
3	Δ in WF RAO	1.030	0.599	-0.182	▮▮	
4	Δ in TIARA Stresses	1.150	1.430	-0.436	▮▮▮▮▮▮	
5	Cd (wave zone)	1.150	0.000	0.000		
6	Cd (deep)	0.423	-1.570	0.479		▮▮▮▮▮▮▮
7	S/N: ln [Intercept]	27.000	-1.510	0.459		▮▮▮▮▮▮
8	S/N: Slope	4.000	0.000	0.000		
9	S/N: Delta	1.300	1.050	-0.321	▮▮▮▮	
10	Stress Amplif. Factr.	3.630	1.430	-0.436	▮▮▮▮▮▮	

Table 3-16 Design Point Associated with Fatigue Failure: Location 10

No.	Description	Value	U	α (direction cosine)		
1	Δ in mean force	0.981	0.000	0.000		
2	Δ in slow-drift rms offset	0.931	0.079	-0.016		
3	Δ in WF RAO	1.030	0.570	-0.113	▮	
4	Δ in TIARA Stresses	1.620	2.550	-0.504	▮▮▮▮▮▮▮	
5	Cd (wave zone)	1.270	0.346	-0.068	▮	
6	Cd (deep)	0.663	-0.038	0.008		
7	S/N: ln [Intercept]	22.300	-3.330	0.660		▮▮▮▮▮▮▮▮▮
8	S/N: Slope	3.740	0.000	0.000		
9	S/N: Delta	1.290	1.010	-0.200	▮▮▮	
10	Stress Amplif. Factr.	1.620	2.550	-0.504	▮▮▮▮▮▮▮	

Table 3-17 Design Point Associated with Fatigue Failure: Location 5 (DNV B)

No.	Description	Value	U	α (direction cosine)		
1	Δ in mean force	0.987	0.033	-0.005		
2	Δ in slow-drift rms offset	1.010	0.347	-0.053		
3	Δ in WF RAO	1.060	1.200	-0.183	▮▮	
4	Δ in TIARA Stresses	2.620	4.970	-0.758	▮▮▮▮▮▮▮▮▮▮▮	
5	Cd (wave zone)	1.150	0.000	0.000		
6	Cd (deep)	0.613	-0.307	0.047		
7	S/N: ln [Intercept]	26.600	-2.630	0.402		▮▮▮▮▮▮
8	S/N: Slope	4.000	0.000	0.000		
9	S/N: Delta	1.640	1.840	-0.281	▮▮▮▮	
10	Stress Amplif. Factr.	2.040	2.500	-0.382	▮▮▮▮▮	

Table 3-18 Design Point Associated with Fatigue Failure: Location 5 (API X)

No.	Description	Value	U	α (direction cosine)		
1	Δ in mean force	0.985	0.023	-0.004		
2	Δ in slow-drift rms offset	0.980	0.252	-0.041		
3	Δ in WF RAO	1.040	0.895	-0.147	▮▮	
4	Δ in TIARA Stresses	2.050	3.710	-0.610	▮▮▮▮▮▮▮▮▮	
5	Cd (wave zone)	1.150	0.000	0.000		
6	Cd (deep)	0.627	-0.230	0.038		
7	S/N: ln [Intercept]	24.100	-4.150	0.682		▮▮▮▮▮▮▮▮▮▮
8	S/N: Slope	4.380	0.000	0.000		
9	S/N: Delta	1.390	1.260	-0.207	▮▮▮	
10	Stress Amplif. Factr.	1.200	1.870	-0.307	▮▮▮▮	

Table 3-19 Design Point Associated with Fatigue Failure: Location 6

No.	Description	Value	U	α (direction cosine)		
1	Δ in mean force	0.990	0.048	-0.006		
2	Δ in slow-drift rms offset	1.020	0.396	-0.053		
3	Δ in WF RAO	1.070	1.460	-0.194	▮▮	
4	Δ in TIARA Stresses	3.240	6.030	-0.804	▮▮▮▮▮▮▮▮▮▮▮▮	
5	Cd (wave zone)	1.150	0.000	0.000		
6	Cd (deep)	0.606	-0.342	0.046		
7	S/N: ln [Intercept]	26.300	-3.200	0.426		▮▮▮▮▮▮
8	S/N: Slope	4.000	0.000	0.000		
9	S/N: Delta	1.850	2.230	-0.298	▮▮▮▮	
10	Stress Amplif. Factr.	1.190	1.520	-0.203	▮▮▮	

Table 3-20 Design Point Associated with Fatigue Failure: Location 8

No.	Description	Value	U	α (direction cosine)		
1	Δ in mean force	0.980	-0.005	0.001		
2	Δ in slow-drift rms offset	0.940	0.112	-0.013		
3	Δ in WF RAO	1.090	1.780	-0.201	▮▮▮	
4	Δ in TIARA Stresses	4.020	7.120	-0.804	▮▮▮▮▮▮▮▮▮▮▮▮	
5	Cd (wave zone)	1.160	0.017	-0.002		
6	Cd (deep)	0.720	0.242	-0.027		
7	S/N: ln [Intercept]	26.100	-3.780	0.426		▮▮▮▮▮▮
8	S/N: Slope	4.000	0.000	0.000		
9	S/N: Delta	2.080	2.640	-0.298	▮▮▮▮	
10	Stress Amplif. Factr.	1.200	1.800	-0.203	▮▮▮	

Location 1 - Distribution of Damage from Low-Frequency Motions

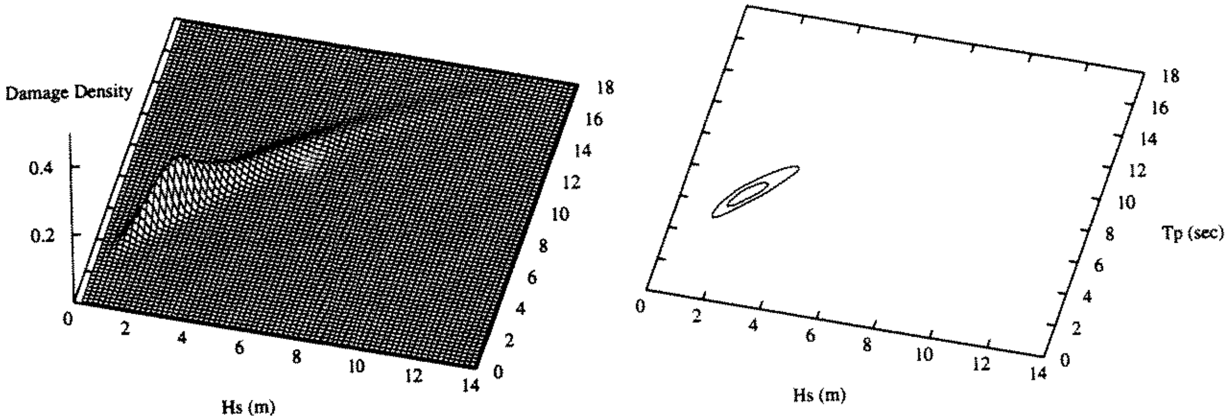

Location 1 - Distribution of Damage from Wave-Frequency Motions

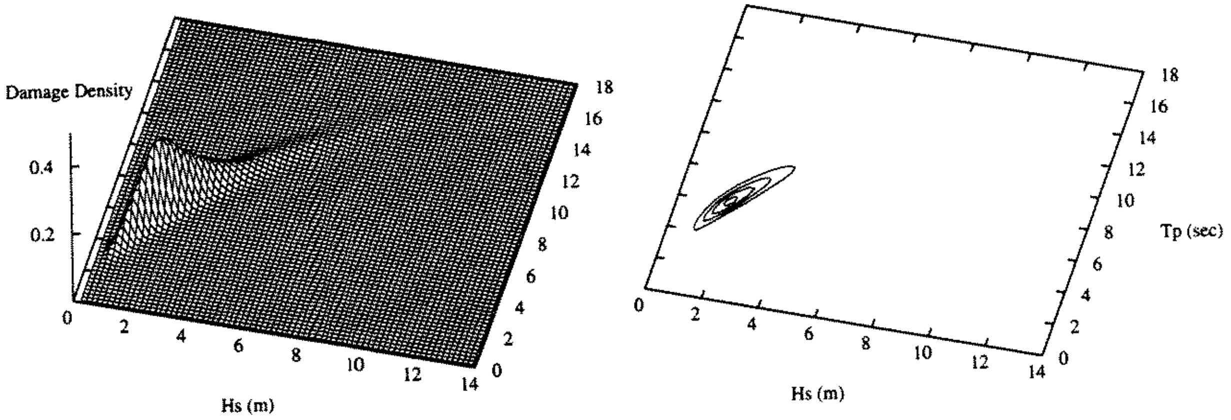

Location 1 - Distribution of Total Damage

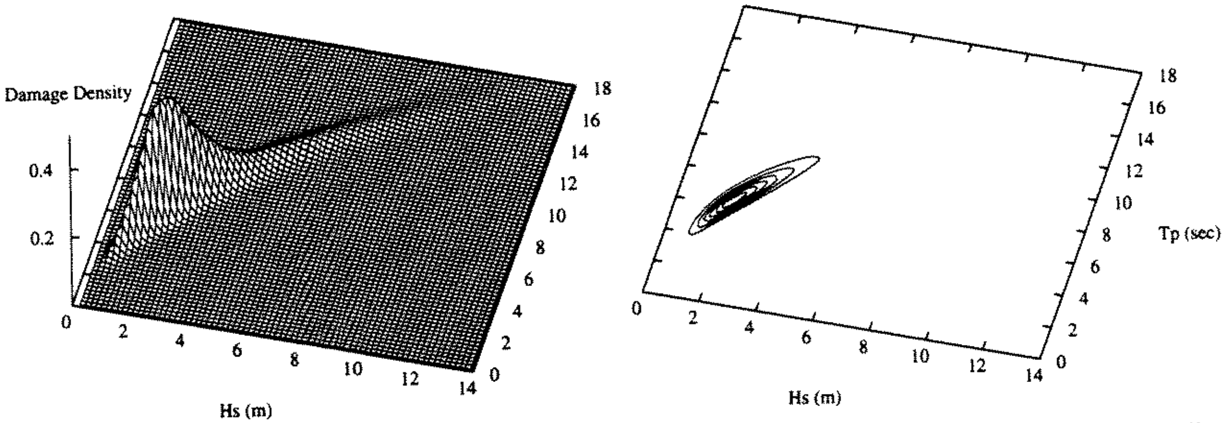

Figure 3-15. Contributions of various Hs-Tp combinations to total damage for Location 1. All uncertain quantities are set to their design-point values.

Location 3 - Distribution of Damage from Low-Frequency Motions

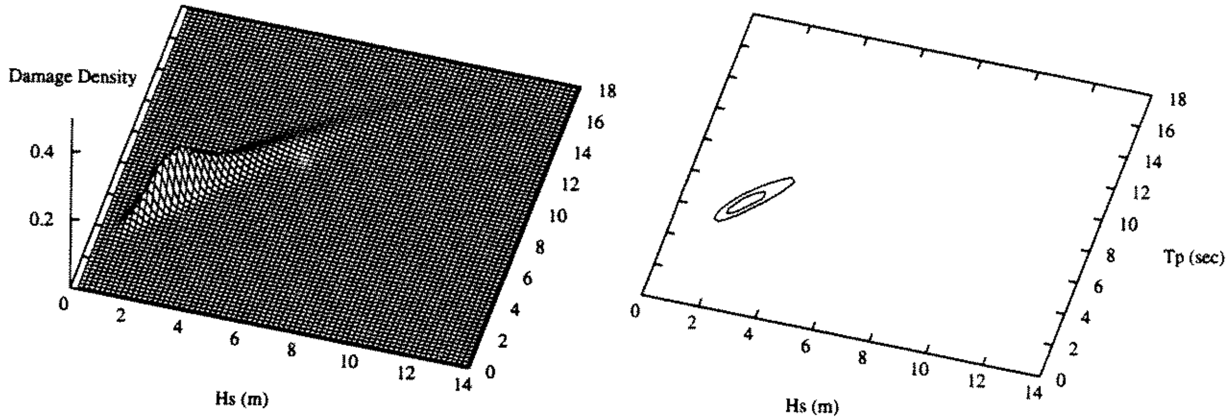

Location 3 - Distribution of Damage from Wave-Frequency Motions

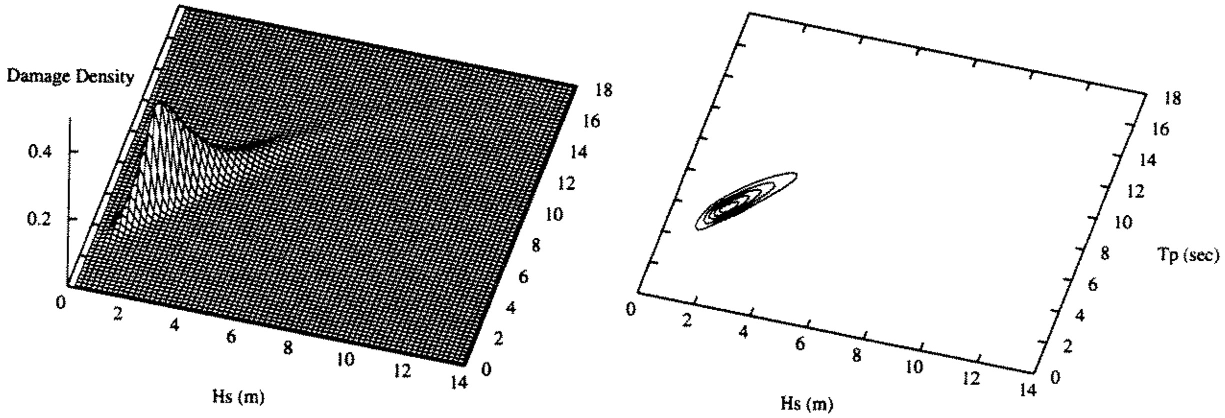

Location 3 - Distribution of Total Damage

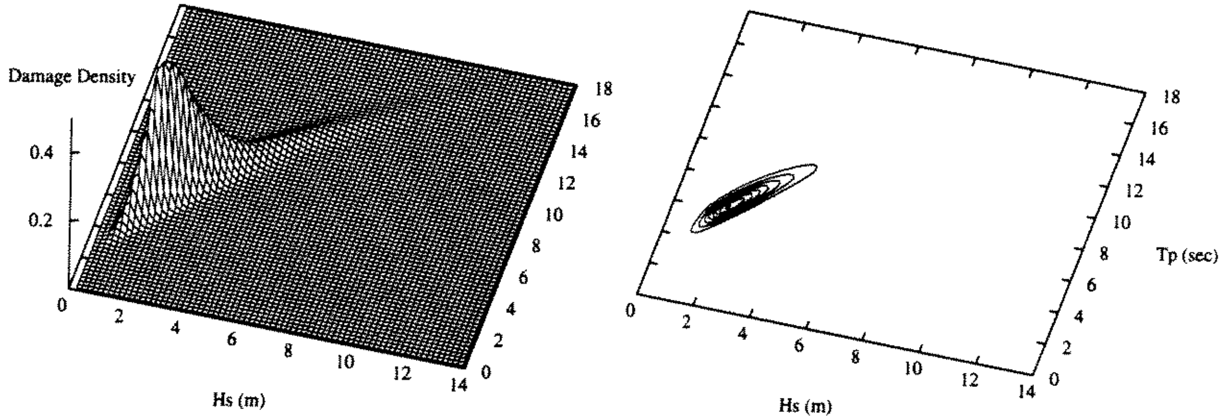

Figure 3-16. Contributions of various Hs-Tp combinations to total damage for Location 3. All uncertain quantities are set to their design-point values.

Location 10 - Distribution of Damage from Low-Frequency Motions

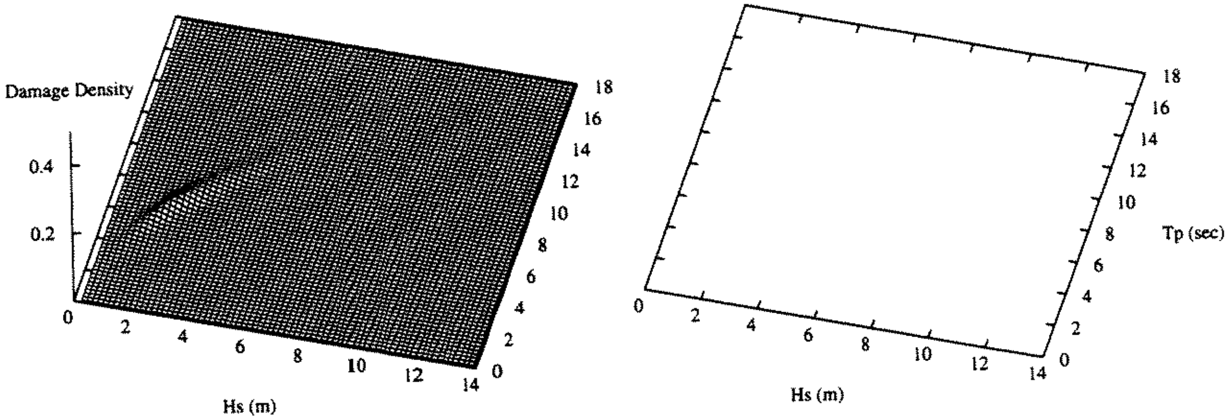

Location 10 - Distribution of Damage from Wave-Frequency Motions

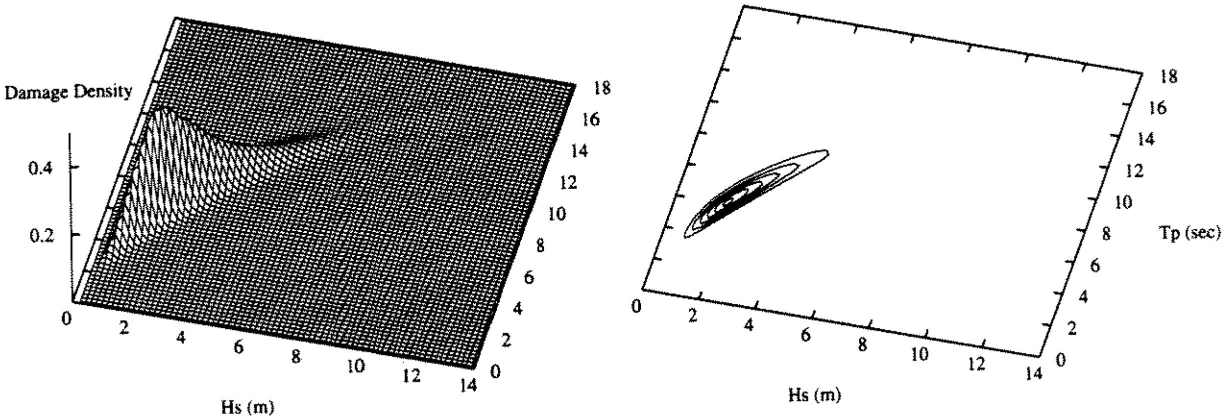

Location 10 - Distribution of Total Damage

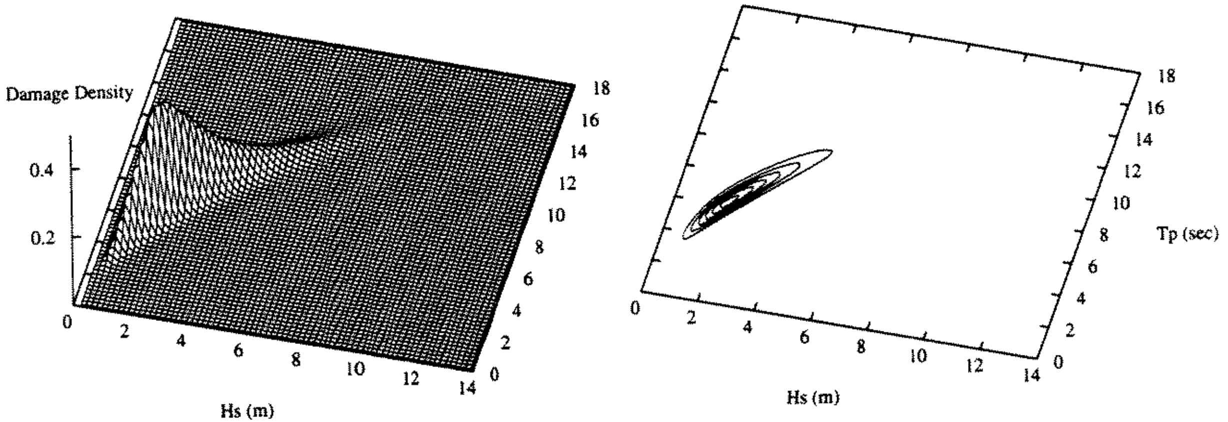

Figure 3-17. Contributions of various Hs-Tp combinations to total damage for Location 10. All uncertain quantities are set to their design-point values.

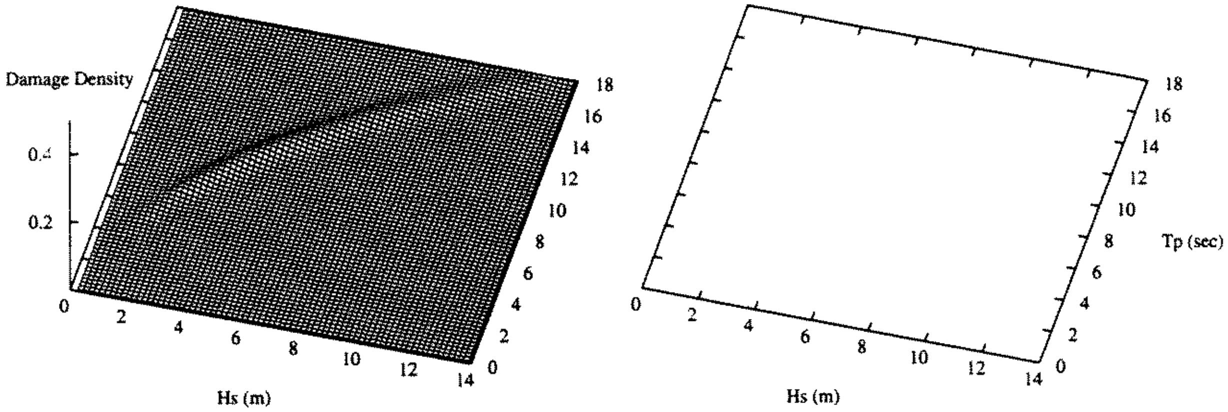

Location 5X - Distribution of Damage from Low-Frequency Motions

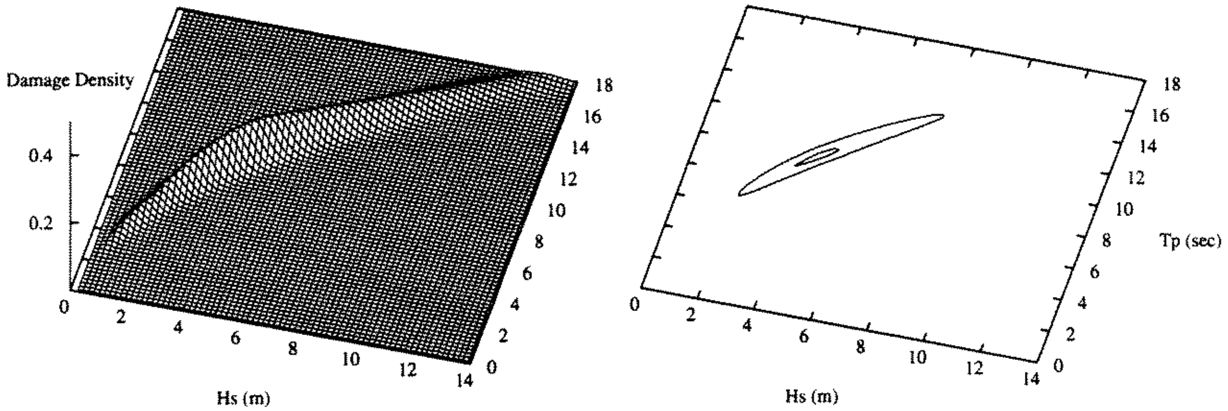

Location 5X - Distribution of Damage from Wave-Frequency Motions

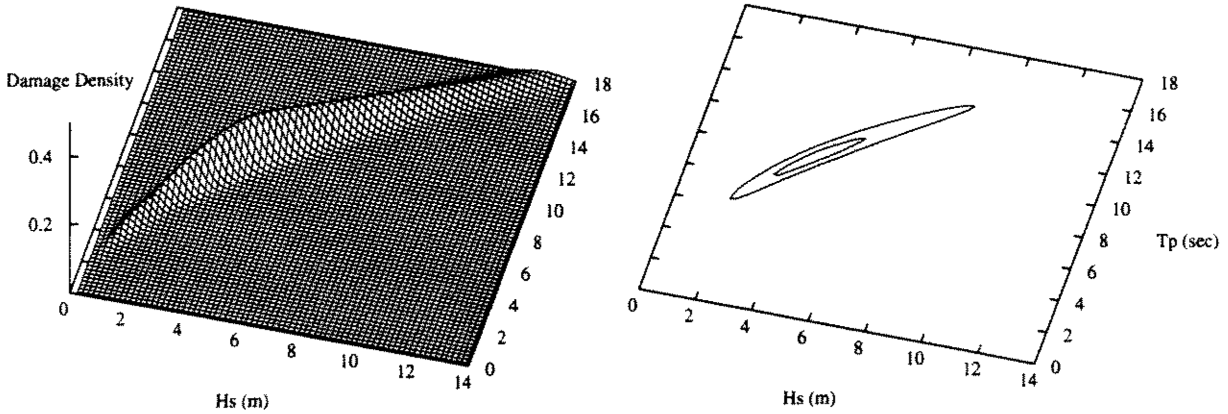

Location 5X - Distribution of Total Damage

Figure 3-18. Contributions of various Hs-Tp combinations to total damage for Location 5 (API X weld). All uncertain quantities are set to their design-point values.

Location 6 - Distribution of Damage from Low-Frequency Motions

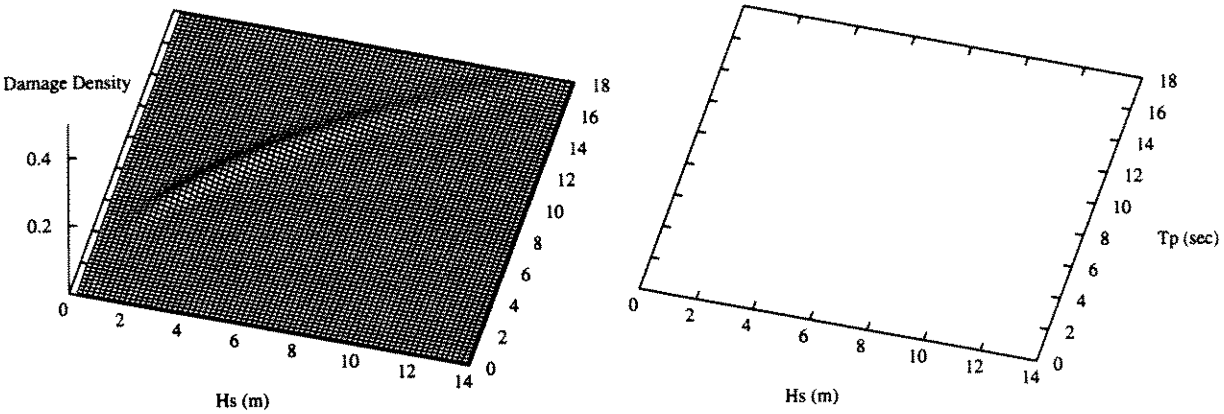

Location 6 - Distribution of Damage from Wave-Frequency Motions

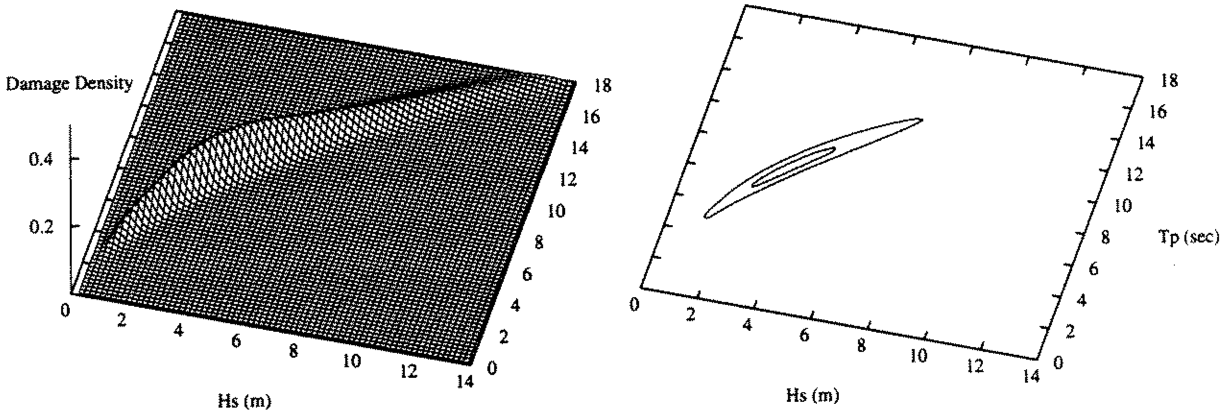

Location 6 - Distribution of Damage from Total Damage

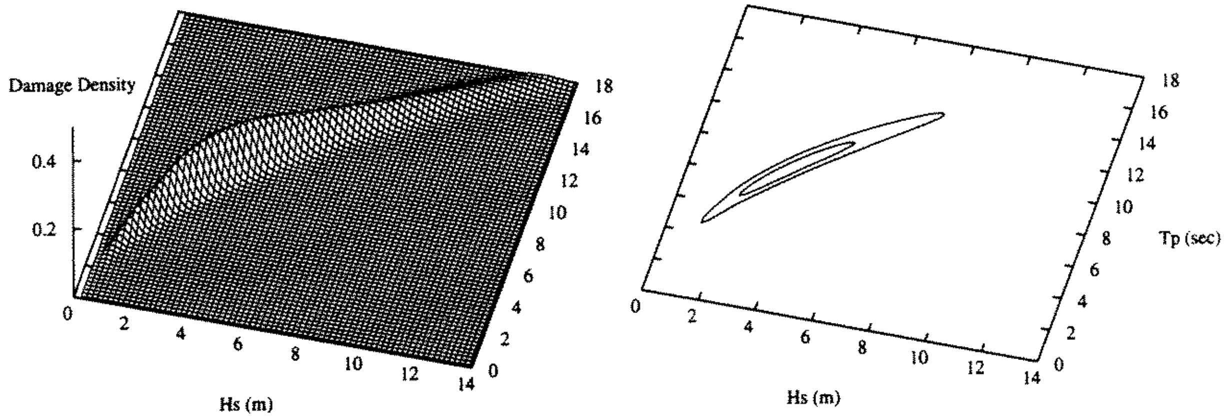

Figure 3-19. Contributions of various Hs-Tp combinations to total damage for Location 6. All uncertain quantities are set to their design-point values.

4. Analysis of Fatigue under Vortex-Induced Vibration

4.1 INTRODUCTION

The inputs to the probabilistic analysis of fatigue from vortex-induced vibration (VIV) for a top-tensioned riser fall in the same general categories as the inputs for the analysis of extreme loads. These inputs consist of a probabilistic characterization of the intensity and frequency of occurrence of loop-current events and for the current profile, models for the calculation of VIV motions of the riser and the resulting stresses in the riser, and limit-state models that define the occurrence of failure (i.e., fatigue curves). All these inputs are then used to construct a reliability model, which is used to calculate the probability of failure due to wave effects and vessel motions during the riser 15-year life.

4.2 LOOP CURRENT MODEL

The model for loop current used in design checks for long-term fatigue from VIV consists of a histogram of current velocity and a normalized current profile. Thus, it is assumed that the profile shape does not depend on the current velocity and does not vary from one loop-current event to the next. In fact, this analysis does not concern.

Table 4-1 and Figure 4-1 show the histogram of current velocity used in this study, which comes from a location 20 miles south of the Marlin site. Note that the highest is associated with only one day of exposure. This indicates that there is significant Type-II uncertainty about the true long-term rate (over hundreds of years) associated with this and other high bins, as well as Type-I uncertainty about the rate that will be experienced during the 15- to 20-year life of the riser system. Accurate characterization of these uncertainties requires information that was not available to this study, including the duration of the data set used and the number of loop-current events in the data set. In lieu of this information, these uncertainties will be quantified on the basis of judgment (see Section 4.5).

In addition to these uncertainties, there is a strong site-to-site variation in the intensity of loop currents within the Gulf. This variation, which may account for 30 to 50% differences in rates, is not considered here (i.e., this study considers an individual site in the vicinity of Marlin site).

This study considered three alternative normalized profiles, which are shown in Table 4-2 and Figure 4-2. These three profiles were drawn from past projects and correspond to different sites. Generally, profiles for VIV are obtained by averaging measurements over time. As a result, these profiles are smoother than instantaneous profiles. Smooth profiles produce higher VIV, thus introducing conservatism in the VIV calculations. Although these profiles differ significantly at depth, they differ little in the thickness of the flat, higher-velocity portion of the profile (corresponding to the mixed-layer). This thickness may be the most important characteristic of the profile for the purposes of VIV.

Table 4-21 Histogram of Current Velocity for VIV Analysis

Total and Per-Year Statistics for Eddy Surface Currents 20 miles South of Marlin

Surface Curr. Speed (ft/sec)	Total Days of Occurrence during 21 years	Days/Year	% of Year
0.16	62	2.95	0.81
0.49	181	8.62	2.36
0.82	200	9.52	2.61
1.15	91	4.33	1.19
1.47	38	1.81	0.50
1.80	14	0.67	0.18
2.13	12	0.57	0.16
2.46	8	0.38	0.10
2.79	10	0.48	0.13
3.12	6	0.29	0.08
3.44	7	0.33	0.09
3.77	3	0.14	0.04
4.10	10	0.48	0.13
4.43	1	0.05	0.01
Totals	643	30.62	8.39

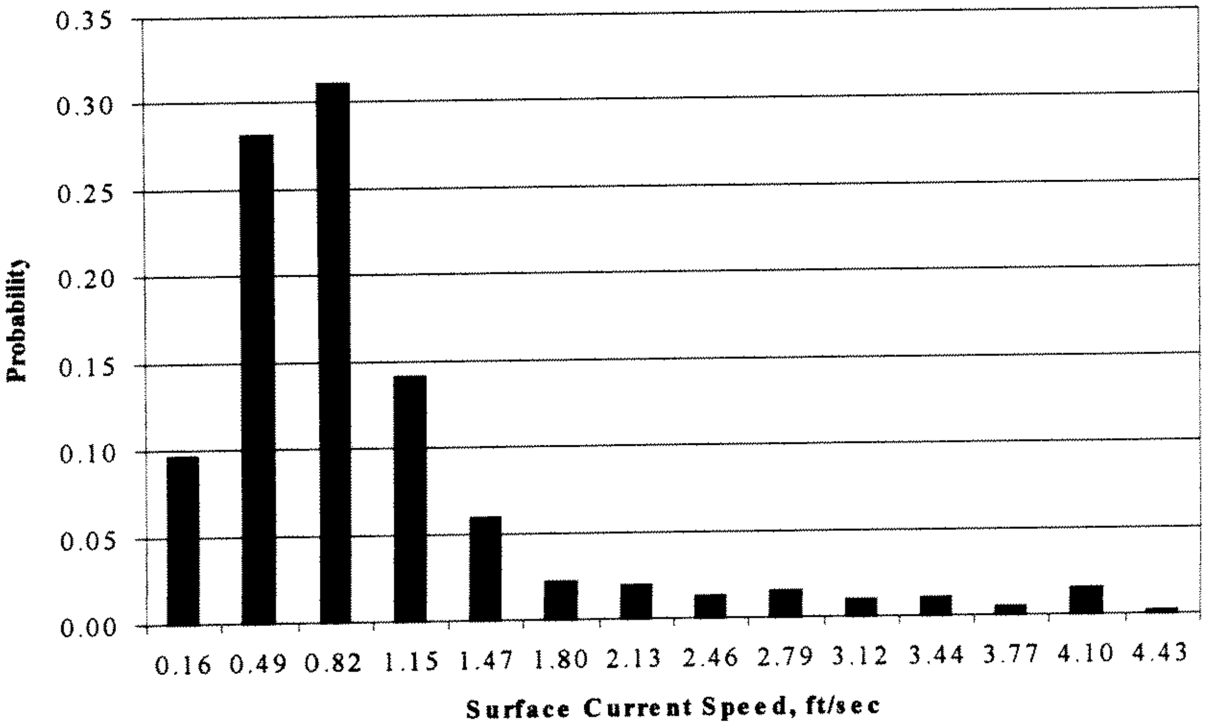

Figure 4-20. Current-velocity histogram (during the 8.4% of time when loop currents are active).

Table 4-22. Normalized Current Profiles

Mobil Profile		DEEPSTAR Profile		Marlin Profile	
Elevation (ft)	Normalized Profile	Elevation (ft)	Normalized Profile	Elevation (ft)	Normalized Profile
3240	1.00	3240	1.00	3240	1.00
3160	1.00	2940	0.93	2940	0.89
2910	1.00	2740	0.38	2740	0.72
2830	0.82	2240	0.35	2240	0.57
2748	0.66	1740	0.13	1740	0.24
2665	0.52	1240	0.05	1240	0.07
2580	0.42	0	0.05	1239	0.00
2500	0.32			0	0.00
2420	0.26				
2340	0.19				
2260	0.14				
2175	0.10				
2125	0.08				
2010	0.06				
1930	0.04				
1850	0.03				
1765	0.02				
1680	0.01				
1600	0.01				
0	0.00				

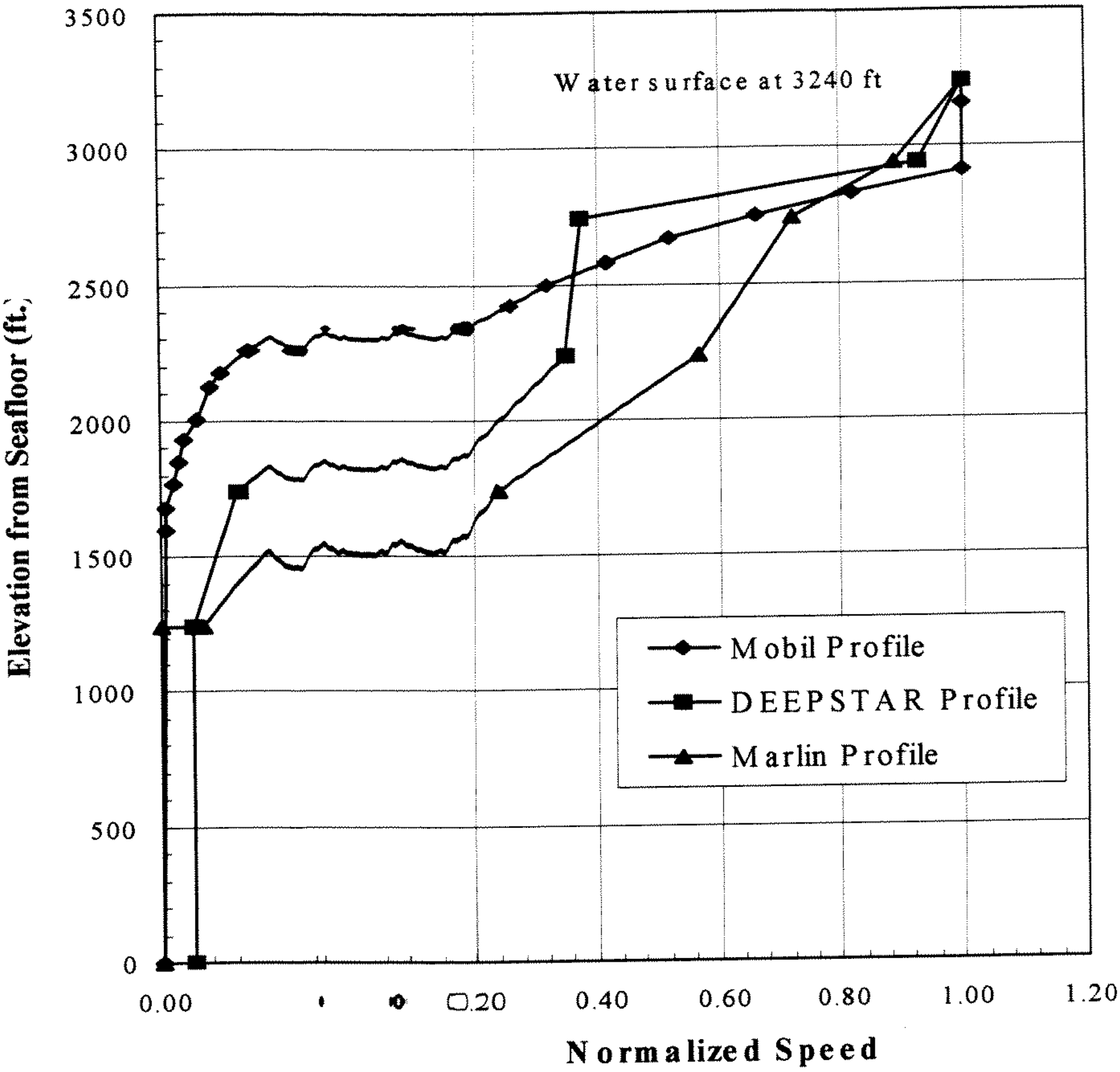

Figure 4-21. Normalized current profile

4.3 VIV AND RISER-RESPONSE CALCULATIONS

The VIV fatigue damage estimates were obtained using the loop current profiles and current histograms given in Section 4.2.

The calculation of the VIV fatigue damage assumed single mode riser response (i.e. assuming that the current will excite the riser at only one of the riser's natural periods) and was performed using TIARA . TIARA incorporates version 1.0 of the VIV analysis program SHEAR7 as one of its analysis modules.

The TIARA VIV solutions are performed using the same riser models used for the design storm load cases and fatigue bin analyses. The steps performed by TIARA for a VIV analysis are outlined below:

1. The riser natural periods and mode shapes are calculated. The number of natural periods and modes shapes determined is equal to 1/8 of the number of elements used in the TIARA riser model.
2. A SHEAR7 element mesh is generated. The number of SHEAR7 elements is equal to 4 times the number of elements used in the TIARA riser model, and the SHEAR7 elements are all the same length.
3. The mode shapes generated by TIARA are mapped onto the SHEAR7 element mesh.
4. Other SHEAR7 input parameters are calculated and a SHEAR7 solution is generated. The input parameters are automatically selected by TIARA to force SHEAR7 to perform its analysis assuming a single mode response.
5. The SHEAR7 results (rms stresses along the length of the riser) are mapped back onto the TIARA element mesh.

A consequence of the assumption of single-mode response is that the dominant frequency for a given velocity bin-profile combination is the same for all locations in the riser. In general, this is not the case if multi-mode response is considered.

Summaries of these results are presented in Figures 4-3 through 4-5 and discussed below. Most results are presented in terms of what we loosely call Damage, which is defined as

$$Damage = \sum_{\substack{i \\ \text{(all current-speed bins)}}} (rms\ stress_i)^4 \left(\frac{p_i}{T_{Z_i}} \right) \tag{4-18}$$

where p_i is the fraction of time associated with bin i and T_{Z_i} is the associated zero-crossing period. This quantity is not exactly identical to damage because it does not have the proper units and because the exponent of four is not applicable to all locations in the riser. Figure 4-3 shows the distribution of total damage (all velocity bins) as a function of depth for all velocity profiles. The highest damage occurs near the top and bottom of the riser. Figure 4-4 shows zooms on the top

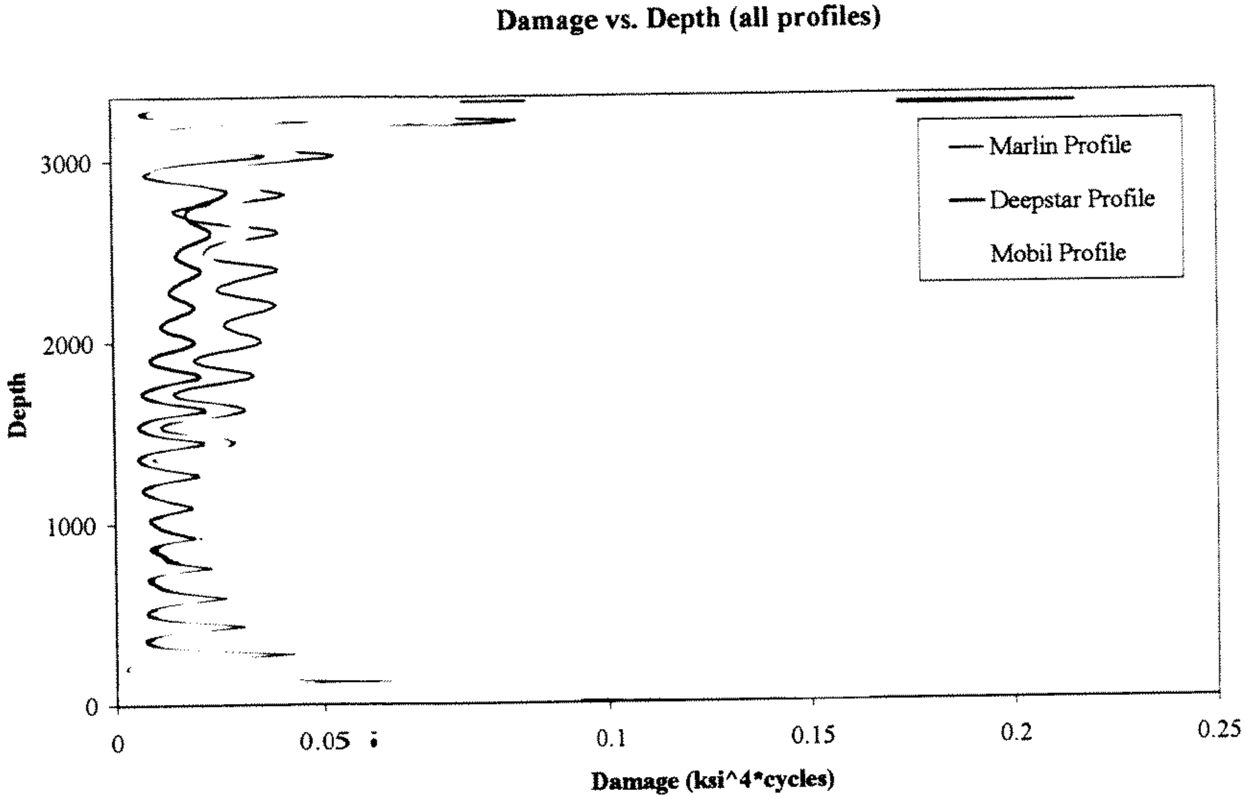

Figure 4-22. Distribution of damage as a function of depth for all velocity profiles.

and bottom of the riser. This figure indicates that the stress distribution at the top and bottom of the riser is strongly dependent on the mechanical properties (longitudinal variations of mass and stiffness) and on the boundary conditions.

Figure 4-5 shows the contributions of the higher current bins to the total damage as a function of depth, as calculated using the Marlin velocity profile. The higher bins are important contributors to the total damage for locations near the top of the riser, but not for locations near the bottom. Tables 4-3 and 4-4 show that the same observation is valid for all velocity profiles. Bins 11 through 14 (current speeds of 3.4 fps and higher) contribute nearly 100% of the damage for locations near the top (as well as location 4). In contrast, nearly all bins contribute (including bins 1 through 5) contribute to the damage at locations 1 through 3.

These calculations were performed assuming no vessel offset as a result of the current itself or of wind and current that may be present during the loop-current events. This assumption is conservative because the increased tension caused by vessel offset reduces the amplitude of VIV. The amount of conservatism introduced by this assumption is not quantified here but can be quantified using the metocean data from Chapter 3, together with additional TIARA runs. It is estimated that normal winds introduce a 10% increase in riser tension, which translates into a 10-20% increase in fatigue life.

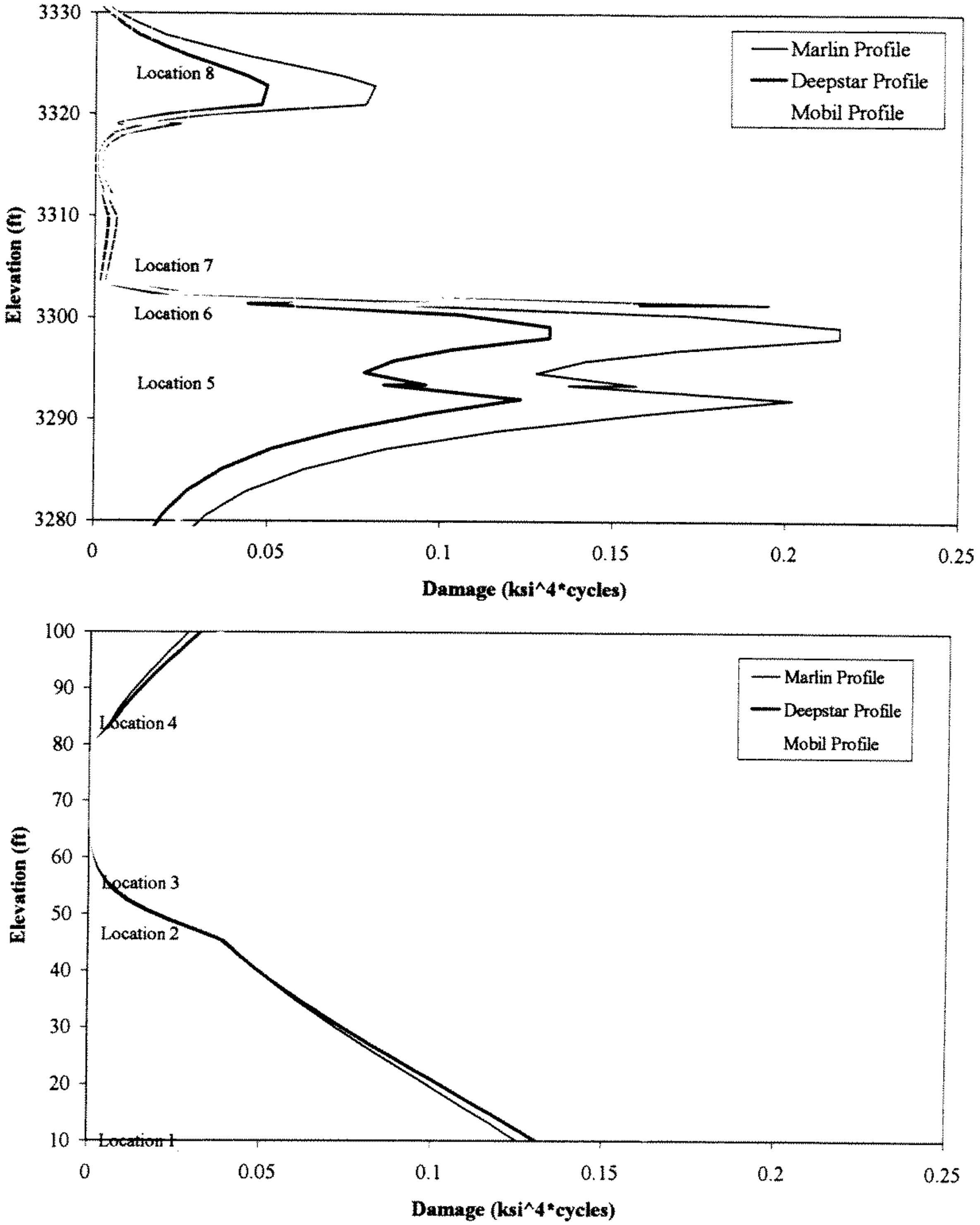

Figure 4-23. Distribution of damage as a function of depth near the top and bottom of the riser, for all velocity profiles:

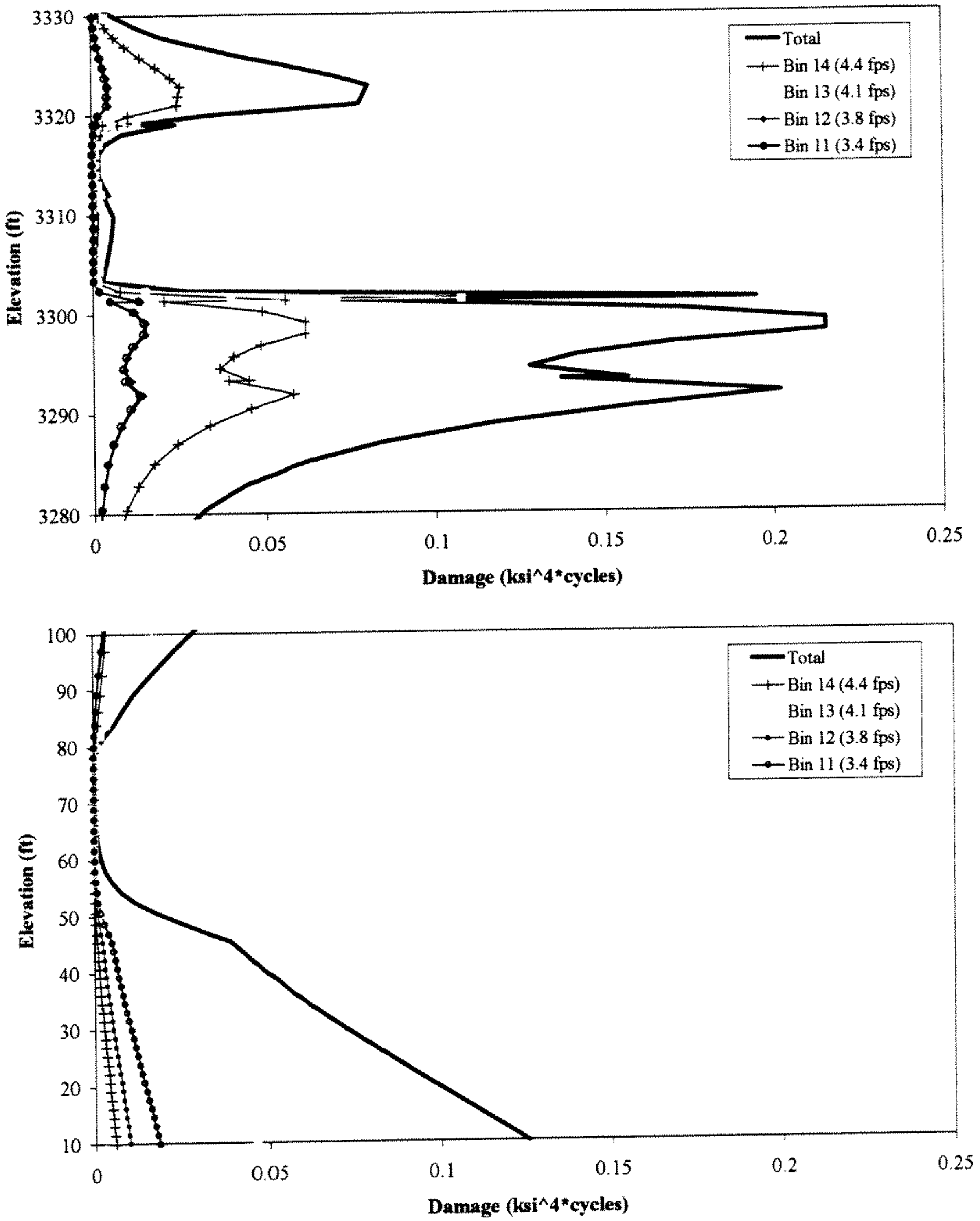

Figure 4-24. Contributions of upper current velocity bins to total damage.

Table 4-23. Contributions of Various Current Bins to Damage (locations near top of riser)

	Bin Number	1 - 5	6	7	8	9	10	11	12	13	14
	Velocity (fps)	0 - 1.475	1.803	2.131	2.459	2.787	3.115	3.443	3.771	4.099	4.427
	Fraction of Time (during loop-current events)	88.95	2.18	1.87	1.24	1.56	0.93	1.09	0.47	1.56	0.16
Location	**Velocity Profile**	**% Damage**									
Loc. 8 (3324' elev.)	Marlin	0.00	0.01	0.02	0.04	0.44	0.79	5.67	6.49	54.30	32.25
	Deepstar	0.00	0.01	0.02	0.12	0.43	0.76	5.21	6.21	56.06	31.19
	Mobil	0.00	0.01	0.02	0.11	0.45	0.81	5.56	6.49	56.42	30.12
Loc. 7 (3305' elev.)	Marlin	0.01	0.02	0.05	0.09	0.75	1.19	6.95	7.23	55.41	28.29
	Deepstar	0.02	0.02	0.05	0.22	0.74	1.16	6.38	6.91	57.25	27.26
	Mobil	0.02	0.02	0.05	0.21	0.77	1.22	6.80	7.18	57.40	26.32
Loc. 6 (3301' elev.)	Marlin	0.01	0.01	0.04	0.08	0.72	1.15	6.86	7.19	55.36	28.57
	Deepstar	0.01	0.01	0.05	0.21	0.70	1.12	6.29	6.87	57.28	27.47
	Mobil	0.01	0.02	0.04	0.20	0.73	1.18	6.71	7.14	57.40	26.56
Max (3299' elev.)	Marlin	0.01	0.01	0.04	0.08	0.71	1.14	6.83	7.18	55.37	28.64
	Deepstar	0.01	0.01	0.04	0.20	0.69	1.10	6.26	6.85	57.27	27.55
	Mobil	0.01	0.01	0.04	0.20	0.72	1.17	6.68	7.13	57.39	26.65
Loc. 5 (3293' elev.)	Marlin	0.01	0.01	0.03	0.07	0.66	1.09	6.71	7.12	55.46	28.84
	Deepstar	0.01	0.01	0.04	0.19	0.65	1.05	6.15	6.80	57.37	27.74
	Mobil	0.01	0.01	0.04	0.18	0.67	1.11	6.57	7.07	57.49	26.84

Table 4-24. Contributions of Various Current Bins to Damage (locations near bottom of riser)

	Bin Number	1 - 5	6	7	8	9	10	11	12	13	14
	Velocity (fps)	0 - 1.475	1.803	2.131	2.459	2.787	3.115	3.443	3.771	4.099	4.427
	Fraction of Time (during loop-current events)	88.95	2.18	1.87	1.24	1.56	0.93	1.09	0.47	1.56	0.16
Location	**Velocity Profile**	**% Damage**									
Loc. 4 (84' elev.)	Marlin	1.25	0.01	0.00	0.00	0.10	0.42	6.44	7.35	62.79	21.63
	Deepstar	0.67	0.01	0.00	0.00	0.09	0.35	5.80	7.29	61.86	23.93
	Mobil	0.84	0.01	0.00	0.00	0.09	0.42	6.84	7.87	61.35	22.56
Loc. 3 (56' elev.)	Marlin	37.50	6.73	8.72	7.99	12.75	7.96	7.55	2.73	7.77	0.30
	Deepstar	31.16	7.10	8.62	9.32	13.19	8.49	8.63	3.41	9.66	0.42
	Mobil	32.55	6.18	8.93	8.66	13.11	9.17	9.14	3.31	8.59	0.36
Loc. 2 (47' elev.)	Marlin	21.07	4.47	6.26	6.28	12.59	9.05	12.25	5.57	20.77	1.70
	Deepstar	16.32	4.33	5.69	7.49	11.97	8.88	12.88	6.42	23.84	2.18
	Mobil	17.29	3.85	6.02	7.10	12.14	9.79	13.94	6.35	21.63	1.88
Loc. 1 (10' elev)	Marlin	8.33	2.18	3.37	3.77	9.65	8.00	14.92	8.15	36.94	4.69
	Deepstar	6.11	1.97	2.85	4.70	8.55	7.31	14.62	8.74	39.51	5.64
	Mobil	6.58	1.80	3.09	4.57	8.90	8.26	16.22	8.86	36.74	4.98

4.4 DEVELOPMENT OF RESPONSE SURFACES FOR RISER STRESSES

In these sections, we develop parametric expressions to calculate the rms stress and zero-crossing frequency as a function of the surface current speed. Because these expressions depend on a single variable, they are considerably more simple than those required in Chapters 2 and 3.

Figure 4-6 shows the rms stress at locations 1 through 8 (see Figure 2-7 for the definition of these locations), for the Marlin velocity profile. Locations near the bottom are shown as heavy lines. The curves for locations 1, 2, and 3 have a negative second derivative, and they flatten or even decrease as the surface current increases. The curves for locations 5 through 8 (near the top of the riser) become steeper with increasing surface current. Location 4 behaves like locations 1-3 for low currents and like locations 5-8 for high currents.

We select locations 1, 5, and 6 for the reliability analysis and fit expressions of the form

$$\sigma_{rms}=C_1\,(V_C-0.162)^{C_2} \qquad (4\text{-}19)$$

to the results obtained using the three current profiles. This functional form works for the three locations selected but does not work for the other (less interesting) locations. The residual standard deviation (corresponding to a COV of 6 to 7%) is interpreted as entirely the result of differences among profiles, although there is also a small contribution from lack of fit (see Figure 4-7). Table 4-4 lists the resulting coefficients.

Table 4-24 Coefficients of Response Surface for VIV Stresses

Location	C_1	C_2	**COV**
1	0.571	0.75	0.07
5	0.033	2.92	0.06
6	0.037	2.88	0.06

Figure 4-8 shows the dependence of the zero-crossing frequency on surface current velocity for the three profiles. This dependence is nearly linear and may be represented by the equation

$$f(\mathrm{Hz})=0.138\ V_C\,(\mathrm{fps})+0.0195 \qquad (4\text{-}20)$$

We ignore the scatter between the calculated frequencies and the above equation.

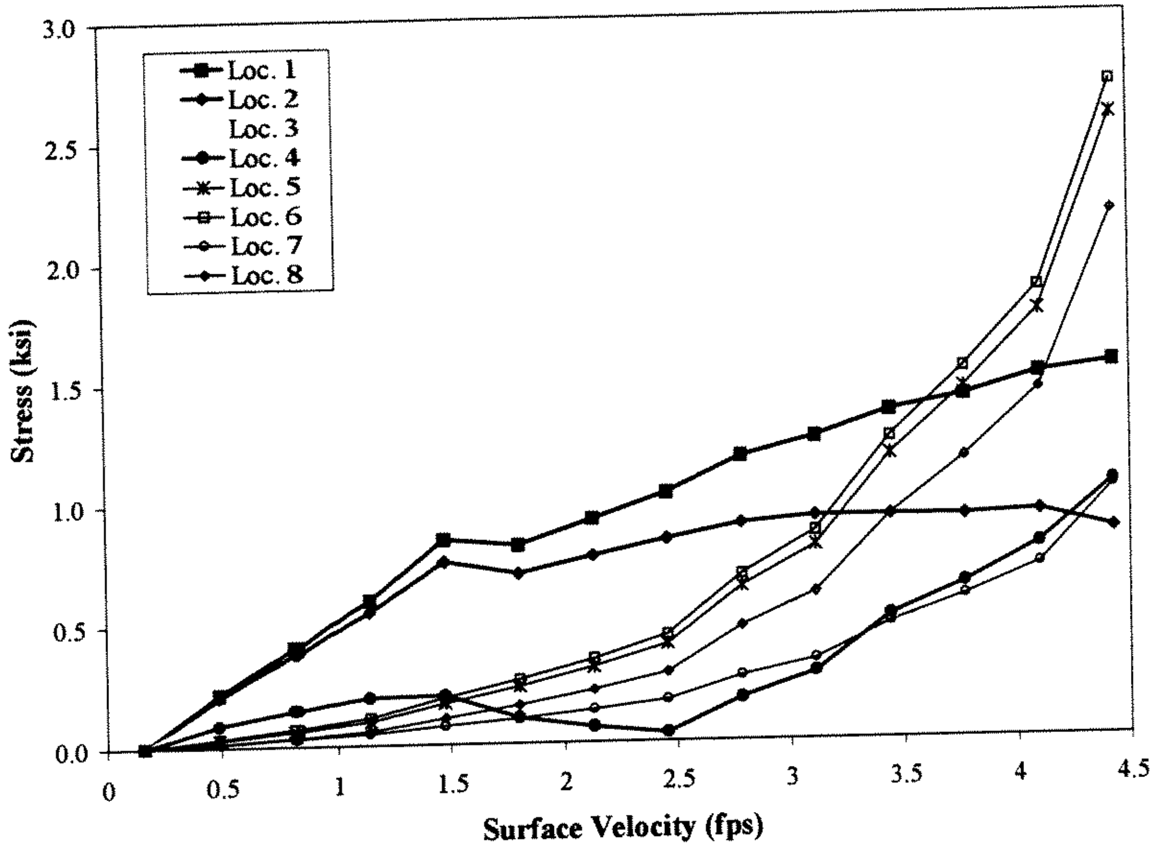

Figure 4-25. Stress vs. surface current velocity at 8 locations in riser. Marlin profile

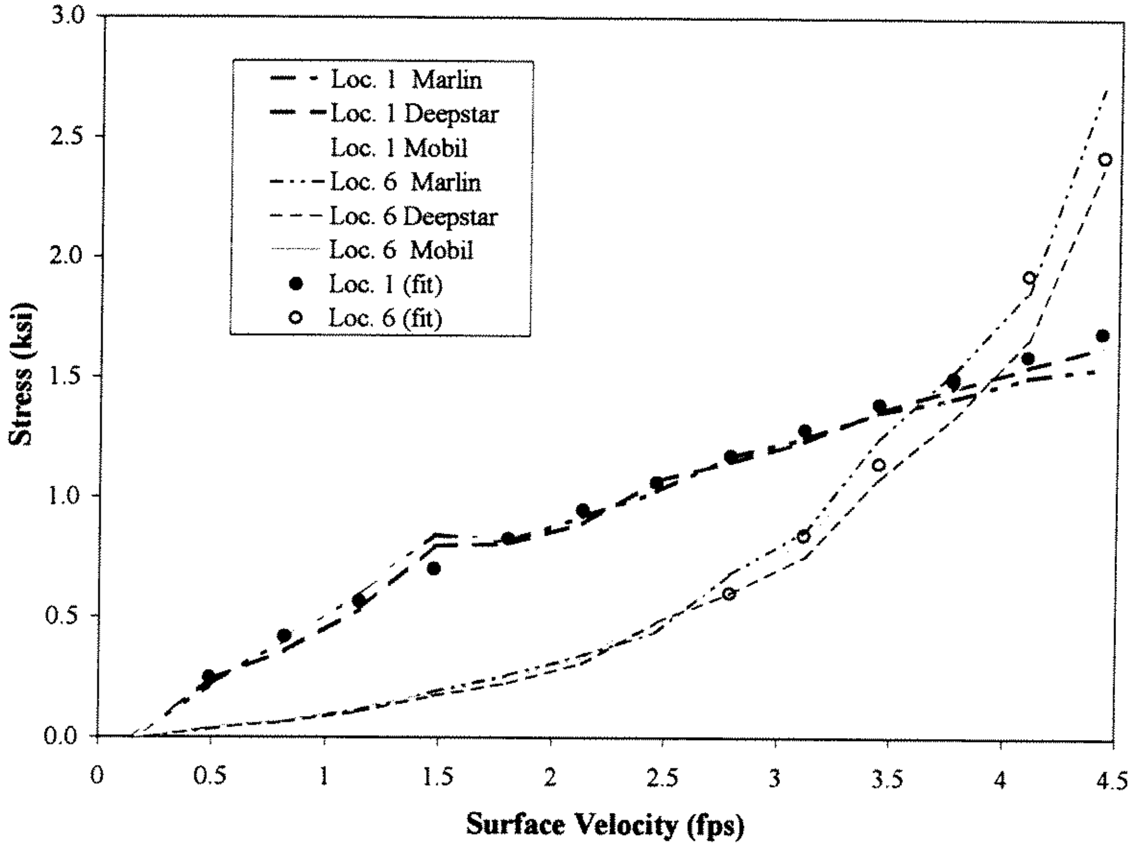

Figure 4-26. Stress vs. surface current velocity at locations 1 and 6 for all current profiles.

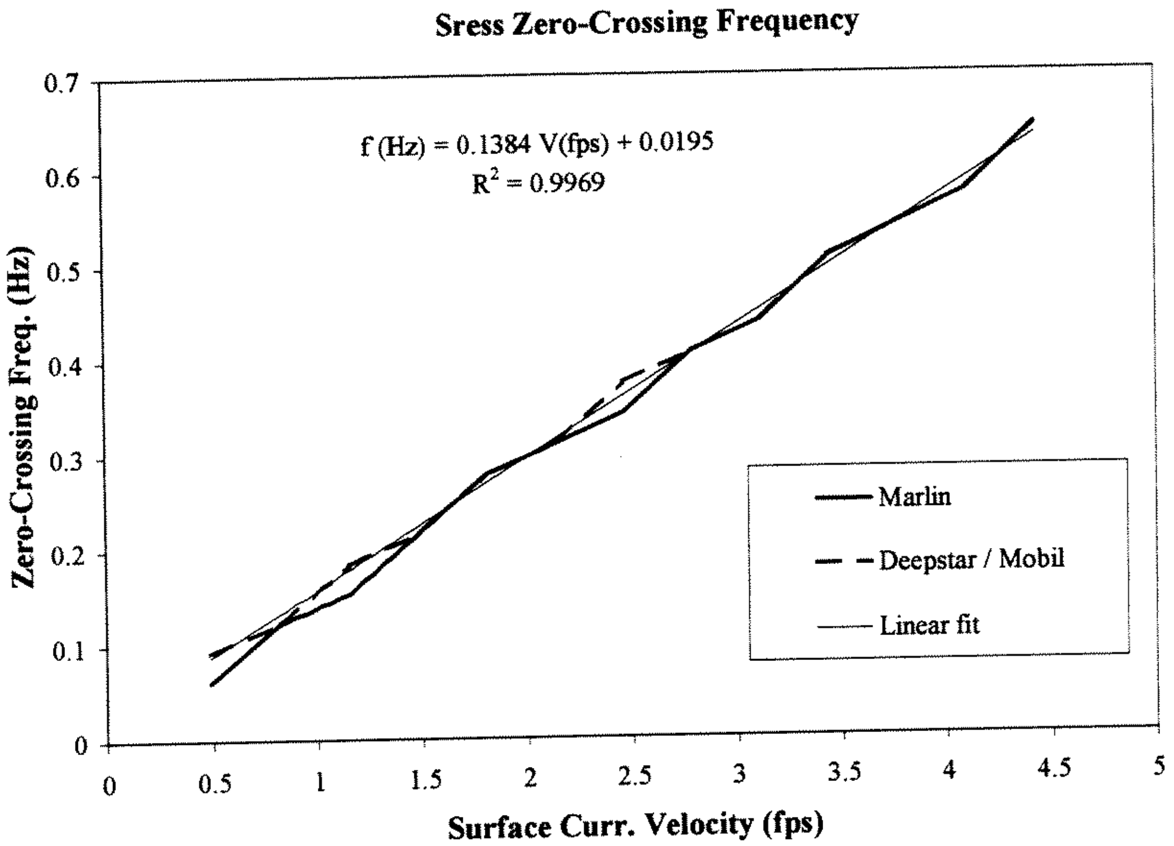

Figure 4-27. Dependence of zero-crossing frequency on surface current velocity.

4.5 FATIGUE RELIABILITY ANALYSIS

The fatigue reliability analysis for VIV uses the same stress amplification factors and S/N models introduced in Section 3.5 for the wave-cycle fatigue analysis. The formulation is also very similar, and begins with the following expression for the total damage:

$$D = \sum_{\substack{i \\ \text{(all current bins)}}} e^{-A} E_{\text{stress amplitude}|i}[S^m] \left(\frac{T}{T_{Z_i}} \right) p_i \tag{4-21}$$

where a and m are the S/N parameters, S is the peak of the vibratory stress, T is the riser design life under consideration (15 years), p_i is the fraction of total time during which surface-current velocity is in bin i, and T_{Z_i} is the zero-crossing period of VIV associated with surface-current bin i. p_i may be expressed as the fraction of the time during which loop currents are active at the site times the fraction of that time during which surface-current velocity is in bin i

There are some differences with the wave-cycle fatigue analysis, in addition to the obvious difference in the characterization of the metocean environment and the dependence of rms stress on the metocean quantities. There is significant uncertainty in the calculated rms stress as a result of the complexity and non-linear character of VIV (more uncertainty than there was in wave-cycle fatigue). Unlike wave-cycle fatigue, there may be significant Type-I and Type-II uncertainty in the fraction of time p_i that will be experienced during the riser's lifetime. Also, the stress peaks may not follow a Rayleigh (or sum of two Rayleighs, as considered in Chapter 3) distribution because VIV is self-exciting phenomenon. This deviation from Rayleign may become important because the stress is raised to the power m (typically near 4) in Equation 4-4.

The bias factor in the calculated VIV stresses has been estimated at 80-90%, and the associated uncertainty has been estimated at 30-40% (Don Allen, personal communication, 1999). These estimates correspond to the Shell-calibrated version of Shear7, which is the version used in this study, and will be used to derive the base-case values.

Another estimate of these quantities was provided by Kim Vandiver (personal communication, 1998), who estimates the bias factor at 50% and a factor of two uncertainty.

Another possible source of information on the uncertainty in VIV is provided by Larsen and Halse (1995), who report discrepancies of up to two orders of magnitude among the predicted VIV amplitudes for a top-tensioned riser by various analysts. It is believed that this wider range of uncertainty is not appropriate for the Shell version of Shear7, which has undergone significant calibration.

The Type-I and Type-II uncertainty in the rates associated with the various bins is decomposed into uncertainty in the fraction of time during which loop currents are active at the site and uncertainty in the histogram rates. The latter is taken as higher for the higher bins in the histogram and is assumed to include both Type-I and Type-II uncertainties. A detailed characterization of these uncertainties would require the complete history of loop-current events and their current velocities, which was not available to this project. The values used here for these uncertainties constitute-first-cut approximations.

A simple way to characterize possible deviations from the Rayleigh distribution of peaks is by thinking of the VIV stress (as a function of time) as a power-law[10] transformation of a narrow-band gaussian process. The resulting distribution of peaks is Weibull. A Weibull exponent of 2 corresponds to a Rayleigh distribution (i.e., the power law has a power of unity). Figure 4-9 illustrates the effect of the Weibull exponent on the appearance of a narrow-band stress time history. Higher Weibull exponents make the peaks sharper. The Weibull exponent will be considered as a source of uncertainty in the analysis.

Table 4-6 lists the uncertainties used in the Type-II calculations, which are based on the foregoing discussion, as well on the material from Section 3.5. Except for the uncertainty in the rates associated with the current bins (which includes both Type-I and Type-II uncertainties) and the uncertainty in Miner's Law, these uncertainties are considered to be Type-II.

Sensitivity analyses will consider alternative assumptions for the uncertainty in VIV stresses and in the uncertainty in the rates associated with surface current bins.

---

[10] Strictly speaking, we define the stress $\sigma(t)$ as $c_0 \, \mathrm{sign}[U(t)] \, |U(t)|^{\alpha/2}$, where $U(t)$ is a gaussian random process and α is the Weibull exponent. Note that the constant c_0 is equal to the rms stress only when the Weibull exponent is 2.

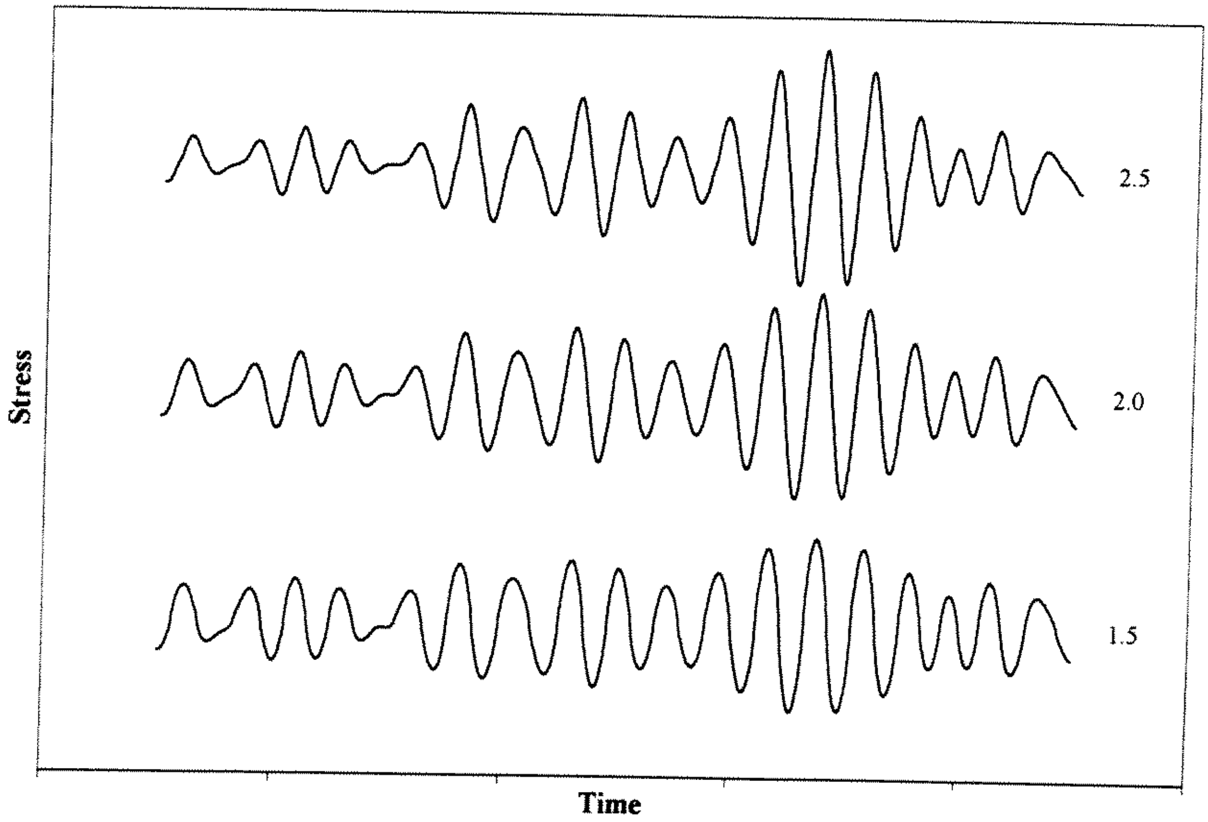

Figure 4-28. Effect of the Weibull exponent on the appearance of narrow-band stress time histories. A Weibull exponent of 2 leads to a Rayleigh distribution of peaks.

Table 4-26 Uncertainties considered in VIV Reliability Calculations

Var. No.	Description	Bias	COV
1	Effect of Profile on Stresses ϵ_{prof}	1	0.06-0.07
2	Uncertainty in fraction of time when loops are active ϵ_{rate}	1	0.3
3	Uncertainty in rates for high bins in histogram ϵ_{tail}	1	1.0[1]
4	Uncertainty in calculated rms stresses	0.85	0.41
		Mean	**σ**
5	Weibull exponent (Rayleigh: 2)	2	0.5
6	S/N ln(Intercept) (a)	var.	var.
7	S/N Slope (m)	var.	0
8	Delta (Miner's Law uncertainty)	0	0.3
9	Stress Amplification Factor	var.	var.

[1] Value for highest bin; values for lower bins are proportional to $\left(\frac{V_i}{V_{\max}}\right)^2$

4.6 RESULTS

We performed VIV reliability calculations for locations 1, 5, and 6 of the riser, considering a design life of 15 years. At location 5, we consider the connector (DNV B fatigue curve). The calculated failure probabilities are shown in Table 4-7. The failure probability is highest at Location 5 (near the water surface), in contrast to the wave-cycle fatigue.

Table 4-27 Calculated Failure Probabilities

Location	Failure Probability
6	1.7E-5
5B	3.1E-4
1	6.1E-5

Tables 4-8 through 4-10 show the design-point coordinates for the three locations. The most important contributor to uncertainty is uncertainty in the rms stress due to VIV, which contributes an uncertainty of two to three orders of magnitude in the failure probability. The next most important uncertainty is uncertainty in the rate of the high current-velocity bins, which contributes only a factor of 2 to 4 to the uncertainty in the failure probability.

Thus, if we consider three general categories of quantities that uncertainty in the calculation of failure probability from VIV-- namely, metocean model, calculation of VIV response and associated stresses, and fatigue-model parameters--we find that the calculation of VIV response an associated stresses is by far the most important of these categories.

Table 4-28 Design point from VIV reliability analysis for Location 1

No.	Description	Value	U	α (direction cosine)		α^2	COV of Pf
1	Effect of Profile on Stresses	1.04	0.549	-0.142	▪	0.020	0.63
2	Uncertainty in fraction of time when loops are active	1.13	0.577	-0.149	▪	0.022	0.67
3	Uncertainty in rates for high bins in histogram	1.82	1.130	-0.291	▬	0.085	1.79
4	Uncertainty in calculated rms stresses caused by VIV	2.69	3.110	-0.802	▬▬▬▬	0.643	227.24
5	Weibull exponent	2.50	1.040	-0.268	▬	0.072	1.54
6	S/N ln(Intercept) (a)	27.30	-0.825	0.213	▪	0.045	1.07
7	S/N Slope (m)	4.00	0.000	0.000		0.000	0.00
8	Delta (Miner's Law uncertainty)	1.13	0.577	-0.149	▪	0.022	0.67
9	Stress Amplification Factor	1.53	1.170	-0.302	▬	0.091	1.91

Table 4-29 Design point from VIV reliability analysis for Location 5

No.	Description	Value	U	α (direction cosine)		α^2	COV of Pf
1	Effect of Profile on Stresses	1.02	0.422	-0.122	▪	0.015	0.48
2	Uncertainty in fraction of time when loops are active	1.11	0.517	-0.149	▪	0.022	0.60
3	Uncertainty in rates for high bins in histogram	2.03	1.270	-0.367	▬	0.135	2.33
4	Uncertainty in calculated rms stresses caused by VIV	2.37	2.790	-0.807	▬▬▬	0.651	88.45
5	Weibull exponent	2.42	0.903	-0.261	▪	0.068	1.25
6	S/N ln(Intercept) (a)	27.30	-0.739	0.214	▪	0.046	0.94
7	S/N Slope (m)	4.00	0.000	0.000		0.000	0.00
8	Delta (Miner's Law uncertainty)	1.11	0.517	-0.149	▪	0.022	0.60
9	Stress Amplification Factor	1.71	0.702	-0.203	▪	0.041	0.87

Table 4-30 Design point from VIV reliability analysis for Location 6

No.	Description	Value	U	α (direction cosine)		α^2	COV of Pf
1	Effect of Profile on	1.03	0.516	-0.123	▮	0.015	0.59
2	Uncertainty in fraction of time when loops are active	1.15	0.632	-0.151	▪	0.023	0.75
3	Uncertainty in rates for high bins in histogram	2.57	1.550	-0.371	▬	0.138	3.64
4	Uncertainty in calculated rms stresses	3.03	3.410	-0.816	▬▬▬	0.666	618.43
5	Weibull exponent	2.59	1.170	-0.280	▬	0.078	1.88
6	S/N ln(Intercept) (a)	27.30	-0.904	0.216	▬	0.047	1.21
7	S/N Slope (m)	4.00	0.000	0.000		0.000	0.00
8	Delta (Miner's Law	1.15	0.632	-0.151	▪	0.023	0.75
9	Stress Amplification	1.12	0.430	-0.103	▮	0.011	0.48

In addition to these results, we consider three sensitivity cases, as follows:

d. Use Vandiver's assessment of uncertainty in the VIV stresses, which correspond to a mean bias factor of 0.5 and a standard deviation of 2 in the calculated stresses.

e. Use a much higher COV (10 instead of 1) for the rate of the highest surface-current bin. This value may not be inappropriate if one considers the possibility of a severe loop-current event with a duration of several days.

f. Double the design life of the riser (to 30 years).

The calculated failure probabilities are shown in Table 4-11. The alternative model for uncertainty in VIV stress yields much higher failure probabilities. The model for increased uncertainty in the rates for the higher velocity bins increases the failure probability by a factor of 3 to 4. A doubling of the design life also increases the failure probability by a factor of 3 to 4.

Table 4-31 Calculated Failure Probabilities

Location	Base Case	a. Alternative Model for Uncertainty in Stresses	b. Increased Uncertainty in Rates for High Bins	c. Doubled Design Life
6	1.7E-5	1.2E-2	8.9E-5	7.6E-5
5B	3.1E-4	1.9E-2	6.4E-4	1.1E-3
1	6.1E-5	1.4E-2	1.2E-4	2.4E-4

4.7 SUMMARY AND DISCUSSION

The results obtained here indicate failure probabilities of the order of 10^{-5} to 10^{-4}. This result is consistent with the experience of few riser failures to VIV in the Gulf. The uncertainty in this failure probability is due mainly to uncertainty in the amplitude of VIV motions and in the resulting rms stresses. The uncertainty in metocean inputs (fraction of time during which loop currents are active at the site, fraction of that time spent in the high-current bins, and current profile) have a moderate effect on the calculated failure probability.

Thus, the most critical issue in evaluating the reliability of risers against fatigue from VIV is the calculation of VIV amplitudes and the associated stresses. Recently analyzed data from VIV associated with tidal currents in Norway may lead to better calibration of VIV models and better quantification of the remaining uncertainty (K. Vandiver, personal communication, 1999).

The model assumed here for uncertainty in the metocean inputs is a crude one, but it may be sufficient given the moderate effect of these uncertainties on the calculated failure probabilities, relative to the uncertainties in the VIV calculations. For instance, a factor of 10 increase in the uncertainty in the rate for the high current bins has a moderate effect on the failure probability.

Another possible limitation in our metocean model is the current profiles. The three profiles considered here are three best-estimate profiles from separate studies and may not have sampled the true Type-II uncertainty in these profiles. Because these three profiles have roughly the same mixed-layer thickness, they produce essentially the same VIV effects.

A third possible limitation in our metocean model is that we did not consider deep-eddy currents.

The highest velocity bin considered in this study (4.4 fps) may not be applicable to other (more exposed) locations in the Gulf, for which values up to 7 fps have been used. This would have an important effect at locations 5 and 6, which are more sensitive to the high current bins.

Appendix B reproduces the notes from a meeting with Professor Kim Vandiver regarding VIV and the development of reliability models for VIV fatigue. These notes contain additional into the methodology for the calculation of VIV, especially for SCRs.

5. Summary and Conclusions

5.1 GENERAL

This methodology and results in this report provide a roadmap for the detailed reliability analysis of top-tensioned TLP risers in a Gulf of Mexico environment, considering extreme loads from hurricanes, wave-cycle fatigue, and VIV (vortex-induced vibration) fatigue. We also identify the most significant Type-II uncertainties in these calculations. This information may be used to make decisions on which elements of the model should be refined further

In the three problems considered, the model used in the reliability calculations consists of the following four basic elements:

1. Metocean Model. A probabilistic of the metocean environment, which describes the intensity and frequency of various seastates of interest. Typically, Type-I uncertainty (e.g.., will my riser experience unusually severe conditions during its service life?) is ignored for fatigue calculations, although we identified fatigue situations where it should not be ignored.

2. Global-Response Model. An algorithm for the calculation of the offset and dynamic response of the vessel, given the values of the metocean quantities. Parametric expressions for the global responses may be derived from simple one-degree-of-freedom models of the vessel, together with results from specialized hydrodynamic studies (e.g., wave drift coefficient, RAO).

3. Riser-Response Model. An algorithm for the calculation of stresses at various locations in the riser, considering the vessel motions, the dynamics of the riser, and direct hydrodynamic forces acting on the riser. The approach followed here was to use the TIARA program to calculate riser stresses for multiple combinations of the metocean parameters and global-response quantities and then fit a parametric expression (often called a response surface) to these numerical results. Any unexplained scatter is carried forward into the reliability calculations. Alternatively, one could have coupled the riser-response software with the reliability analysis software, but this would have required a significant software-development effort.

4. Limit-State Functions. An algorithm to determine the condition of the riser (more precisely, the probability of failure or some other undesirable state), given the riser stresses (and number of cycles, in the case of fatigue). These limit-state functions differ from those used in design in that they must be unbiased and they must also contain information about uncertainty. In the case of extreme loads, we limited ourselves to conventional (force based) definitions of failure, but we recognize the need for the definition of serviceability based limit-state functions. We also recognize that displacement-based limit-state functions may provide a more realistic model for failure of the riser. In the fatigue calculations, the limit-state function takes the form of an SN curve. System effects,

related to the failure of one out of many locations in he riser or to failure of one out of many risers, were not considered in this study.

The reliability calculations consider all possible seastates of interest and calculate their associated vessel motions, riser response, and limit state, thereby calculating the failure probability. Type I and Type-II uncertainties are kept separate in these calculations by using the "Nested FORM/SORM" capability in the RELACS reliability software. Results give us not only the overall (mean) failure probability, but also the individual contributions of the various Type-I and Type-II uncertainties to that probability. This information is essential for the development of an LRFD (Load and Resistance Factor Design) approach for risers.

The intention of this project was to also consider a steel catenary riser (SCR) hanging from a Floating Production Storage and Off-loading (FPSO), and we actually obtained some data for a particular SCR design. In the end, it was decided not to pursue the analysis of the SCR due to difficulty in obtaining some of the associated information and to budget limitations. We do provide some insights as to how the approach used here needs to be modified for the reliability analysis of an SCR.

5.2 EXTREME LOADS

Results from Section 2 indicate that the failure probabilities from extreme loads associated with hurricanes are low for locations at the bottom of the riser and very low for locations at the top. Most of the stress on the riser is generated by the mean offset of the vessel in response to wind, current, and second-order wave forces The most important environmental quantity is wind speed (this is in part a consequence of the way the metocean model was set up, with wind as the primary variable).

The most important Type-II uncertainties are the probability distribution of wind speed (i.e., uncertainty in Vw value associated with a certain exceedence probability), the uncertainty in capacity (limit-state equation), and the uncertainty in the calculation of the mean force on the vessel (which controls vessel offset). Also important are the uncertainty in the stress calculations (for surface locations), Cd at depth (for bottom locations), and Cd in wave zone (for surface locations).

5.3 WAVE-CYCLE FATIGUE

As was the case for extreme loads, results from Section 3 indicate that the failure probabilities from wave-cycle fatigue are low for locations at the bottom of the riser and very low for locations at the top. The latter may have been under-estimated because we did not consider the effect of hurricanes on fatigue (and possibly the associated Type-I uncertainty), which is important at these locations.

As anticipated, most of the damage comes from wave-frequency stresses. These stresses show a strong dependence on Tp, which arise from the vessel RAO and from the dynamics of the riser.

The most important contributors to uncertainty are the uncertainty in the calculated stresses (particularly at the top), uncertainty in the fatigue-law intercept, and uncertainty in the stress amplification factor, and scatter in the fatigue data.

5.4 VIV FATIGUE

The methodology for reliability analysis of VIV-induced fatigue is, like the methodology for the modeling and prediction of VIV, in its early stages of development. The results obtained in Section 4 indicate failure probabilities of the order of 10^{-5} to 10^{-4}, which is consistent with the experience of few riser failures to VIV in the Gulf of Mexico.

The uncertainty in this failure probability is due mainly to uncertainty in the amplitude of VIV motions and in the resulting rms stresses. The uncertainty in metocean inputs (fraction of time during which loop currents are active at the site, fraction of that time spent in the high-current bins, and current profile) have a moderate effect on the calculated failure probability.

The latter conclusion is somewhat tentative because our rather crude model of Type-II uncertainty in the metocean model (we did not have access to the data required for the development of a more sophisticated model), because the three current profiles we considered may not have properly sampled the range of possible profiles, and because we ignored phenomena such as deep-eddy currents.

5.5 ISSUES IDENTIFIED BUT NOT RESOLVED

In addition to the issues identified above and in the preceding sections, there were a number of issues that were identified as important but were not treated explicitly in the analysis. These issues deserve additional consideration in future riser reliability studies.

Behavior of the Tensioners. Our analyses assume that the tensioners will behave as designed, thereby maintaining a nearly constant tension in the risers. It has been observed, however, that the tensioners may become stuck during moderate seastates, resulting in higher stresses which may affect fatigue reliability. There is also uncertainty about the stiffness of the tensioners. This uncertainty affects the stresses near the top of the riser, for both the extreme-load and fatigue reliability analyses.

Foundation Stiffness. Our study ignored uncertainty in the rotational stiffness of the riser foundation. This uncertainty affects the stresses near the bottom of the riser, for both the extreme-load and fatigue reliability analyses.

Serviceability Limit States. Even if the riser does not fail, excessive permanent deformations of the riser may prevent the introduction and extraction of tools, thereby incurring significant costs. Therefore, it may be important to define serviceability limit states and calculate their associated probabilities in order to ensure that these probabilities are sufficiently low.

Other Riser Configurations. It may be necessary to consider riser configurations other than the production configuration. For instance, the reliability of the stress joint at the bottom of the riser may be controlled by a moderate hurricane occurring during work-over (when a heavier riser is used).

Effect of VIV on Cd During Severe Storms. It has been postulated that riser VIV may occur during a severe storm, as a result of storm-generated current or vessel global motions. The principal effect of this vibration would be a very large increase in the riser's Cd.

Wave-Cycle Fatigue from High Seastates. Much of the fatigue damage for locations near the top of the riser comes from high seastates (in the region near the 100-yr Hs). To account properly for this damage, it is necessary to include severe hurricane seastates (with the appropriate fraction of time) in the fatigue calculations. It may also be necessary to consider the Type-I uncertainty associated with these high seastates, as the fraction of time during which these seastates are present during the design life of a particular riser may be substantially greater than the long-term fraction.

Effect of Velocity Profile on VIV. The three profiles considered in the VIV analysis may not represent the range of uncertainty in the thickness of the mixed-layer portion of the velocity profile (i.e., the region of near-constant velocity at the top of the profile). This thickness has a strong effect on VIV stresses. Another related issue is the effect of using average profiles, which are smooth and more efficient at generating VIV, rather than more realistic profiles.

VIV Fatigue from High-Velocity Bins. Because much of the damage comes from the high bins, which are associated with a very small fraction of the total time and occur during rare loop-current events, this fraction may have significant Type-I and Type-II uncertainty. That is, we do not know the long-term fraction during which the current takes a certain high value. Furthermore, even if we knew this long-term fraction, a particular riser may experience this high current during a significantly higher fraction of the time.

5.6 CONSIDERATIONS ABOUT THE RELIABILITY ANALYSIS OF STEEL CATENARY RISERS

The most critical locations in the design of an SCR are the hang-off point and the point where the riser comes in contact with the soil.

The direction of the weather is more important for an SCR than for a top-tensioned riser because it affects the configuration of the riser. In typical SCR design, the stresses are checked for three different weather headings, which result in three different configurations of the riser (namely taut, slack and at 90 degrees). This dependence on direction requires the consideration of directionality in both the metocean model and the riser-stress calculations.

Joint-probability metocean models that include directionality have been developed and used in the past for hurricanes (e.g., Banon et al., 1994). Similar directional information is available for long-term seastates.

To consider the effect of directionality on the riser stresses, one has two options. One may include direction as a variable in the response surface and then perform one set of reliability calculations. Alternatively, one may fit separate response surfaces for weather headings along various sectors, conduct separate reliability calculations for each sector, and then combine the results. Hybrid approaches, where sectors are considered separately but directionality is considered explicitly within each sector, may also be used.

The dynamic response of the riser is expected to be more important for an SCR than for a top-tensioned riser because riser tension is lower. In order to obtain response surfaces that are sufficiently accurate, it may be necessary to explicitly consider the dynamics of the problem (e.g., vessel RAO, fundamental mode and frequency of the riser), or to use a finer sampling on Tp in the experimental design.

The contact between riser and soil is difficult to model and may constitute a significant source of uncertainty.

The VIV analysis of an SCR (particularly the lazy-wave design that was contemplated for this study) poses significant challenges. The meeting transcript documented in Appendix B contains some guidance on how to perform this analysis.

6. References

Banon, H, G.R. Toro, R. Jefferies, and R.S. De. (1994). "Development of Reliability-Based Global Design Equations for TLPs," OMAE Proceedings.

Box, George E.P., and Norman R. Draper (1987). *Empirical Model-building and Response Surfaces*. New York : Wiley, c1987.

British Standards Institute (1993). Code for Practice for Pipelines - Part 3. Pipelines Subsea: Design, Construction and Installation, BS8010: Part 3.

Cooper, C.K. (1988). "Parametric Model of Hurricane-Generated Winds, Waves, and Currents in Deep Water," OTC 5738, Offshore Technology Conference, Houston, Texas, May.

Gran, S. (1992). "A Course in Ocean Engineering". Developments in Marine Technology, Vol. 8. Elsevier Science Publishers.

Jiao, G. (1992). "Stochastic Analysis of Fracture Under Combination of Gaussian Response Processes." Engineering Fracture Mechanics, v. 43, p.321-329.

Jiao, G., and T. Moan (1990). "Probabilistic Analysis of Fatigue due to Gaussian Load Processes." Probabilistic Engineering, Mechanics, v. 5, p.76-83.

Larsen, C.M., and Halse, K.H. (1995). "Comparison of Models for Vortex Induced Vibration of Slender Marine Structures," : Proc.: sixth international conference on flow-induced vibration, Balkema.

Moan, T., S.F. Estefen, S. Saevik, and R.A. Zimmer (1994). "Limit State Functions for the Ultimate Strength of Tubulars Subjected to Pressure, Bending, and Tension Loads." Marine Structures, v. 7, p. 323-344.

Mork, Kim. J., Jorn Spiten, Enrico Torselletti, Odd Bjornar Ness, and Richard Verley (1997). "The Superb Project & DNV'96: Buckling and Collapse Limit State," OMAE-97 Conference, American Society of Mechanical Engineering.

Risk Engineering, Inc. (1996). RELACS Users Manual.

Stahl, B. (2000). *Fatigue Safety Factors for Deepwater Risers: An examination of uncertainties affecting the choice of fatigue safety factors.* Prepared by Bernie Stahl, Ph.D., P.E., Consulting Engineer, for BP Deepwater Underwater Technology Group, Houston, TX

Toro, Gabriel R. (1984). Probabilistic Analysis of Combined Dynamic Responses, Ph.D. Thesis, Department of Civil Engineering. Published as Technical Report No. 65, John A. Blume Earthquake Engineering Center, Department of Civil Engineering, Stanford University.

Toro, Gabriel R., and C. Allin Cornell (1986). "Extremes of Gaussian Processes with Bimodal Spectra," Journal of Engineering Mechanics, ASCE, Vol. 112, No. 5, May 1986, pp. 465-484

Wen, Y-K., and H.C. Chen (1987). "On Fast Integration for Time Variant Structural Reliability." Probabilistic Engineering Mechanics, vol. 2, p.156-162.

Winterstein, Steven R., and Kumar, Satyendra (1994). "Reliability of Floating Structures: Extreme Response and Load Factor Design" OTC 7758.

Wirsching, P.H. (1984). "Fatigue Reliability for Offshore Structures." Journal of Structural Engineering, Vol. 110, No. 10, p. 2340-2356.

Appendix A. Calculation of Stress-Range Uncertainty for Standard Fatigue Model

A.1 INTRODUCTION

It is useful to utilize the fatigue results obtained in Sections 3 and 4 to calculate the equivalent values of the parameters of a simplified model for fatigue reliability analysis. This appendix provides a brief description of the simplified model, describes the process used for the calculation of parameters of the simplified model, and then presents and discusses the results from these calculations.

A.2 SIMPLIFIED FATIGUE MODEL

The reliability model used in this study had its origin in an American Petroleum Institute (API) project for which Professor Paul Wirsching of the University of Arizona served as principal investigator (see Wirsching, 1984). In this model, the time to development of a fatigue crack is given by

$$T=\frac{K\Delta}{B^{m}\Omega} \tag{3-22}$$

in which K and m are the parameters of the S-N curve (see Eq. 3-9), Δ represents scatter in S-N data, and Ω is a deterministic quantity. All random quantities in this equation are assumed lognormal, making it straightforward to perform reliability calculations with this model.

In contrast to the formulations in Sections 3 and 4, where each element of the metocean environment and structural response are treated explicitly (i.e., long-term Hs-Tp scatter diagram, global vessel response, dynamic stresses on riser pipe, stress amplification factor) all uncertainties in the calculation of peak stresses and number of stress cycles are represented by random variable *B*. Similarly, all the deterministic elements in the calculation of stresses are represented by Ω.

We wish to use the results from Sections 3 and 4 to calculate the equivalent coefficient of variation (COV) of B. The corresponding value of Ω may be estimated by performing a deterministic fatigue analysis using best-estimate values for all parameters of the fatigue model in Sections 3 and 4.

A.3 APPROACHES FOR ESTIMATING THE STRESS-RANGE UNCERTAINTY

Two methods are used to deduce the uncertainty corresponding to the stress range random variable. The two methods are not independent of each other because they use results from the FORM/SORM calculations in Sections 3 and 4. Hence, the two methods do not provide independent corroboration of the results. But use of both methods, instead of only one, provides additional confidence that the calculated results are accurate.

Method A

Method A involves matching the probability of failure produced using the simplified fatigue reliability model given by Equation A-1 to the corresponding probability of fatigue failure from Sections 3 and 4.

The random variables K and Δ are common to both reliability models. All other random variables in the detailed fatigue reliability model of Sections 3 and 4 were represented by the stress range random variable B in the simplified model. This method requires the following two inputs:

5. The median fatigue life, which is obtained by plugging in the best-estimate values of all parameters into the detailed models of Sections 3 and 4.

6. The probability of failure, which was obtained in Sections 3 and 4 using the detailed model.

The COV of B was varied until the probability of failure was satisfactorily matched with that of the detailed model.

Method B

This method uses the FORM/SORM direction cosines (alphas) computed in Sections 3 and 4 using the detailed models. In the case of wave-cycle fatigue, the square root of the sum of the squares of the direction cosines of variables 1, 2, 3, 4, 5, 6, and 10 represents the total importance factor from the stress calculations. To compute the associated standard deviation, it is noted that we know the alpha and standard deviation of the ln-intercept A= -ln K and that the alphas are proportional to the COVs in this simple reliability model. Also, we note that $COV[B]=COV[B^{m}]/m$. Thus, the COV due to stress may be written as

$$COV[B]=\sqrt{\sum_{\substack{i \\ \text{(stress-related} \\ \text{quantities)}}} \alpha^{2}{}_{i}}\;\frac{COV[\text{intercept}]}{\alpha_{\text{ln-intercept}}}\;\frac{1}{m} \qquad (3\text{-}23)$$

The direction cosine of B can be obtained in another way by recognizing that the square root of the sum of the squares of the direction cosines must be equal to 1.0. The resulting expression is then

$$COV[B]=\sqrt{1-\alpha^{2}_{\text{ln-intercept}}-\alpha^{2}_{\Delta}}\;\frac{COV[\text{intercept}]}{\alpha_{\text{ln-intercept}}}\;\frac{1}{m} \qquad (3\text{-}24)$$

A.4 RESULTS

The spreadsheet (Table A-1) shows that for wave-induced fatigue, the coefficient of variation (COV) of B varies from 17% to 29%, with most values falling not far from the average of 22%. Methods A and B give nearly the same results for the case of wave-induced fatigue, but it is observed that as the variance becomes higher, the difference between methods A and B increases. This is evident for the case of VIV-induced fatigue. For VIV, the three joints that were analyzed in Ref. 10 gave a COV value of about 50% for method A and 47% for method B. The differences between the methods may be attributable to differences between the detailed and simplified reliability models that show up when the COV is large.

The average value of 22% obtained here for wave-induced fatigue is comparable to values in current use for both fixed and floating structures (e.g., Lotsberg et al., 1984; Wirsching et al., 1995; Nikolaidis et al., 1991).

A.5 ACKNOWLEDGMENTS

This appendix is largely based on material prepared by Bernie Stahl for BP , with some assistance from G. Toro (Stahl, 2000). We thank B. Stahl and H. Banon for their permission to publish these results.

Table A-1. Calculation of Stress-Range Uncertainty from FORM/SORM Results

Joint	Data Source	Pf, Life = 15 yrs	beta, Life = 15 yrs	median life (yr)	**COV B Meth A**	$\sigma_{\text{ln-intercept}}$	$\alpha_{\text{ln-intercept}}$	α_{Δ}	**COV B Meth B**
Vessel-induced Fatigue									
Loc 3	Tab 3-15	6.40E-04	3.22	286	0.192	0.42	0.459	0.321	0.190
Loc 5 X	Tab 3-18	6.20E-10	6.08	85,439	0.231	0.97	0.682	0.207	0.228
Loc 5 B	Tab 3-17	3.20E-11	6.53	13,773	0.230	0.42	0.402	0.281	0.228
Loc 10 X'	Tab 3-16	2.30E-07	5.04	24,719	0.290	0.97	0.66	0.2	0.285
Loc 1 B	Tab 3-14	1.30E-08	5.57	3,834	0.215	0.42	0.422	0.295	0.213
Loc 2	no table	3.40E-12	6.86	4,772	0.168	0.42	0.5	0.349	0.166
Loc 6 B	Tab 3-19	3.50E-14	7.49	24,163	0.213	0.42	0.426	0.298	0.211
Loc 8 B	Tab 3-20	4.20E-19	8.86	93,271	0.213	0.42	0.426	0.298	0.211
					0.219				**0.216**
VIV-induced Fatigue									
Loc 5 B	Tab 4-9	3.10E-04	3.42	12,398	0.502	0.42	0.214	0.149	0.474
Loc 1	Tab 4-8	6.10E-05	3.84	29,239	0.504	0.42	0.213	0.149	0.476
Loc 6	Tab 4-10	1.70E-05	4.14	47,409	0.496	0.42	0.216	0.151	0.469
					0.501				**0.473**

Appendix B. Summary of Meeting to Define Approach for VIV Analysis of Vertical and SCR Risers

MIT, March 27, 1998

Attendees:

Pierre Beynet, Amoco

Hiren Maniar, Chevron

Chuck Miller, Stress Engineering

Gabriel Toro, Risk Engineering

Kim Vandiver, MIT Dept. of Ocean Engineering

Introduction

The purpose of the meeting was to identify the main sources of uncertainty in the calculation of vortex-induced vibration (VIV) for the two riser designs considered in this study and to develop an approach for incorporating of these effects within the reliability calculations. It was emphasized that this exercise is different from design, in the sense that we want to remove intentional biases in the inputs and models used. Instead of using conservative values for a parameter, we want to use a best estimate of the parameter and a measure of the associated uncertainty.

This summary follows the chronological sequence of the discussions, rather than organizing the various topics into a logical sequence. In particular, we start with discussion of key issues for the SCR riser, move to key issues for the vertical riser, discuss the approach for the analysis of the vertical riser, and return to the approach for the analysis of the SCR riser.

Issues and Sources of Uncertainty for SCR Riser

For this discussion, we used the information on the riser dimensions and configuration that was provided by and Chuck Petrauskas (1/14/98).

7. **Current Profile** Given the current profile, the effective current acting on the plane of the riser is decomposed into a component normal to the riser (important for VIV) and a longitudinal component (not considered). This decomposition is performed using the static configuration of the riser. With typical current profiles, this decomposition has the effect of further reducing the in-plane currents at depth. In spite of this, the critical fatigue stresses may occur at depth because the tension is lower there.

   There is also another component of current perpendicular to the plane of the riser. This component is not affected by the geometry of the riser.

   An issue that came up several times is that the current practice of specifying a smooth profile for VIV may be quite conservative because a smooth profile is more efficient at generating VIV than a realistic profile. In particular, the constant-velocity portion at the top of the profile is probably unrealistic. The thickness of this constant portion is believed to have a significant effect on VIV and should be investigated.

8. **Dynamics of Riser**. Two complicating factors are the large number of modes of vibration and the complicated boundary conditions at the bottom.

9. **Deep-Eddy Currents**. Current (in the direction perpendicular to the plane of the riser) at the depth of the buoyancy segment of the riser will have a large effect on VIV, due to the larger diameter of this segment. Typical profiles used in design include very low current velocity at those depths, but some measurements have indicated the existence of deep currents. This deep current may or may not be an issue for the GOM locations of interest in this study.

Current profile with high velocity at depth

10. **Effect of Buoyancy Segment on the Dynamics of the Riser**. This is due to the differences in mass/length and stiffness of this segment relative to the riser pipe. If the buoyancy segment does not act as a good reflector, energy will be dissipated at the seafloor contact, thereby helping reduce the amplitude of VIV motions. If it acts as a good reflector, the vibrations on either side of the buoyancy segment will be isolated from each other, and the benefit of energy dissipation at the bottom will be lost.

Shear7 allows the specification of arbitrary tension distributions along the riser length. This is required for this problem.

Issues and Sources of Uncertainty for Vertical Riser

The VIV behavior of vertical top-tensioned risers is better understood than that of flexible risers. Nearly all the sources of uncertainty identified here also apply to the SCR riser discussed earlier.

1. **Model Uncertainty and Bias of Shear7** Kim Vandiver estimates an uncertainty of approximately a factor of 2 and a bias of 50 to 100% for a vertical riser (this bias applies if one uses the largest of the single-mode and multi-mode response).

2. **Stress-Concentration Factors.** The uncertainties here are the same as in the fatigue analysis of risers due to wave motions.

3. **S/N Curves.** Chuck Miller mentioned that they used the DNV b curve and the API X' curve for the Marlin design work. We need to use the unbiased versions of these.

4. **Shear7 Parameters**

   a. **Mode Cutoff.** This parameter should be set on a case-by-case basis, depending on whether one or several modes dominate the response. The suggested approach is to start with very little cutoff and see how many modes contribute to the response. It was recommended to use the highest of the single-mode and multi-mode response.

b. **Multi-Mode Reduction Factor**. This parameter behaves differently in the new version of Shear7. Now, it is a factor that multiplies the lift coefficients. In the past, this factor was applied to the final result. The lift coefficients used by Shear7 are conservative (by approximately a factor of 2). The source of this conservatism is that, for each value of the reduced velocity, the program uses the highest lift coefficient (over all possible values of the normalized amplitude a/D).

1. **Current Velocity Profile.** The thickness of the constant-velocity portion at the top of the velocity profile has an important effect on VIV response. It would be desirable to work with the average profile for loop-current events in a given intensity range. An additional improvement would be to work with actual profiles (snapshots) rather than working with average profiles, which are smoother than actual profiles.

Approach for the VIV Analysis of Vertical Riser

1. **Multiple- vs. Single-Mode Response.** Run as multi-mode first to determine with one or more modes dominate the response. Use the highest of single-mode and multi-mode response.

2. **Thickness of Constant Velocity Portion of Profile.** Investigate the effect of varying this thickness by ~ 20%. If it has an important effect, as anticipated, we should obtain realistic values (or probability distributions) of this thickness for use in this study.

3. **Multi-Mode Reduction Factor.** Vary this factor to investigate its effect on the response. If it is important, treat explicitly in the reliability calculations.

Note on the treatment of non-monotonic current profiles. Shear7 requires the specification of a monotonic profile (or a monotonic profile surrounded by portions with zero velocity). One can approximate the response to a non-monotonic profile by re-arranging it into an equivalent monotonic profile, which is constructed as the monotonic profile that has the same depth-wise probability distribution of velocity. This is done by breaking-up the current-velocity profile into chunks with approximately the same velocity and then re-arranging them from lowest velocity (at the bottom) to highest velocity (at the top).

Approach for the VIV Analysis of SCR Riser

1. **Dynamics**. To be able to build a Shear7 model of the SCR riser, it is important to understand the dynamics of the riser, particularly the effect of the buoyant segment. To this effect, the following calculations were suggested:

    a. Apply a distributed horizontal force (on the plane of the riser). The force should have a sinusoidal variation with time. Observe the response of the riser, with emphasis on how much of the motion gets to the buoyant section and how much motion there is beyond the buoyant section. This should be done for several values of the frequency.

    b. Similarly, apply a vertical force on the buoyant section of the riser.

    It is important to use an appropriate model for hydrodynamic damping in these calculations

1. **Presence of Bottom Currents.** We need to determine if the GOM locations under consideration for this riser design have deep-current events. If so, VIV effects on the buoyant section will probably be important.

2. **Boundary Conditions at Bottom.** The boundary conditions at the bottom of the SCR riser (elastic foundation effects, etc.) are likely to result in less severe stresses than the simpler pinned or rigid boundary conditions. Using analyses like those in 1a with the various boundary conditions, one can determine the ratio of peak stresses under the realistic and the simpler boundary conditions.

    This ratio can then be used to correct the bottom stresses obtained with Shear7.

The tasks identified for the SCR riser are exploratory. Results from these calculations will be used to construct the Shear7 model for this riser.